Multi-functional metamaterials

Thesis by
Sai Sharan Injeti

In Partial Fulfillment of the Requirements for the
Degree of
Doctor of Philosophy

CALIFORNIA INSTITUTE OF TECHNOLOGY
Pasadena, California

2021
Defended April 15, 2021

Sai Sharan Injeti
ORCID: 0000-0003-1941-9752

ACKNOWLEDGEMENTS

First, I would like to thank Prof. Kaushik Bhattacharya and Prof. Chiara Daraio for being incredible advisors and mentors. As advisors, they have given me immense intellectual freedom in research, while providing necessary guidance. Kaushik's theoretical expertise together with Chiara's experimental aptitude made for an excellent combination in solving research problems that are both fundamental and have an immediate impact through application. They have also been great mentors to me by instilling in me a thought process that is centered around making a huge positive impact on society. I am very grateful to them for shaping me into a better researcher and person.

I would also like to thank Prof. Guruswami Ravichandran and Prof. José Andrade for serving on my thesis committee. Caltech has no shortage of role models, but Prof. Guruswami Ravichandran has been someone I looked up to since my first interaction with him. I would like to thank him for all the feedback on my research and general advice, while being an incredibly humble person. I am also very grateful to the support from the Shang-Li and Betty Huang endowed graduate fellowship fund in mechanical engineering.

All members of both the Bhattacharya and Daraio groups have been very helpful during my journey at Caltech. In particular, I would like to thank Connor McMahan, Andrew Akerson, Paolo Celli, Hao Zhou, Eric Ocegueada, Gunho Kim, and Alex Ogren for valuable discussions, guidance, and input on my research. I would also like to thank Petros Arakelian for help with 3-D printing throughout my research. I am grateful to Jenni Campbell and Carolina Oceguera for being extremely prompt with scheduling and purchases at various stages of my research. I would like to extend a special thanks to my friend and tennis partner Tony Zhang for keeping our weekly tennis sessions going throughout my time here.

I am very grateful to my undergraduate advisors and mentors Prof. M. S. Sivakumar and Prof. R. K. Annabattula for introducing me to research in mechanics and for instilling in me the right work ethic and discipline. Finally, I am most grateful to my family – my parents and my brother, for being my main pillars of strength, constantly believing in me, and unconditionally supporting my path.

ABSTRACT

Optimally designing interdependent mechanical properties in a structure allows for it to be used in application where an arbitrary combination of properties is desired. Architected materials have proven to be an effective way of attaining mechanical behaviors that are unattainable using their constituent materials alone, such as unusual static mechanical properties, unusual wave propagation behavior, and shape morphing. The advent of 3-D printing has allowed for fabricating metamaterials with complex topologies that display engineered mechanics. However, much of the current efforts have focused on optimally designing simple mechanical behaviors such as designing for stiffness and weight, particular frequency bandgaps, or bi-stability. In this work, we study two metamaterial systems where we control and optimize a wide set of static and dynamic properties, and one complex multi-stable structure.

Most studies on the optimal design of static properties have focused on engineering stiffness and weight, and much remains unknown about ways to decouple the critical load to failure from stiffness and weight. This is the focus of the first part of our work. We show that the addition of local internal pre-stress in selected regions of architected materials enables the design of materials where the critical load to failure can be optimized independently from the density and/or quasistatic stiffness. We propose a method to optimize the specific load to failure and specific stiffness using sensitivity analysis, and derive the maximum bounds on the attainable properties. We demonstrate the method in a 2-D triangular lattice and a 3-D octahedral truss, showing excellent agreement between experimental and theoretical results. The method can be used to design materials with predetermined fracture load, failure location and fracture paths.

For the second part of our work, we focus on designing acoustically transparent structures, by engineering the acoustic impedance – a combination of wave speed and density, to match that of the surroundings. Owing to the strong correlation between acoustic wave speed and static stiffness, it is challenging to design acoustically transparent materials in a fluid, while maintaining their high structural rigidity. We provide a sensitivity analysis to optimize these properties with respect to design parameters of the structure, that include localized masses at specific positions. We demonstrate the method on five different periodic, three dimensional lattices, to calculate bounds on the longitudinal wave speed as a function of their density and stiffness. We then perform experiments on 3-D printed structures, to validate our numerical simulations. Further, using the sensitivity analysis together with a data-driven approach, we design and demonstrate a mode demultiplexer, that is capable of splitting arbitrarily mixed modes. The tools developed in this work allow for designing structures in a plethora of applications, including ultrasound imaging, wave filtering, and waveguiding.

Finally, most multi-stable structures are limited by bi-stability either at the macroscopic or the unit cell level owing to the difficulty in engineering a highly non-linear energy landscape using just elements that display convex energy landscapes. We demonstrate a method to design arbitrarily complex multi-stable shape morphing structures, by introducing rigid kinematic constraints together with disengaging energy storing elements. We present the idea on a kagome lattice configuration, producing a quadri-stable unit cell and complex stable topologies with larger tessellations, validated by demonstrations on 3-D printed structures. Most designs that use passive actuation address one-way shape morphing along the direction of least resistance. We demonstrate reversible, thermally actuated shape morphing between stable open and closed topologies using shape memory springs. The designs can be extended to non-planar structures and fabricated at vastly different length scales.

PUBLISHED CONTENT AND CONTRIBUTIONS

[1] Injeti, S. S., Bhattacharya, K. & Daraio, C. (2021). Data-intensive architecture of a mode demultiplexer. *In Preparation*.

[2] Injeti, S. S., Celli, P., Bhattacharya, K. & Daraio, C. (2021). Tuning acoustic impedance in load-bearing structures. *In Preparation*.

[3] Injeti, S. S., Daraio, C. & Bhattacharya, K. (2021). Multi-stable shape morphing. *In Preparation*.

[4] Injeti, S. S., Daraio, C. & Bhattacharya, K. (2019). Metamaterials with engineered failure load and stiffness. *Proceedings of the National Academy of Sciences*, *116*(48), 23960–23965. https://doi.org/10.1073/pnas.1911535116

Sai Sharan Injeti contributed to designing and performing the research (theory, numerics, and experiments), analysing the data, and writing the papers.

CONTENTS

LIST OF FIGURES

LIST OF TABLES

Chapter 1

INTRODUCTION

1.1 Motivation

It has long been understood that material microstructure or microgeometry affects a material's overall or engineering property, and this has been exploited in composite materials, sandwich structures, and cellular materials [47, 85, 122]. There are well-established engineering approaches [93] and rigorous mathematical results [85, 86] that have studied the problem of finding bounds on mechanical properties and identifying optimal microstructures that attain them. However, till recently, the ability to make materials with controlled microgeometry was limited. The advent of 3D printing and similar approaches of materials synthesis with highly controlled geometries have overcome this limitation [45], and opened the doors for engineering architected or metamaterials with unusual mechanical properties [10, 64].

Engineering failure load and stiffness

A topic that has received particular attention is designing and synthesizing materials that maximize stiffness for a given density [9, 28, 30, 32, 41, 46, 65, 104, 108, 116, 118, 127]. A recent result demonstrated that it is possible to approach the Hashin-Shtrikhman bounds with a single-scale architected material [10], though hierarchical structures were known earlier [43]. Another topic that has received much attention is the development of architected materials with unusual (negative) Poisson's ratio [40, 105]. Note that both these concern aspects of the overall linear elastic modulus. There is now an emerging line of work on nonlinear properties. For example, Milton and his collaborators have studied the class of materials that can undergo prescribed finite deformation including the identification of a pentamode material [18, 87].

Still, much remains unknown about failure for many reasons. Failure depends on the local state of stress, and it is therefore difficult to characterize from a theoretical point of view. Further, failure is sensitive to defects and imperfections. Finally, there are no known bounds on failure. However, failure is critically important from the point of view of application. Typically, the critical load to failure increases with stiffness, and this leaves a gaping hole in the space of possible material properties as shown in Fig. 1.1(A). This figure shows the specific stiffness and specific failure load of various materials systems, and we note that there are no materials that have high specific load to failure but limited stiffness indicated by the dashed ellipse in Fig. 1.1(A).

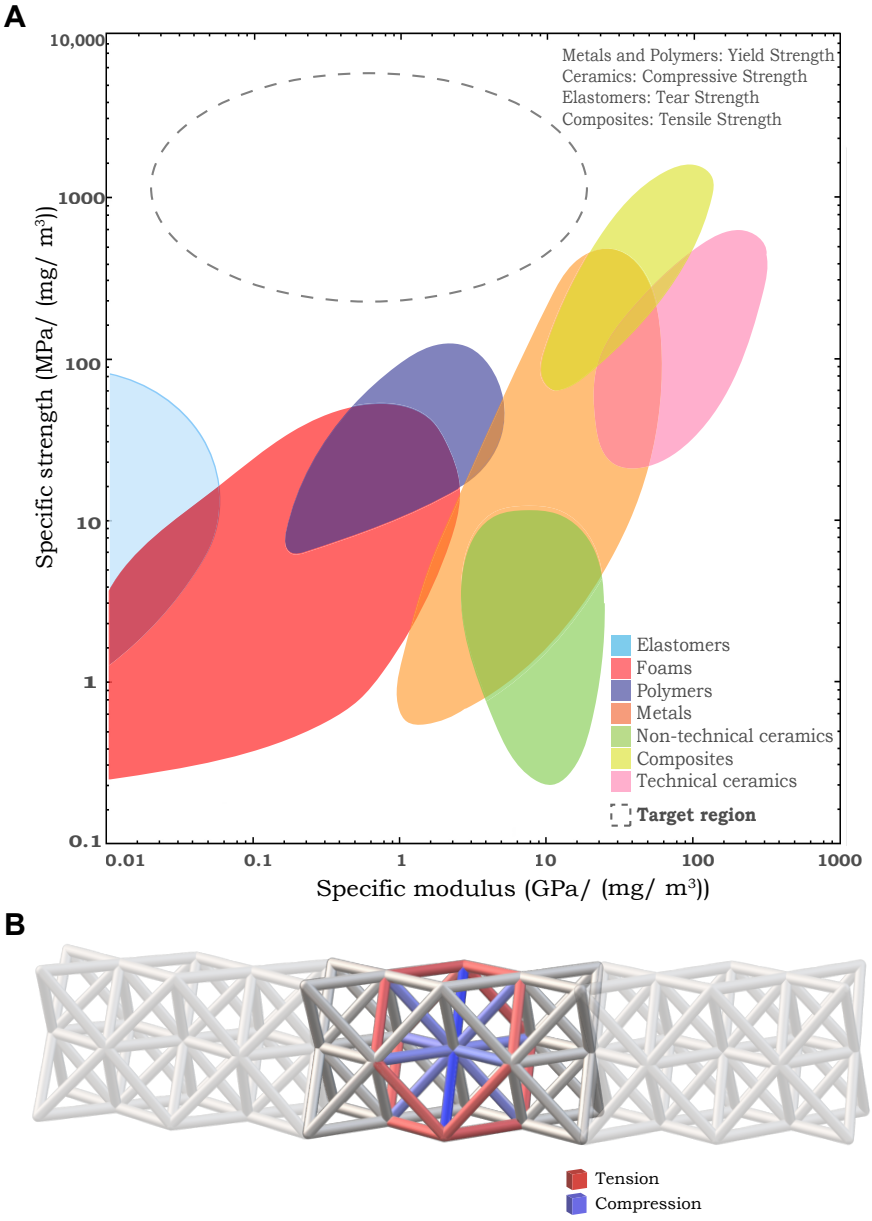

Figure 1.1: Specific strength vs modulus: ***(a)*** *Material selection chart of specific modulus (ratio of Young's modulus of elasticity E to density ρ) versus specific strength (ratio of stress at failure σ_f to ρ) for different materials/ structures according to data obtained from thirtyone.* ***(b)*** *Example of an internally stressed octet truss with two unit cells (darker gray members and colored bars). Red and blue elements illustrate the distribution of a state of self stress.*

Engineering wave speed and stiffness

In acoustics, the transmission coefficient can be defined as the ratio of amplitude of the transmitted wave to that of the incident wave at an interface between two media [49]. This ratio is unity when the acoustic impedances (product of density and wave speed) of the two media are identical [49], ensuring maximum transmission of elastic wave energy across the interface. This is of particular importance in the design of acoustically transparent materials, where the acoustic impedance of the material matches that of the surroundings, and produces negligible interference with the propagating acoustic waves. Traditionally, while engineering the acoustic impedance of a structure, there is not much freedom in designing its static stiffness. This is because the static stiffness (along the direction of wave propagation) varies with the square of the elastic wave speed, making it difficult to design structures with high stiffness but low or moderate wave speeds. There are several applications where the mechanical rigidity of these acoustically transparent media is critical, including underwater sonar windows, acoustic imaging using transducer arrays, medical ultrasonography, hydrophone casings, and other support structures for polymer transducers [2, 26, 90, 107, 117].

Engineering the wave speeds in different regions of a structure allows us to guide waves based on their modal composition and frequency. Such manipulation of waves enables a demultiplexer, where multiple/mixed modes of waves can be separated into their individual components that are guided in distinct paths. Such a device can be extremely valuable in realizing phononic [17, 33, 75, 76, 77, 94, 128] and photonic [22, 63, 66, 71, 72, 123, 124] based computing. Phononic and photonic based computing have received increasing attention in recent years due to their potential in information transfer with minimal losses in heat, as opposed to current carrying wired electrical systems. In order to facilitate thermal or mechanical computing, it is important to realize phononic and photonic devices that are analogous to electronic systems. Some of these devices include thermal and acoustic rectifiers [22, 66, 71, 75, 77, 94], switches [5, 13, 15, 73], diodes [15, 36, 75, 102], and lasers [62, 119]. All such devices are to be used together in order to realize a phononic or photonic computer, but each device may use as an input, waves propagating along different modes and at different frequencies. It would be more beneficial to send multiple/ mixed modes of waves through a single channel and be able to separate the individual components to the devices, as opposed to transmitting each mode through a different line.

Engineering multi-stability

A number of applications including robotics [24, 129], bio-medicine [70, 130], energy storage [50, 109], deployable aerospace and solar structures [23, 25] require reconfigurability between a number of shapes. These shape changes can include morphing between flat and curved geometries [51, 67] or between open and closed topologies [23, 92]. Further, it is important that the structure is stable in each configuration for it to be load-bearing in application. Engineering arbitrarily complex

stable configurations requires the design of a highly non-linear energy landscape. However, in most studies the overall structure or the repeating elements are bi-stable limiting the number and complexity of stable configurations. This can be attributed to the difficulty in engineering highly non-linear energy landscapes in simple mechanisms that use energy storing elements that display strictly convex energy landscapes.

1.2 Scope of the thesis

In this work, we demonstrate ways to decouple mechanical properties of materials that are strongly correlated by tuning certain elements in its topology. First, we demonstrate a way to decouple the critical load to failure of a structure from its stiffness and weight, when the structure may be subject to multiple modes of loading. We formulate the expressions for failure load and stiffness of truss-like structures in terms of its topology, that include the dimensions of struts and internal stress distribution. We perform a sensitivity analysis that uses an adjoint method to calculate bounds and independently design the failure load, stiffness, and density of a truss. In our analysis, we vary the cross-sectional areas of bars and pre-stress in the structure. We validate our results with experiments on 3-D printed trusses, where a desired internal stress distribution is simulated by introducing pre-compression in selected bars of the truss.

Second, we study periodic trusses, i.e. lattices, that feature point masses at selected joints to manipulate waves propagating through a structure independently from its static properties. Specifically, we engineer the wave speeds of chosen modes at a frequency while also designing for the static stiffness. We obtain bounds on the mechanical properties using a sensitivity analysis, where we vary the cross-sectional areas of struts and the point masses at the joints. We validate our results with experiments on 3-D printed structures, where we analyze one lattice with a fast propagating longitudinal wave and another with a slow propagating wave at the same frequency and similar densities. Our sensitivity analysis allows us to also calculate the second derivative of frequency of wave propagation with respect to the wavenumber (magnitude of wave vector). This allows us to automate the tracking of modes in a dispersion plot for a structure. We then use a data-intensive approach that involves tracking dispersion curves for several thousand lattices, which allows us to design a demultiplexer that can split a mixed mode input. We demonstrate the method by demultiplexing a combination of longitudinal and shear waves into individual channels. We validate our results on 3-D printed lattices where we recover the demultiplexed signal at the output, reconstruct the expected dispersion curves, and measure the wave speeds.

Third, we demonstrate shape morphing between arbitrarily complex stable topologies using rigid kinematic elements and disengaging springs. We design a tri-stable switch that has two stable closed configurations and one stable open configuration. As the switch consists of two equilateral

triangles, it can be tessellated in a kagome lattice configuration to realize several mode stable shapes. We show that a unit cell of the kagome lattice is quadri-stable and larger tessellations can attain thousands of stable configurations. We demonstrate multi-stability on 3-D printed tessellations where the rigid triangles and energy storing springs are printed with materials that possess different stiffnesses. We demonstrate reversible shape morphing between open and closed stable shapes using thermally actuated shape memory springs. We also measure the force in each spring to cause each structure to snap.

Finally, we summarize the key findings of our research and discuss potential avenues for future work.

Chapter 2

ENGINEERING FAILURE LOAD AND STIFFNESS

Research presented in this chapter has been adapted from the following publication:

Injeti, S. S., Daraio, C. & Bhattacharya, K. Metamaterials with engineered failure load and stiffness. *Proceedings of the National Academy of Sciences* **116**, 23960–23965 (2019).
https://doi.org/10.1073/pnas.1911535116

2.1 Motivation

Architected materials have proven to be a very effective way of making materials with unusual mechanical properties. For example, by designing the mesoscale geometry of lattice materials, it is possible to obtain extremely high stiffness to weight ratio or unusual Poisson's ratio. However, much of this work has focused on properties like stiffness and density, and much remains unknown about the critical load to failure. This is the focus of the current work. We show that the addition of local internal pre-stress in selected regions of architected materials enables the design of materials where the critical load to failure can be optimized independently from the density and/or quasistatic stiffness. We propose a method to optimize the specific load to failure and specific stiffness using sensitivity analysis, and derive the maximum bounds on the attainable properties. We demonstrate the method in a 2-D triangular lattice and a 3-D octahedral truss, showing excellent agreement between experimental and theoretical results. The method can be used to design materials with predetermined fracture load, failure location, and fracture paths.

2.2 Introduction

In this work, we show using trusses that the gap indicated by the dashed ellipse in Fig. 1.1(A) can be bridged. In particular, we show that the critical load to failure in a truss can be varied within a range while holding the stiffness and density fixed. We do so by exploiting states of self-stress in a truss. A truss is a structure made of elongated members or bars joined together at nodes that can transmit force but not moments. Depending on the topology of a truss, it may have mechanisms whereby some nodes are free to move or it can support states of self stress. Fig. 1.1(B) shows an octet truss with self stress – the bars in blue are in compression while the bars in red are in tension. We show that states of self-stress can be exploited to increase the critical load to failure, and then derive bounds on the range of specific (per unit relative density) stiffness and specific load to failure, where the relative density of a truss is the ratio of density of the lattice to the density of the material from which it is constructed. We validate the results from numerical simulations

using experiments in both two and three dimensions.

Our work is related to two ideas in the literature. First, Paulouse *et al.* five showed using the 3D version of a Kagome lattice that they can control the nonlinear mechanical response by selectively activating buckling modes using states of self-stress. Our focus is on tensile fracture rather than compressive buckling. Second, Mishuris and Slepyan [88] showed that the peak stress in a self-equilibrated 1-D chain of stretched and compressed bonds can be controlled by varying the internal stresses. Our idea is similar, but addresses higher dimensions.

2.3 Optimization of specific failure load and specific stiffness

A pin-jointed truss is a structure made of linear bars that carry uniaxial (tensile or compressive) force held together by joints that transmit force but no moment. The truss is called *statically determinate* if the force in each bar can be calculated only from static equilibrium equations given the external loads. If there are too many bars such that the equilibrium conditions are insufficient to determine the forces in the members, the truss is *statically indeterminate*. Such a structure can be internally stressed, even when there are no external loads. An analysis going back to Maxwell and subsequently generalized two,three shows that

$$b - nd + 3(d-1) = s - m, \tag{2.1}$$

where b is the number of bars, n the number of joints, d the dimension (two or three), s the number of linearly independent (modes) of self-stress, and m the number of independent mechanisms. In a self-stressed system, some members are in tension while others are in compression, but the whole structure is in equilibrium without any external loads. In our analysis, we consider a statically indeterminate truss with s states of self-stress and denoted by s_α^j be the stress in the α^{th} bar due to the j^{th} state of self-stress, $\alpha = 1, \ldots, b,\ j = 1, \ldots, s$. So the stress in the α^{th} bar is $\sum_j \lambda_j s_\alpha^j$ where λ_j is the intensity of the j^{th} state of self-stress.

In designing architected materials, the octet truss has played a predominant role among space filling structures, since it naturally exhibits high stiffness and strength that scale linearly with its relative density. Also, the structure has a nodal connectivity of 12, making it highly indeterminate with a stretch dominated mechanical response twenty. These properties make it a prime example for our analysis. We study the octahedral truss with six unit cells and nine states of self-stress (Fig. 2.1(A)) and the octet truss with two unit cells and five states of self-stress (Figures 1.1(B), 2.1(B), and 2.1(C)). The octahedral truss considered is still a portion of a larger octet truss with several unit cells stacked together in all three dimensions.

Now suppose the truss is subjected to a particular mode of loading (e.g., Fig. 2.1(A)) with an applied force T. We solve the equations of equilibrium as described in the Methods section and

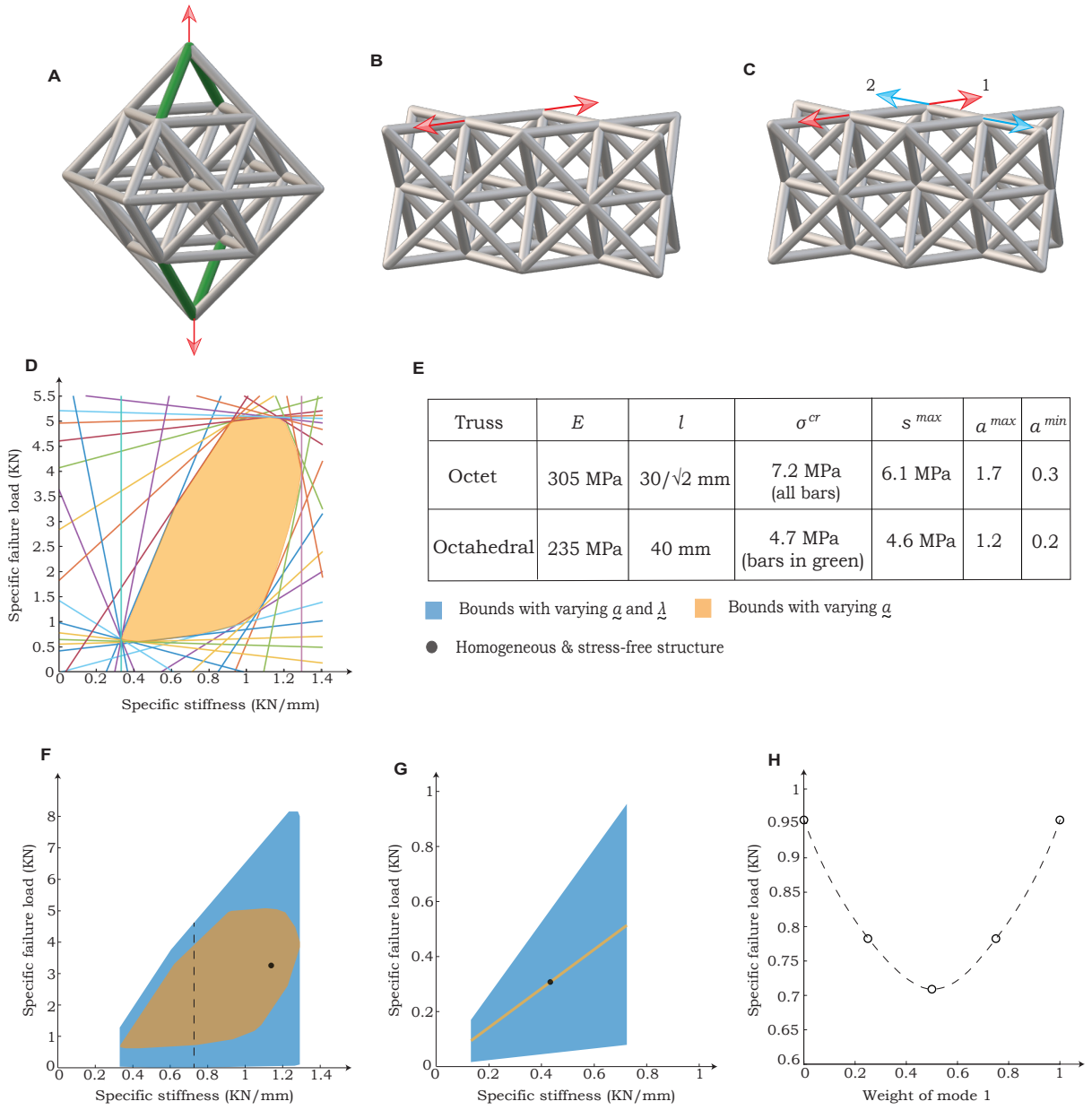

Figure 2.1: Optimal design of failure load and stiffness: ***(a)*** *Octahedral truss loaded along a single mode, in which failure occurs in a bar in green.* ***(b)*** *and* ***(c)*** *Octet truss loaded along a single mode and two modes, respectively, where any bar can fail in tension.* ***(d)*** *Construction of bounds on specific (per unit relative density) failure load and specific stiffness for the octahedral truss with varying cross-sectional areas alone.* ***(e)*** *Table indicating parameters of optimization for both trusses.* s^{max} *represents the maximum allowed magnitude of pre-stress in a bar.* a^{max} *and* a^{min} *are the maximum and minimum values* a_α *can take.* ***(f)*** *and* ***(g)*** *Calculated bounds on attainable specific load to failure and specific stiffness, for the octahedral truss and octet truss loaded along a single mode. The dashed line indicates the specific stiffness of the octahedral truss experimentally tested.* ***(h)*** *Variation of maximum value of weighted specific failure load with weight associated to mode 1, for the octet truss with two symmetric loading modes.*

obtain the force carried by the α^{th} bar to be Tf_α where f_α is a dimensionless quantity depending on the topology of the truss. The total force in this bar is $Tf_\alpha + \sum_j \lambda_j A_\alpha s_\alpha^j$ where A_α is the cross-sectional area of the α^{th} bar. The whole structure is safe if this force is less than the critical failure load $F_\alpha^{\text{cr}} = A_\alpha \sigma_\alpha^{\text{cr}}$ in that bar. It follows that the failure load – the applied load at which any bar fails – is given by

$$T_{\text{cr}} = A \min_{\{\beta:\ f_\beta > 0\}} a_\beta \frac{\sigma_\beta^{\text{cr}} - \sum_j \lambda_j s_\beta^j}{f_\beta} \tag{2.2}$$

where we denote $A_\alpha = A a_\alpha$ for some non-dimensional area ratio a_α. Further, the stiffness/ modulus of the structure is given by

$$M = \frac{A}{\sum_\alpha \frac{l_\alpha f_\alpha^2}{E a_\alpha}} \tag{2.3}$$

where l_α is the length of the α^{th} bar and E the elastic modulus of the solid material.

It is possible to show that the relative density, $\overline{\rho}$ of a truss with fixed length of the bars scales as A as long as $\sum_\alpha a_\alpha = b$ so that $\overline{\rho} = A\rho_o$ where ρ_o depends on the truss geometry and length of a bar. In particular, if all the bars are uniform (with length l and cross-sectional area A), the relative density is $6\frac{\sqrt{2}A}{l^2}$ $(7\frac{A}{\sqrt{2}l^2})$ for the octet (octahedral) truss in Fig. 2.1.

Therefore, we obtain the expressions for the specific failure load (ratio of failure load to relative density) and specific stiffness (ratio of stiffness to relative density) as

$$\overline{T}_{\text{cr}} = \min_{\{\beta:\ f_\beta > 0\}} \frac{a_\beta}{\rho_o} \frac{\sigma_\beta^{\text{cr}} - \sum_j \lambda_j s_\beta^j}{f_\beta}, \tag{2.4}$$

$$\overline{M} = \frac{1}{\rho_o} \frac{1}{\sum_\alpha \frac{l f_\alpha^2}{E a_\alpha}}. \tag{2.5}$$

Previous work has considered optimizing and bounding the specific stiffness $\overline{M}$ by varying the non-dimensional cross-sectional areas a_α subject to the constraint $\sum_\alpha a_\alpha = b$. In this work, we focus on a combination of the specific stiffness $\overline{M}$ and specific failure load $\overline{T}_{\text{cr}}$, while varying non-dimensional area a_α ($\sum a_\alpha = b$) and pre-stress λ_j. A difficulty in doing so is that the specific failure load is itself defined through a variational principle – this makes usual approaches to optimization which requires the computation of the sensitivity difficult. Therefore, we approximate it as

$$\overline{T}_{\text{cr}} \approx \left(\sum_{\{\beta:\ f_\beta > 0\}} \left(\frac{a_\beta}{\rho_o} \frac{\sigma_\beta^{\text{cr}} - \sum_j \lambda_j s_\beta^j}{f_\beta} \right)^{-p} \right)^{-1/p}, \tag{2.6}$$

for p large enough (we take p=5 in our calculations).

We find bounds on all attainable values of $\overline{T}_{\text{cr}}, \overline{M}$ that can be obtained by varying a_α, λ_j. Given any γ_1 and γ_2, we maximize the objective function $O = \gamma_1 \overline{T}_{\text{cr}} + \gamma_2 \overline{M}$ to find $O^{\max}$ using established methods (we find the sensitivity using the adjoint method and avoid local minima by taking multiple initial guesses; details in Methods section). It then follows that for any given $\{a_\alpha, \lambda_j\}$, $\gamma_1 \overline{T}_{\text{cr}}(a_\alpha, \lambda_j) + \gamma_2 \overline{M}(a_\alpha, \lambda_j)$ lies in the half plane $\gamma_1 \overline{T}_{\text{cr}} + \gamma_2 \overline{M} \leq O^{\max}$. The intersection of all such half planes (for all values of γ_1, γ_2) defines an outer bound on all possible values of $\overline{T}_{\text{cr}}(a_\alpha, \lambda_j), \overline{M}(a_\alpha, \lambda_j)$. This construction is shown in Fig. 2.1(D), using the constraints on design mentioned in Fig. 1.2(E). It is an outer bound because all attainable values lie in the set, but it is not guaranteed by the argument above that all points inside the set are feasible. However, the points on the boundary that correspond to unique points where the tangent touches the set are in fact feasible, i.e., it is possible to find the distribution of non-dimensional areas a_α and intensities of states of self-stress λ_j that result in specific failure load and specific stiffness indicated by these points. This is important because extremal properties are likely to occur at such points.

Our analysis shows that it is possible to significantly expand the attainable specific failure load and specific stiffness values in trusses, by varying the non-dimensional areas and pre-stress of the bars (Figures 2.1(F) and 2.1(G)). The points marked in black indicate the specific failure load and specific stiffness for a uniform truss with no pre-stress. The yellow region (line in the case of the octet truss) gives bounds on all possible values of specific failure load and specific stiffness that can be obtained by varying the non-dimensional areas while keeping the pre-stress uniformly zero (i.e., varying a_α subject to the constraint $\sum_\alpha a_\alpha = b$ with $\lambda_j = 0$). The blue region gives bounds on all possible values of specific failure load and specific stiffness that can be obtained by varying both non-dimensional areas and pre-stress (i.e., varying a_α subject to the constraint $\sum_\alpha a_\alpha = b$ and λ_j). Here, the pre-stress does not affect the range of specific stiffness that the truss can attain. Instead, internal stresses can significantly increase the specific failure load. By varying the distributions of non-dimensional areas and pre-stress, one can increase the specific stiffness of the octet truss by a factor two and simultaneously increase its specific failure load by a factor three, within the constraints of design mentioned in Fig. 2.1(E).

Finally, we study the case in which an octet truss is loaded in multiple modes (Fig. 2.1(C)). In such situations, it is natural to seek the Pareto optimal or the envelope of optimal values for various weights of the different loading modes. Consider r loading modes and suppose we assign weights/ intensities $w_i,\ i = 1, \ldots r, w_i > 0,\ \sum w_i = 1$ for the different modes. Then, the formulae above are easily generalized as

$$\overline{T}_{\text{cr}} = \sum_i w_i \min_{\{\beta:\ f_{i,\beta} > 0\}} \frac{a_\beta}{\rho_o} \frac{\sigma_\beta^{\text{cr}} - \sum_j \lambda_j s_\beta^j}{f_{i,\beta}}, \tag{2.7}$$

$$\overline{M} = \sum_i \frac{w_i}{\rho_o} \frac{1}{\sum_\alpha \frac{l f_{i,\alpha}^2}{E a_\alpha}}. \tag{2.8}$$

We find the Pareto optimal by considering all possible weights. Fig. 2.1(H) shows representative results for the octet truss for a combination of two modes of loading shown in Fig. 2.1(C).

In this section, we calculated bounds on attainable specific failure load and specific stiffness. However, in order to design a truss with a particular property within these bounds, one can minimize a norm of the difference between eq. (2.4) or eq. (2.5) and the required property using a sensitivity analysis similar to the one described in the Methods section. We would then arrive at distributions a_α and λ_j that result in specific failure load/ stiffness close to or at the desired value. For a truss with a given relative density $\overline{\rho}$ and non-dimensional area distribution a_α, the distribution of cross-sectional areas of bars can be calculated as $A_\alpha = A a_\alpha$, where $\overline{\rho} = A\rho_o$.

2.4 Experimental results

To demonstrate the principles described above, we first choose a triangular lattice (Fig. 2.2(A)), which is part of a planar section of the octet truss with several unit cells stacked along two directions. This geometry is statically indeterminate with three states of self-stress. We then validate the model in three dimensions, using an octahedral truss, with nine states of self-stress (Fig. 2.2(B)). Since prior work has studied stiffness in detail thirty, here we focus on maximizing the failure load with respect to the distribution of internal stress λ_j for a given distribution of area a_α and relative density $\overline{\rho}$. Internal stress distributions as a result of this optimization (see algorithm in the Methods section) are qualitatively indicated on samples in Figures 2.2(A) and 2.2(B). The bars in red are in tension while those in blue are under compression. The octahedral truss considered here has a specific stiffness value and maximized specific failure load that lie on the dashed line indicated in Fig. 2.1(F). The specimens are fabricated using a Stratasys Connex500 multi-material 3D-printer, with the bars made of DM8530-GREY60 material and the soft joints with TangoBlackPlus (TB) thirtytwo. The length of each bar is 40 mm.

Any statically indeterminate structure can be internally pre-stressed to a desired distribution, by inducing local pre-strain in selected bars. This is possible because the principle of superposition applies in the limit of small deformations. In our examples, we introduce local pre-compression in three of the bars in the triangular lattice and in four bars of the octahedral truss. These bars (indicated by green arrows in Figures 2.2(A) and 2.2(B)) are initially pre-compressed, but are then subjected to tensile stresses when the truss is loaded. The magnitude of the local pre-compression on these bars is determined using superposition, so that the final stress-state of the lattices matches the desired distribution of self-stress, obtained from numerical simulations (see Methods section).

To emulate the effect of local pre-compression, we introduce hinge mechanisms in the center of these

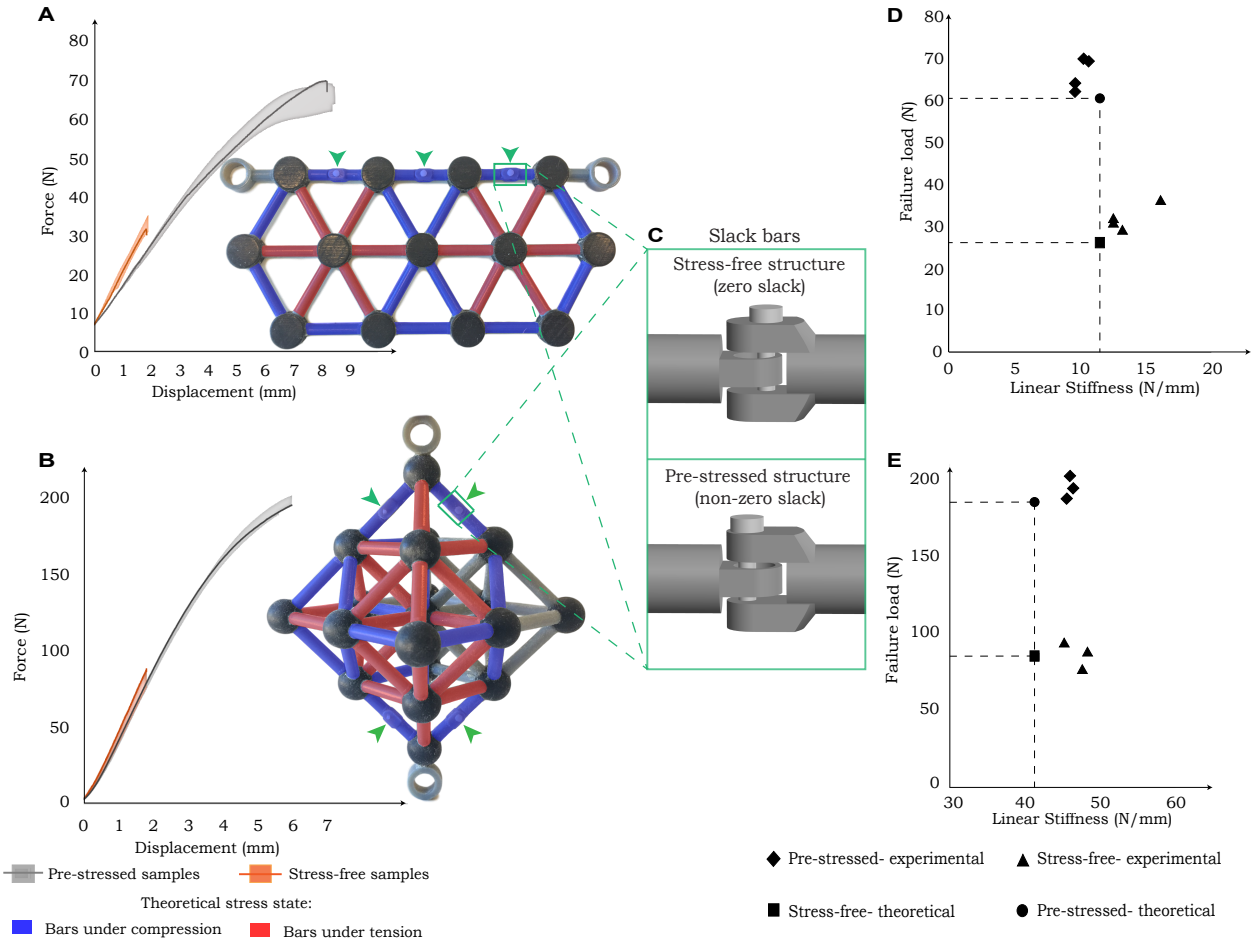

Figure 2.2: Experiments: ***(a)*** *and* ***(b)*** *Experimental results from tensile tests on the triangular lattice and octahedral truss, respectively. The bold line indicates the data for a particular specimen, while the shaded area indicates all test data.* ***(c)*** *Close-up of the hinge that enables the slack bar – note that the position of the pin is changed.* ***(d)*** *and* ***(e)*** *The failure load and stiffness – both experimental and theoretical – for the specimens with and without pre-stress for the triangular lattice and octahedral truss, respectively.*

bars, allowing them to buckle slightly and remain unstressed before loading is applied. We call such bars the *slack* bars (Fig. 2.2(C)). The amount of slack in each mechanism is designed to match the displacement needed for its locally pre-compressed bar to reach zero stress. Hence, as the structure is loaded, the tensile displacements in the mechanism compensate the slack, eventually engaging the pins in each hinge. From this point onwards, the stress state of the truss is identical to that expected from the desired pre-stressed structure under the same load. We verify this experimentally by ensuring that the global *effective* stiffness of the structures tested match the expected values. In control experiments, we introduce hinges with no slack, to test the failure of structures with no initial pre-stress. Importantly, the hinge mechanisms also act as *defects* in the bars, and localize failure away from the joints of the truss, at a fixed load level.

The lattices are tested in an Instron testing machine, operated in displacement control. The results of the tensile tests, performed to failure for both the triangular lattice (Fig. 2.2(A)) and octahedral truss (Fig. 2.2(B)), show a significant difference between the samples with and without slack in the hinge mechanisms. The resulting stiffness and failure load are compared to the theoretically predicted values (Figures 2.2(D) and 2.2(E)), showing excellent agreement. To obtain the theoretical values, individual bars are fabricated using the same method and tested in tension at the same strain rate. We obtain a linear stiffness of 115.28 ± 1.91 N/mm and 21.12 ± 0.64 N/mm for the regular and slack bar, respectively, and the maximum load to failure in the slack bar is 15.12 ± 1.56 N.

We obtain a two-fold increase (107.21% for the triangular lattice, and 127.44% for the octahedral truss) in the specific failure load of the pre-stressed structures, as compared to the structures with no pre-stress. However, the stiffness of the structures with and without pre-stress remains almost constant, as intended. Consequently, there is a four-fold increase in the work of fracture.

2.5 Discussion

Our analysis expresses failure load of architected materials in terms of geometrical parameters that can be used in design. This approach decouples stiffness from strength and allows the calculation of global optima using sensitivity analysis. As stiffness and failure load scale linearly with density, for stretch dominated structures, the approach can be used to design arbitrarily lightweight structures. We show that the design bounds can be reached in truss-like structures introducing internal stresses and varying the distribution of cross sectional areas within the structures. We demonstrate this technique on the octet and octahedral trusses. While these are relatively simple examples, they illustrate the principle. The formulas and the methods presented are applicable to trusses of arbitrary complexity. The proposed design approach could be further extended in the future to include more complicated loading conditions (e.g., complex loading histories or dynamic solicitations) and expand materials' functionalities. For example, engineering pre-stress can be used to improve

impact energy absorption and failure of architected foams. The addition of pre-stresses can also be an important tool to engineer large shape changes in materials thirtysix. Finally, internally stressed structures can be studied to create predetermined failure paths in a structure, which can be useful to prolong the life of a product.

2.6 Methods

2.6.1 Equilibrium equations

In this section, we provide details to obtain the force in any bar of a pre-stressed truss in the presence of external loads.

Consider a truss with b bars and n joints or nodes. Let $\underset{\sim}{y}_i^0$ denote the position of the ith joint in the absence of any self-stress and any external load (i.e., the ideal truss). Thus, the length L_{ij}^0 of the bar connecting the ith and jth joint is given by $|\underset{\sim}{y}_j^0 - \underset{\sim}{y}_i^0|$.

A state of self-stress can be induced in the truss by changing the natural length of the bar connecting the ith and jth joint to be L_{ij} that is different from the ideal natural length L_{ij}^0. Further, we can apply external force $\underset{\sim}{F}_i^{ext}$ at the ith joint. The new positions of the joints, $\{\underset{\sim}{y}_i\}$, can be obtained from solving the equilibrium equations. Assuming that each bar is made of a linear elastic material, the equilibrium of the ith joint is given by

$$\sum_j K_{ij} \left(|\underset{\sim}{y}_j - \underset{\sim}{y}_i| - L_{ij} \right) \frac{\left(\underset{\sim}{y}_j - \underset{\sim}{y}_i \right)}{|\underset{\sim}{y}_j - \underset{\sim}{y}_i|} - \underset{\sim}{F}_i^{ext} = 0 \tag{2.9}$$

where K_{ij} denotes the stiffness of the bar connecting the joints indexed i and j (with $K_{ij} = 0$ if there is no such bar).

These equations are nonlinear in the positions. However, if the displacement of the joints is small enough (as for example, if the strain to failure is small as is true in our situation), we can linearize around the natural positions. To do so, we set $\underset{\sim}{y}_i = \underset{\sim}{y}_i^0 + \underset{\sim}{u}_i$ and $L_{ij}^0 = L_{ij} + e_{ij}$, and linearize the equilibrium equation (2.9) in $\{\underset{\sim}{u}_i\}$ and $\{e_{ij}\}$. We obtain

$$\sum_j K_{ij} \left(\underset{\sim}{t}_{ij} . (\underset{\sim}{u}_j - \underset{\sim}{u}_i) - e_{ij} \right) \underset{\sim}{t}_{ij} = \underset{\sim}{F}_i^{ext}, \tag{2.10}$$

where $\underset{\sim}{t}_{ij}$ is the unit vector tangent to the bar given by $\frac{\underset{\sim}{y}_j^0 - \underset{\sim}{y}_i^0}{|\underset{\sim}{y}_j^0 - \underset{\sim}{y}_i^0|}$. We can now exploit the linearity of the equation and write $\underset{\sim}{u}_i = \underset{\sim}{u}_i^F + \underset{\sim}{u}_i^S$ where $\underset{\sim}{u}_i^F, \underset{\sim}{u}_i^S$ solve

$$\sum_j K_{ij} \left(\underset{\sim}{t}_{ij} . (\underset{\sim}{u}_j^F - \underset{\sim}{u}_i^F) \right) \underset{\sim}{t}_{ij} = \sum_j \overline{K}_{ij} \underset{\sim}{u}_j^F = \underset{\sim}{F}_i^{ext}, \tag{2.11}$$

$$\sum_j K_{ij} \left(\underset{\sim}{t}_{ij} . (\underset{\sim}{u}_j^S - \underset{\sim}{u}_i^S) - e_{ij} \right) \underset{\sim}{t}_{ij} = 0, \tag{2.12}$$

with $\overline{K}_{ij} = \left(\underset{\sim}{t}_{ij} \otimes K_{ij}\underset{\sim}{t}_{ij}\right) - \delta_{ij}\left(\sum_k \underset{\sim}{t}_{jk} \otimes K_{jk}\underset{\sim}{t}_{jk}\right)$. The first equation above finds the displacements due to the external force in the absence of self stress while the latter finds the displacements due to self-stress in the absence of the external forces.

Now, note that $K_{ij}\left(\underset{\sim}{t}_{ij}.(\underset{\sim}{u}_j^S - \underset{\sim}{u}_i^S) - e_{ij}\right)$ is the force in the bar connecting joints indexed i and j in the pre-stressed structure without the application of an external load. Representing this force by P_{ij}^S, eq. (2.12) becomes $\sum_j P_{ij}^S \underset{\sim}{t}_{ij} = 0$. Switching to an indexing with respect to bars, eq. (2.12) further simplifies to

$$\sum_\alpha C_{i\alpha} P_\alpha^S = 0, \tag{2.13}$$

where C represents a connectivity matrix of size $dn \times b$ and $\alpha = 1, \ldots, b$. If the α^{th} bar starts or ends at the joint indexed i, then the vector in the α^{th} column of C from its $d(i-1)+1^{th}$ row to its di^{th} row is given by the unit vector $\underset{\sim}{t}_\alpha$, which represents the direction cosines of the bar pointing away from the joint i. The vector is zero otherwise. The null-space of matrix C indicates states of self-stress in the system, and the orthonormal vectors that span this null-space describe the different states of self-stress in the truss.

Therefore, the total force in the α^{th} bar is given by

$$P_\alpha = P_\alpha^F + \sum_m \lambda_m A_\alpha s_\alpha^m, \tag{2.14}$$

where $P_\alpha^F = K_{ij}(\underset{\sim}{u}_j^F - \underset{\sim}{u}_i^F).\underset{\sim}{t}_{ij}$ is the force in the α^{th} bar due to the external force. Finally, consider a loading mode on the structure with an applied force T. It is easy to calculate a non-dimensional quantity f_α associated with the α^{th} bar such that eq. (2.14) becomes

$$P_\alpha = T f_\alpha + \sum_m \lambda_m A_\alpha s_\alpha^m. \tag{2.15}$$

Here, θf_α is the force in the α^{th} bar when the initially stress-free structure is loaded along the mode with a unit external load, where θ is a unit force.

To illustrate the states of self-stress, consider the structure shown in Fig. 2.3 with a uniform stiffness distribution. As a result, there are three states of self-stress represented by the linearly independent vectors,

$\underset{\sim}{s}^1 = [-1,\ -1,\ 1,\ -1,\ 1,\ -1,\ 1,\ 0,\ -1,\ 1,\ 0,\ 0,\ 0,\ -1,\ 1,\ 0,\ 1,\ 0,\ 0,\ 0,\ 0,\ 0,\ 0,\ 0,\ 0,\ 0]^T$,

$\underset{\sim}{s}^2 = [0,\ 0,\ 0,\ 0,\ 0,\ -1,\ 1,\ 1,\ -1,\ -1,\ -1,\ -1,\ -1,\ 0,\ 1,\ 1,\ 0,\ 1,\ 0,\ 1,\ 0,\ 0,\ 0,\ 0,\ 0,\ 0]^T$,

$\underset{\sim}{s}^3 = [0,\ 0,\ 0,\ 0,\ 0,\ -1,\ 1,\ 1,\ -1,\ -1,\ 0,\ -2,\ 0,\ 0,\ 1,\ 1,\ 0,\ 0,\ 1,\ 0,\ -1,\ -1,\ -1,\ 1,\ 1,\ 1]^T$.

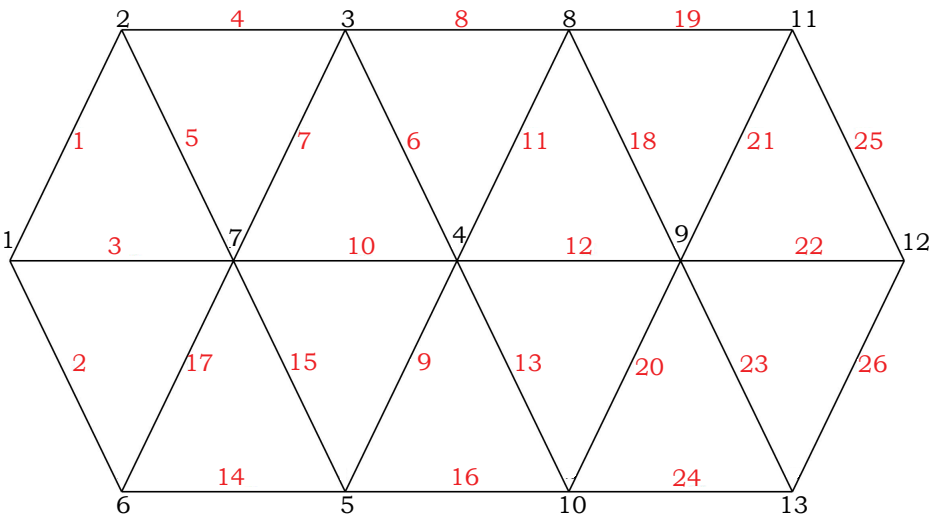

Figure 2.3: Triangular lattice: *Example of a statically indeterminate 2-D truss with 13 joints (labeled in black) and 26 bars (labeled in red).*

2.6.2 Sensitivity analysis

2.6.2.1 Sensitivity of specific failure load

Consider a matrix $\underset{\sim}{V}_i$ of size b_i x d, where b_i is the number of elements in the set $\{\beta\}$ for the i^{th} loading mode. Let the j^{th} row in $\underset{\sim}{V}_i$, $\underset{\sim}{v}_{i,j}$ be the difference in displacement vectors (due to the external force) of joints associated with the bar given by the j^{th} element in the corresponding set $\{\beta\}$. From eq. (2.11), it is easy to find the relation $\underset{\sim}{V}_i = \underset{\sim}{J}\underset{\sim}{F}_i$, where the k^{th} row of $\underset{\sim}{F}_i$ is the external force at the k^{th} joint for a unit load along the i^{th} mode. Note that $\underset{\sim}{J}$ is a matrix of size b_i x n. With this revised notation, the specific failure load considering failure of a bar in tension can be written as

$$\overline{T}_{cr} = \sum_i \frac{\theta w_i}{EA\rho_o} \left(\sum_{\{\beta:\ f_\beta > 0\}} \left(\frac{l(\sigma_\beta^{\mathrm{cr}} - \sum_j \lambda_j s_\beta^j)}{\underset{\sim}{v}_{i,\beta} \cdot \underset{\sim}{t}_\beta} \right)^{-p} \right)^{-1/p}, \tag{2.16}$$

where $\underset{\sim}{t}_j$ is the unit vector along the bar indexed j in the corresponding set $\{\beta\}$. The sensitivity of specific failure load with the internal stress distribution can be easily calculated as

$$\frac{\partial \overline{T}_{cr}}{\partial \underset{\sim}{\lambda}} = \sum_i \frac{\theta w_i}{EA\rho_o}\Bigg[\left(\sum_{\{\beta:\ f_\beta>0\}}\left(\frac{l(\sigma_\beta^{\mathrm{cr}} - \sum_j \lambda_j s_\beta^j)}{\underset{\sim}{y}_{i,\beta}.\,\underset{\sim}{t}_\beta}\right)^{-p}\right)^{\frac{-(p+1)}{p}} \left(\sum_{\{\beta:\ f_\beta>0\}}\left(\frac{l(\sigma_\beta^{\mathrm{cr}} - \sum_j \lambda_j s_\beta^j)}{\underset{\sim}{y}_{i,\beta}.\,\underset{\sim}{t}_\beta}\right)^{-p-1}\left(\frac{-l\underset{\sim}{s}_\beta}{\underset{\sim}{y}_{i,\beta}.\,\underset{\sim}{t}_\beta}\right)\right)\Bigg]. \quad (2.17)$$

However, $\underset{\sim}{Y}_i$ and hence $\underset{\sim}{y}_{i,j}$ depend on the stiffness distribution within the truss. In order to calculate the sensitivity of eq. (2.16) with respect to a_α, we modify eq. (2.16) by introducing the method of Lagrange multipliers, as follows

$$\overline{T}_{cr} = \sum_i \frac{\theta w_i}{EA\rho_o}\left(\sum_{\{\beta:\ f_\beta>0\}}\left(\frac{l(\sigma_\beta^{\mathrm{cr}} - \sum_j \lambda_j s_\beta^j)}{\underset{\sim}{y}_{i,\beta}.\,\underset{\sim}{t}_\beta + \underset{\sim}{B}_\beta.(\underset{\sim}{y}_{i,\beta} - \underset{\sim}{J}_\beta \underset{\sim}{F}_i)}\right)^{-p}\right)^{-1/p}, \quad (2.18)$$

where $\underset{\sim}{B}_\beta$ represents the β^{th} Lagrange multiplier of size 1 x d and $\underset{\sim}{J}_\beta$ represents the β^{th} row of $\underset{\sim}{J}$. The sensitivity of $\overline{T}_{cr}$ with respect to a_α, $\alpha = 1, 2, \ldots, b$ is calculated as

$$\frac{\partial \overline{T}_{cr}}{\partial a_\alpha} = \sum_i \frac{\theta w_i}{EA\rho_o}\left[\left(\sum_{\{\beta:\ f_\beta>0\}}\left(\frac{l(\sigma_\beta^{\mathrm{cr}} - \sum_j \lambda_j s_\beta^j)}{\underset{\sim}{y}_{i,\beta}.\,\underset{\sim}{t}_\beta}\right)^{-p}\right)^{\frac{-(p+1)}{p}}\left(\sum_{\{\beta:\ f_\beta>0\}}\left(\frac{l(\sigma_\beta^{\mathrm{cr}} - \sum_j \lambda_j s_\beta^j)}{\underset{\sim}{y}_{i,\beta}.\,\underset{\sim}{t}_\beta}\right)^{-p-1} l D_i\right)\right]. \quad (2.19)$$

For each loading mode given by the index i,

$$D_i = \frac{\dfrac{\partial \sigma_\beta^{cr}}{\partial a_\alpha} - \underset{\sim}{\lambda}.\left(\dfrac{\partial \underset{\sim}{s}_\beta}{\partial a_\alpha}\right)}{\underset{\sim}{y}_{i,\beta}.\,\underset{\sim}{t}_\beta} - \frac{\left(\sigma_\beta^{\mathrm{cr}} - \sum_j \lambda_j s_\beta^j\right)\left(\underset{\sim}{t}_\beta.\dfrac{\partial \underset{\sim}{J}_\beta}{\partial a_\alpha}\underset{\sim}{F}_i\right)}{\left(\underset{\sim}{y}_{i,\beta}.\,\underset{\sim}{t}_\beta\right)^2}. \quad (2.20)$$

Note that we avoid computing $\frac{\partial \underset{\sim}{y}_{i,\beta}}{\partial a_\alpha}$ by choosing $\underset{\sim}{B}_\beta$ to be $-\underset{\sim}{t}_\beta$.

2.6.2.2 Sensitivity of specific stiffness

Similarly to the procedure carried out in the previous subsection, the specific stiffness can be written as

$$\overline{M} = \sum_i \frac{\theta^2 w_i l}{EA^2\rho_o}\frac{1}{\sum_\alpha a_\alpha \left(\underset{\sim}{y}_{i,\alpha}.\,\underset{\sim}{t}_\alpha\right)^2 + \underset{\sim}{B}_\alpha.(\underset{\sim}{y}_{i,\alpha} - \underset{\sim}{J}_\alpha \underset{\sim}{F}_i)}. \quad (2.21)$$

Choosing the Lagrange multiplier $\underset{\sim}{B}_\alpha$ to be $-2a_\alpha\left(\underset{\sim}{y}_{i,\alpha}.\,\underset{\sim}{t}_\alpha\right)\underset{\sim}{t}_\alpha$,

$$\frac{\partial \overline{M}}{\partial a_\alpha} = \sum_i \frac{-\theta^2 w_i l}{EA^2\rho_o}\frac{\left(\underset{\sim}{y}_{i,\alpha}.\,\underset{\sim}{t}_\alpha\right)^2 + 2a_\alpha\left(\underset{\sim}{y}_{i,\alpha}.\,\underset{\sim}{t}_\alpha\right)\underset{\sim}{t}_\alpha.\frac{\partial \underset{\sim}{J}_\alpha}{\partial a_\alpha}\underset{\sim}{F}_i}{\left(\sum_\alpha a_\alpha\left(\underset{\sim}{y}_{i,\alpha}.\,\underset{\sim}{t}_\alpha\right)^2\right)^2}. \quad (2.22)$$

We optimize the specific stiffness with respect to a_α subject to the constraints, $\sum_\alpha a_\alpha = b$ and $a^{min} \leq a_\alpha \leq a^{max}$, $\alpha = 1, 2, \ldots, b$, using algorithm 1. We optimize $\overline{T}_{cr}$ with respect to both a_α and λ_j, subject to the additional constraints $|\sum_j \lambda_j s_\alpha^j| \leq s^{max}$, using algorithm 2.

2.6.3 Experimental details

2.6.3.1 Design of the truss

Figures 2.4(A) and (B) show the design of the truss (without the joints) for the triangular lattice and octahedral truss, respectively. The reduced cross-sectional area at the bars' intersection ensures a decrease in bending resistance. To ensure that failure does not occur at the joints when the structure is loaded, we fabricate them using a softer material (TangoBlack, TB, by Stratasys). During testing, the structures are fastened to an Instron mechanical testing machine using bolts that pass through the loops at the two corners of the structure (Figures 2.4(C) and (D)). The close-up image in Fig. 2.4(E) shows an expected fracture of a slack bar at the thinnest region.

In order to calculate the internal stress distribution that optimizes the failure load, we first measure the properties of a single bar. We perform tensile tests on the samples shown in Figures 2.4(F) and (G) to measure the linear stiffness of a regular bar and a slack bar. It is to be noted that the effective length of these bars is twice that of one bar in a truss. Hence, we double the measured stiffness to calculate the stiffness of just one bar in each truss. We calculate the linear stiffness of each sample as the slope of the straight line portion in its force-position data for a fixed displacement. We use these values as input to maximize the failure load in the following subsection.

2.6.3.2 Maximum failure load and slack length distribution

We calculate optimal distributions of internal stress $\underset{\sim}{\lambda}_1^*$ and $\underset{\sim}{\lambda}_2^*$ that maximize the failure load for the structures shown in Figures 3(A) and (B), respectively. We assume a maximum pre-compression/ pre-extension limit in each bar of 0.97 mm ($\approx$ 2.5% maximum pre-strain) for the triangular lattice and 0.85 mm ($\approx$ 2.1% maximum pre-strain) for the octahedral truss. The failure load is optimized with the constrained gradient based method, using eq. (2.17). We use algorithm 2 to calculate the internal stress distributions $\underset{\sim}{\lambda}_1^*$ and $\underset{\sim}{\lambda}_2^*$, that maximize the failure loads in each structure. This desired increase in failure load can be achieved in the triangular lattice by introducing a slack length of 2.28 mm in each of the three slack bars indicated in Fig. 3(A)– using algorithm 3. Similarly, we introduce a slack length of 1.4 mm in each of the four slack bars in Fig. 3(B).

2.6.3.3 Experimental setup

Figures 2.4(C) and (D) show the triangular lattice and octahedral truss loaded using the Instron tensile testing machine. Since the fixtures are constrained to move vertically, this process replicates

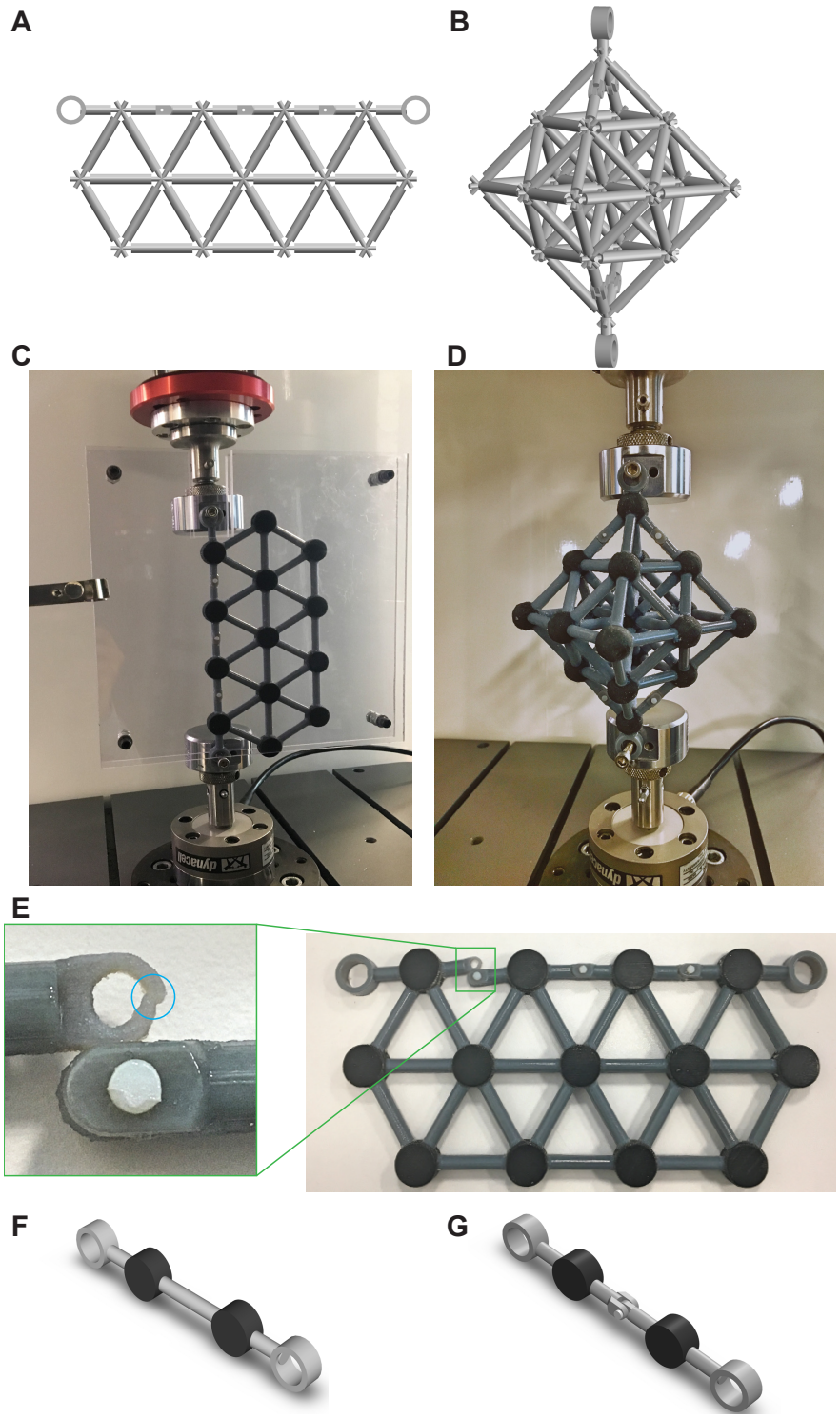

Figure 2.4: Design of samples: ***(a)*** *and* ***(b)*** *Models of bars for the triangular lattice and octahedral truss, respectively.* ***(c)*** *and* ***(d)*** *The triangular lattice and octahedral truss loaded using the Instron machine.* ***(e)*** *A triangular lattice sample post testing. Notice fracture in the slack bar indicated by the blue circle in the close-up image.* ***(f)*** *and* ***(g)*** *Model of a regular bar and a slack bar, respectively.*

Table 2.1: Experiments vs theory– Triangular lattice

Quantity	**Experimental results**	**Theoretical results**
Failure load (stress-free)	31.89 ± 3.01 N	26.07 N
Failure load (internally stressed)	66.13 ± 3.89 N	60.30 N
Stiffness (stress-free)	13.64 ± 1.72 N/mm	11.55 N/mm
Stiffness (internally stressed)	10.07 ± 0.52 N/mm	11.55 N/mm
Percentage increase in failure load	**107.21 %**	**131.30 %**

Table 2.2: Experiments vs theory– Octahedral truss

Quantity	**Experimental results**	**Theoretical results**
Failure load (stress-free)	86.03 ± 8.67 N	85.14 N
Failure load (internally stressed)	195.59 ± 7.39 N	185.74 N
Stiffness (stress-free)	47.12 ± 1.65 N/mm	41.37 N/mm
Stiffness (internally stressed)	46.02 ± 0.43 N/mm	41.37 N/mm
Percentage increase in failure load	**127.44 %**	**118.16 %**

the desired mode of loading. As we load the triangular lattice, some of the bars compress and naturally tend to buckle out of plane at the joints. This happens due to the negligible bending resistance offered by the joints. In order to make sure all the bars remain in the same plane, which is the plane of view, we constrain the sample between two glass slides with lubricated internal surfaces. The lubrication helps reduce friction between the sample and the glass, without adding any in-plane external force. Further, the spacing between the glass slides is held constant using a fixed number of standard nuts and washers between them. Finally, the glass slides are held stationary with respect to the machine using clamps that are attached to the Instron machine. The two ends are moved vertically away with respect to each other, quasi-statically, till the first bond breaks. The displacement rate is set at 0.5 mm/s. We then measure the peak load at which this failure occurs from the recorded data.

Tables 2.1 and 2.2 summarize the experimental results (mean values with standard deviations) against the corresponding theoretical predictions. Note that we calculate the stiffness of each structure as slope of the straight line regions for a fixed displacement in Figures 3(A) and (B).

2.6.4 Algorithms

Algorithm 1 Optimization (minimization) with respect to $\underline{a}$

Objective function $\Rightarrow O\ (\underline{a})$, fix $\underline{\lambda} = \underline{0}$
Randomly select 100 points for $\underline{a}$ such that the constraints are satisfied
Evaluate O at all 100 points
Let $\underline{a}_i$ represent the vector of stiffness at the i^{th} iteration.
Identify $\underline{a}_1$ such that $O\ (\underline{a}_1)$ is minimum of all 100 values
i=1 (step)
Evaluate $\underline{G}_{a,i}$ (Gradient of O with $\underline{a}$ at $\underline{a}_i$) and $\underline{G_p}_{a,i}$ ($\underline{G}_{a,i}$ projected on active constraints)
while (norm ($\underline{G}_{a,i}$)>0) OR (norm ($\underline{G_p}_{a,i}$)>0) **do**
    $\underline{a}_{i+1} = \underline{a}_i - e\ \underline{G}$ {$\underline{G} = \underline{G}_{a,i}$, if $\exists\ e > 0$ s.t. $\underline{a}_{i+1}$ is feasible; $\underline{G} = \underline{G_p}_{a,i}$, otherwise}
    If $\underline{a}_{i+1}$ violates a constraint, recalculate $\underline{a}_{i+1}$ on boundary
    while ($O(\underline{a}_{i+1}) - O(\underline{a}_i)$)>0 **do**
        $e = \tau\ e$, where $0 < \tau < 1$
        Re-evaluate feasible $\underline{a}_{i+1}$
    end
    i=i+1
    Evaluate $\underline{G}_{a,i}$ and $\underline{G_p}_{a,i}$
end
$\underline{a}^* = \underline{a}_i$

Algorithm 2 Optimization (minimization) with respect to $\underline{a}$ and $\underline{\lambda}$

Objective function $\Rightarrow O\ (\underline{a}, \underline{\lambda})$
Randomly select 100 points for $(\underline{a}, \underline{\lambda})$ such that the constraints are satisfied
Evaluate O at all 100 points
Let $(\underline{a}_i,\ \underline{\lambda}_i)$ represent the stiffness and internal stress distribution vectors at the i^{th} iteration.
Identify $(\underline{a}_1, \underline{\lambda}_1)$ such that $O\ (\underline{a}_1, \underline{\lambda}_1)$ is minimum of all 100 values
i=1 (step)
Evaluate $\underline{G}_{a,i}$, $\underline{G}_{\lambda,i}$ (Gradient of O with $\underline{a}$ at $\underline{a}_i$ and with $\underline{\lambda}$ at $\underline{\lambda}_i$, respectively), $\underline{\underline{G_p}}_{a,i}$ and $\underline{\underline{G_p}}_{\lambda,i}$ ($\underline{G}_{a,i}$ and $\underline{G}_{\lambda,i}$ projected on active constraints, respectively)
while (norm $(\underline{G}_{a,i})$>0 AND norm$(\underline{\underline{G_p}}_{a,i})$>0) OR (norm $(\underline{G}_{\lambda,i})$>0 AND norm $(\underline{\underline{G_p}}_{\lambda,i})$>0) **do**
    $\underline{a}_{i+1} = \underline{a}_i - e_1\ \underline{G}$ {$\underline{G} = \underline{G}_{a,i}$, if $\exists\ e_1 > 0$ s.t. $\underline{a}_{i+1}$ is feasible; $\underline{G} = \underline{\underline{G_p}}_{a,i}$, otherwise}
    If $\underline{a}_{i+1}$ violates a constraint, recalculate $\underline{a}_{i+1}$ on boundary
    while $(O(\underline{a}_{i+1}, \underline{\lambda}_i) - O(\underline{a}_i, \underline{\lambda}_i))$>0 **do**
        $e_1 = \tau_1 e_1$, where $0 < \tau_1 < 1$
        Re-evaluate feasible $\underline{a}_{i+1}$
    end
    Re-evaluate $\underline{G}_{\lambda,i}$ and $\underline{\underline{G_p}}_{\lambda,i}$
    $\underline{\lambda}_{i+1} = \underline{\lambda}_i - e_2 \underline{G}$ {$\underline{G} = \underline{G}_{\lambda,i}$, if $\exists\ e_2 > 0$ s.t. $\underline{\lambda}_{i+1}$ is feasible; $\underline{G} = \underline{\underline{G_p}}_{\lambda,i}$, otherwise}
    If $\underline{\lambda}_{i+1}$ violates a constraint, recalculate $\underline{\lambda}_{i+1}$ on boundary
    while $(O(\underline{a}_{i+1}, \underline{\lambda}_{i+1}) - O(\underline{a}_{i+1}, \underline{\lambda}_i))$>0 **do**
        $e_2 = \tau_2 e_2$, where $0 < \tau_2 < 1$
        Re-evaluate feasible $\underline{\lambda}_{i+1}$
    end
    i=i+1
    Evaluate $\underline{G}_{a,i}$, $\underline{G}_{\lambda,i}$, $\underline{\underline{G_p}}_{a,i}$ and $\underline{\underline{G_p}}_{\lambda,i}$
end
$(\underline{a}^*, \underline{\lambda}^*) = (\underline{a}_i, \underline{\lambda}_i)$

Algorithm 3 Distribution of slack lengths

1: Assign stiffness k_2 to slack bars and k_1 to the remaining bars. Let the set of indices of slack bars be represented by Set1.
2: Calculate $\underline{\lambda}^*$ from algorithm 2, for this fixed $\underline{a}$
3: **for** i=1: 1: size (Set1) **do**
4: Natural length of bar indexed by Set1(i) $\rightarrow L + 1$ mm
5: Natural lengths of all other bars $\rightarrow L$ mm
6: Resultant equilibrium pre-stress distribution (without external load) $\rightarrow \underline{\lambda}_i$
7: **end**
8: Solve for the optimal solution, $\underline{x}^* = arg\ min_{\underline{x}} |\sum_i x_i \underline{\lambda}_i - \underline{\lambda}^*|^2$, subject to $\underline{x} \geq 0$ and $\underline{x} \leq ub$ (upper bound determined by a maximum pre-strain limit)
9: Distribution of natural lengths: $L + x_i^*$ mm for the i^{th} bar in Set1 and L mm for the rest, where L is the natural length of each bar in the homogeneous structure.
10: Amount of slack in the i^{th} bar in Set1 is x_i^* mm.

Chapter 3

ENGINEERING WAVE SPEED AND STIFFNESS

Research presented in this chapter has been adapted from the following publication:

Injeti, S. S., Bhattacharya, K. & Daraio, C. Tuning acoustic impedance in load-bearing structures. *In preparation* (2021).

3.1 Tuning acoustic impedance in load-bearing structures

3.1.1 Motivation

Acoustic transparency is the capability of a medium to transmit mechanical waves to adjacent media, without scattering. This characteristic can be achieved by carefully engineering the acoustic impedance of the medium – a combination of wave speed and density, to match that of the surroundings. Owing to the strong correlation between acoustic wave speed and static stiffness, it is challenging to design acoustically transparent materials in a fluid, while maintaining their high structural rigidity. In this work, we propose a method to design architected lattices with independent control of the elastic wave speed at a chosen frequency, the mass density, and the static stiffness, along a chosen loading direction. We provide a sensitivity analysis to optimize these properties with respect to design parameters of the structure, that include localized masses at specific positions. We demonstrate the method on five different periodic, three dimensional lattices, to calculate bounds on the longitudinal wave speed as a function of their density and stiffness. We then perform experiments on 3-D printed structures, to validate our numerical simulations. The tools developed in this work can be used to design lightweight and stiff materials with optimized acoustic impedance for a plethora of applications, including ultrasound imaging, wave filtering, and waveguiding.

3.1.2 Introduction

In this work, we present a design approach that decouples the static stiffness of a structure from its elastic wave speed. We apply this method to architected lattices featuring point masses at specific locations, which act as localized scatterers or resonating elements in the dynamic response of these structures.

Architected solids are a class of materials whose macroscopic properties stem from a carefully-engineered *mesostructure*, whose characteristic lengthscale is in between the atomistic one (that dictates the behavior of the constituent material) and the overall size of the system [42]. Com-

monly, these mesostructures are obtained by spatially-repeating a unit cell or repetitive volume element (RVE) that comprises peculiar spatial arrangements of material phases and voids. An engineering-relevant subclass of architected solids are lattice structures, i.e., networks of simple structural elements like trusses [35], shells [120], or plates [11], that show unusual combinations of mechanical properties like high strength and light weight [4]. Most early studies on lattice structures focused on their peculiar mechanics, e.g., on their ability to display mechanisms of inextensional deformation and states of self stress [55, 57], and on their potential structural applications, e.g., as cores of sandwich panels [34, 39]. Lattice structures with increasingly complex architectures can now be additively fabricated in many different materials, from polymers and metals [57, 99], to ceramics [84], composites [103], and cementitious materials [89], and with characteristic lengthscales reaching down to nanometers [7].

Lattice structures are particularly appealing for their response to dynamic loads, since their complex architectures give way to peculiar dispersion properties [100]. In the context of elastic wave propagation, periodic lattices can exhibit bandgaps, i.e., frequency ranges where waves are not allowed to propagate [48, 69, 78, 101, 125]. Beyond this well-known attribute, lattices also exhibit spatial wave manipulation capabilities, e.g., wave anisotropy or directionality [8, 19, 20], negative refraction [115], and topologically-protected backscattering-free waveguiding [121], stemming from intrinsic or carefully-chosen unit cell symmetries that yield mode-rich dispersion relations. In acoustics, microlattice metamaterials immersed in a fluid behave as poroelastic media and interact with ultrasonic waves, leading to local resonance based bandgaps [68, 113] and other wave manipulation effects such as wave focusing [114], with potential applications in the biomedical field [61]. When manufactured at the micro- or nano-scale, lattice architectures can also interact with electromagnetic waves and exhibit photonic gaps [27]. These characteristics, coupled with their structural performance, make lattices appealing as multifunctional systems for mechanical, aerospace, and biomedical applications.

A critical need to translate structured materials into engineering applications is the development of inverse design strategies, to obtain optimal architectures given desired specifications. In dynamics, the dispersion properties of a periodic lattice are often derived from the analysis of a single cell, applying periodic boundary conditions of the Floquet-Bloch type, which impose a dependency on the wavenumber [16, 101]. This approach simplifies the optimization process, and reduces it to the design of a single cell. Most optimization efforts to date target the position in the frequency spectrum and frequency width of elastic bandgaps [6, 12, 44, 52, 54, 80, 106, 112]. In this context, the techniques used are mainly gradient-based topology optimization and genetic algorithms [74]. Fewer studies are dedicated to the optimization of other dispersive properties, e.g., the elastic wave speeds. Topology optimization has been used to design the transient response of one-dimensional

elastic waveguides, based on a sensitivity analysis that uses the adjoint method to calculate the effects of topological changes on the group velocity [31]. A similar technique, albeit applied to frequency-domain equations, is adopted for spatial wave manipulation [3, 29, 98]. In one example, authors design plates with perforations, optimized to control the direction of flexural modes at different frequencies [3]. However, this method avoids the calculation of implicit derivatives that describe the evolution of a mode shape with the cell architecture, an aspect that could be useful for the optimization of mode shape-dependent dispersion characteristics. Furthermore, the studies mentioned are restricted to structures consisting of a single material and void. However, we note that the local addition of a second material with a relatively high density can have drastic effects on the range of wave speeds that can be attained, while maintaining constant the static stiffness.

In this section, we develop a tool to optimize the elastic wave speeds in three-dimensional architected lattices at a fixed frequency of propagation. The key step is a sensitivity analysis to calculate the topological gradient of the elastic group velocity of any particular mode at a chosen frequency of interest, by providing a method to compute the sensitivities of the mode shape together with an adjoint method. These derivatives are also useful in understanding and engineering the rich modal composition exhibited by these 3-D structures at any frequency. We show that analyzing the real and imaginary parts of the mode shape separately simplifies the problem of computing sensitivity. In order to demonstrate our method, we study five periodic lattices (simple cubic (SC), body-centered cubic (BCC), face-centered cubic (FCC), octet, and hexagonal) that propagate pressure-like elastic waves at similar frequencies. We model these lattices using frame elements [53, 79]. We use our sensitivity analysis to optimize the group velocity for a chosen mode and at a chosen frequency for all five structures, as a function of their density and/or static stiffness. The structural parameters we choose to vary are the circular cross-sectional areas of the beams and the value of point masses located at the joints. We non-dimensionalise our analysis, so that the results can be applied to any frequency, by simply scaling a length parameter within each unit cell. In order to verify our results, we compare them to finite element simulations with 3-D elements in COMSOL, and validate them by comparing to experiments on 3-D printed samples. Our technique could also be applicable to other phenomena involving directional or preferential wave propagation, such as wave focusing or backscattering-free waveguiding.

Following this introduction, in Section 3.1.3, we report details on the formulation of group velocity culminating with its sensitivity analysis. In Section 3.1.4, we use our sensitivity analysis to calculate bounds on the wave speeds for the five considered lattices as a function of their densities and stiffness. Finally, in Section 3.1.5, we conduct experiments on two representative BCC lattices with engineered wave speeds and compare the results to our findings obtained from numerical calculations.

3.1.3 Optimal design of group velocity

Several important applications such as impedance matching structures, delay lines, frequency filters, and vibration absorbers require engineering wave speeds, i.e. group velocities, of specific modes at a frequency of propagation, or a range of frequencies. In this subsection, we define the group velocity of a wave propagating at a certain frequency in periodic media and we detail a framework to optimize the group velocity in a structure together with static properties such as the stiffness and mass density.

3.1.3.1 Background

Consider an infinite heterogeneous periodic medium, where the unit cell geometry is described by p parameters $\underset{\sim}{\chi} \in \mathbb{R}^p$. In this work, we consider a discrete system (either a discrete mass system or one obtained by the discretization of a continuum system as in Section 3.1.4.1) with d degrees of freedom $\underset{\sim}{U} \in \mathbb{R}^d$ in the reference unit cell. We index the unit cells with n-tuple of integers $\underset{\sim}{n} \in \mathbb{Z}^n$ depending on whether the unit cell is repeated in $n = 1, 2,$ or 3 dimensions. Let $u_{i\underset{\sim}{n}}$ denote the generalized displacement and $p_{i\underset{\sim}{n}} = \sum_{j,\underset{\sim}{m}} M_{i\underset{\sim}{n}j\underset{\sim}{m}} \dot{u}_{j\underset{\sim}{m}}$ denote the momentum associated with the i^{th} degree of freedom in the $\underset{\sim}{n}^{th}$ unit cell, and let $K_{i\underset{\sim}{n}j\underset{\sim}{m}}$ be the stiffness between the i^{th} degree of freedom in the $\underset{\sim}{n}^{th}$ unit cell and the j^{th} degree of freedom in the $\underset{\sim}{m}^{th}$ unit cell. Then the generalized equation of motion is

$$\sum_{j,\underset{\sim}{m}} M_{i\underset{\sim}{n}j\underset{\sim}{m}} \ddot{u}_{j\underset{\sim}{m}} = F_{i\underset{\sim}{n}} = \sum_{j,\underset{\sim}{m}} K_{i\underset{\sim}{n}j\underset{\sim}{m}} (u_{i\underset{\sim}{n}} - u_{j\underset{\sim}{m}}) \quad i = 1, \ldots d,\ \underset{\sim}{n} \in \mathbb{Z}^n. \tag{3.1}$$

The general solution to this equation may be written as a superposition of functions of the form $u_{i\underset{\sim}{n}}(t) = \exp(-i\omega t) U_{i\underset{\sim}{n}}$. Further, Bloch's theorem [16] enables us to write $U_{i\underset{\sim}{n}} = \exp(i\underset{\sim}{k} \cdot \underset{\sim}{n}) U_i$ where $\underset{\sim}{U} \in \mathbb{R}^d$ represents amplitude of displacements within a single unit cell. Thus, the general solution is a superposition of waves $u_{i\underset{\sim}{n}}(t) = \exp(i(\underset{\sim}{k} \cdot \underset{\sim}{n} - \omega t)) U_i$ with temporal frequency ω and wave vector $\underset{\sim}{k}$. Substituting this in eq. (3.1), we obtain the characteristic equation

$$\underset{\sim}{K}(\underset{\sim}{\chi}, \underset{\sim}{k}) \underset{\sim}{U} = \omega^2 \underset{\sim}{M}(\underset{\sim}{\chi}, \underset{\sim}{k}) \underset{\sim}{U}, \tag{3.2}$$

where $\underset{\sim}{K}$ and $\underset{\sim}{M}$ are the $d \times d$ self-adjoint stiffness and mass matrices with components

$$K_{ij}(\underset{\sim}{\chi}, \underset{\sim}{k}) = \sum_{\underset{\sim}{n}} \left(\exp(i\underset{\sim}{k} \cdot \underset{\sim}{n}) K_{i\underset{\sim}{0}j\underset{\sim}{n}}(\underset{\sim}{\chi}) - \sum_{l} \delta_{ij} K_{j\underset{\sim}{0}l\underset{\sim}{n}}(\underset{\sim}{\chi}) \right), \tag{3.3}$$

$$M_{ij}(\underset{\sim}{\chi}, \underset{\sim}{k}) = \sum_{\underset{\sim}{n}} \exp(i\underset{\sim}{k} \cdot \underset{\sim}{n}) M_{i\underset{\sim}{0}j\underset{\sim}{n}}(\underset{\sim}{\chi}). \tag{3.4}$$

Since $\underset{\sim}{n} \in \mathbb{Z}^n$ is an n-tuple of integers and $\underset{\sim}{k}$ occurs only in sinusoidal terms, it suffices to consider $\underset{\sim}{k}$ in the irreducible Brillouin zone ($\mathcal{B}$) which is the set $(0, \pi/L)^n$ for a cubic periodicity with

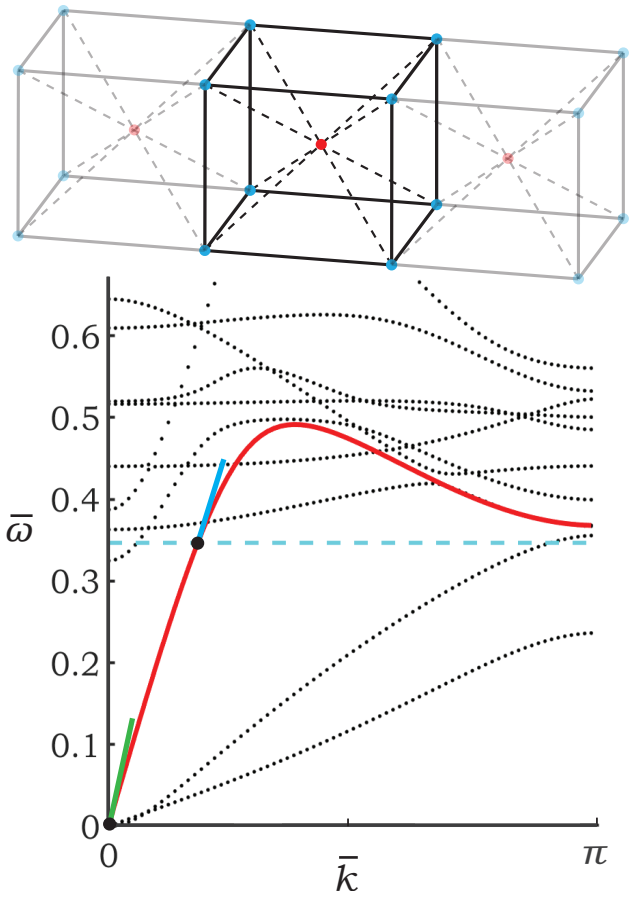

Figure 3.1: Dispersion plot: *Example of a body-centered cubic lattice and the corresponding dispersion relation between non-dimensional frequency and wavenumber.*

period L. Given any wave-vector $\underset{\sim}{k} \in \mathcal{B}$, eq. (4.1) is a generalized eigenvalue problem. Further since $\underset{\sim}{K}, \underset{\sim}{M}$ are self-adjoint and also positive definite for stable structures, there is a complete set of positive eigenvalues ω^2. It is customary to normalize the eigenmodes $\underset{\sim}{U} \cdot \underset{\sim}{M}\underset{\sim}{U} = 1$. Since $\underset{\sim}{K}, \underset{\sim}{M}$ depend smoothly on $\underset{\sim}{k}$, the resulting eigenvalues ω^2 and eigenvectors (eigenmodes) $\underset{\sim}{U}$ also depend smoothly on $\underset{\sim}{k}$. Thus, we obtain the *dispersion relation* with d branches $\omega^{(m)}(\underset{\sim}{k})$, $m = 1, \ldots, d$. A typical example – that of a body-centered cubic lattice that repeats in one dimension is shown in Fig. 3.1. The lattice displays point masses indicated by the red and blue dots at its joints. The plot shows the relation between non-dimensional frequency and non-dimensional wavenumber (magnitude of wave vector). We explain the non-dimensionalisation later in this section. The branch associated with the longitudinal mode where all deformations are parallel to the direction of periodicity indicated in red in Fig. 3.1.

In this work, we shall be concerned with wave packets consisting of waves with a particular mode with a narrow range of wave numbers and frequency. The energy of a wave packet associated with

the m^{th} mode propagates with the *group velocity*

$$\underset{\sim}{C}^{(m)} := \frac{\partial \omega^{(m)}}{\partial \underset{\sim}{k}} = \omega^{(m)}_{\underset{\sim}{k}}. \tag{3.5}$$

For future use, we note the relations

$$\underset{\sim}{C}^{(m)} = \frac{1}{2\omega^{(m)}} \underset{\sim}{U}^{(m)} . \left(\underset{\sim}{\underset{\sim}{K}}_{\underset{\sim}{k}} - (\omega^{(m)})^2 \underset{\sim}{\underset{\sim}{M}}_{\underset{\sim}{k}} \right) \underset{\sim}{U}^{(m)} \tag{3.6}$$

that follows from eq. (4.1) and the normalization of the eigenmode. In the above, subscript indicates partial derivative of a quantity. The wave speed is calculated as the magnitude of group velocity, $C^{(m)} = |\underset{\sim}{C}^{(m)}|$.

The static stiffness $E^{(m)}$ of the structure deformed in a particular mode is related to the speed of propagation of long wavelengths:

$$E^{(m)} = \frac{(C_0^{(m)})^2}{\rho}, \quad \text{where} \quad C_0^{(m)} = \lim_{\underset{\sim}{k} \to \underset{\sim}{0}} \; C^{(m)}(\underset{\sim}{k}) \tag{3.7}$$

and ρ is the average density of the unit cell. The long wavelength (or low frequency) wave speed and the finite wavelength (or moderate frequency) wave speed for the longitudinal mode in the illustrated BCC lattice are indicated by the slopes of the green and blue solid lines in Fig. 3.1, respectively.

Finally, we note that the dispersion relation may be such that there are no waves propagating at certain frequencies. We call the interval of frequencies for which there are no waves the *bandgap*.

3.1.3.2 Optimal design problem

We seek to design a structure, i.e., identify parameters $\underset{\sim}{\chi}$ in a design set $\mathcal{D}$, so that the structure has a given static stiffness E^*, a given density ρ^*, and a given wave speed C^* for a particular mode m of propagation with a given frequency ω^*.

The first step is to verify that there are indeed waves associated with mode m and the given frequency ω^*, i.e., we can find $\underset{\sim}{\chi}_0 \in \mathcal{D}$ and $\underset{\sim}{k}_0 \in \mathcal{B}$ such that $\omega^{(m)}(\underset{\sim}{\chi}_0, \underset{\sim}{k}_0) = \omega^*$. Suppose we can identify such a point, and further suppose that the group velocity at that point is non-zero, i.e., $C^{(m)}(\underset{\sim}{\chi}_0, \underset{\sim}{k}_0) \neq 0$, then we can use the implicit function theorem to identify a function $\underset{\sim}{k} = \underset{\sim}{k}^*(\underset{\sim}{\chi})$ such that

$$\omega^{(m)}(\underset{\sim}{\chi}, \underset{\sim}{k}^*(\underset{\sim}{\chi})) = \omega^* \tag{3.8}$$

in the neighborhood of $\underset{\sim}{\chi}_0, \underset{\sim}{k}_0$.

Second, we consider the density. The density $\rho(\underset{\sim}{\chi})$ is generally a monotone function of the parameters $\underset{\sim}{\chi}$, so it is generally possible to identify a set of admissible parameters which attain the given density:

$$\mathcal{D}_{\rho^*} = \{\underset{\sim}{\chi} \in \mathcal{D} : \rho(\underset{\sim}{\chi}) = \rho^*\}. \tag{3.9}$$

We assume that this is the case. If not, we can proceed by adding a constraint on our optimal design problem below.

The third step is to understand the range of wave speeds that can be attained by the admissible set of parameters. We do so by identifying the maximum and minimum wave speeds in terms of the optimal design problem

$$\max/\min_{\underset{\sim}{\chi}\in\mathcal{D}_{\rho^*}} \quad C^{(m)}\left(\underset{\sim}{\chi}, \underset{\sim}{k}^*(\underset{\sim}{\chi})\right). \tag{3.10}$$

We solve this problem using a descent method, but postpone the computation of the gradient till the next subsection.

We then turn to bounding the set of wave speeds and elastic moduli pairs that one can attain using the admissible set of parameters. We can obtain an outer bound on this set by studying the Pareto optimal of weighted averages. Given any $\gamma_1, \gamma_2 \in \mathbb{R}$, let

$$O(\gamma_1, \gamma_2) := \max_{\underset{\sim}{\chi}\in\mathcal{D}} \quad \gamma_1 C^{(m)}\left(\underset{\sim}{\chi}, \underset{\sim}{k}^*(\underset{\sim}{\chi})\right) + \gamma_2 E^{(m)}(\underset{\sim}{\chi}). \tag{3.11}$$

Then the convex hull of the set of all attainable wave speeds and stiffness is given by

$$\mathcal{S} = \{(C^{(m)}, E^{(m)}) : \gamma_1 C^{(m)} + \gamma_2 E^{(m)} \leq O(\gamma_1, \gamma_2), \gamma_1, \gamma_2 \in \mathbb{R}\}. \tag{3.12}$$

We again solve (3.11) using a descent method, but postpone the computation of the gradient till the next subsection. Figure 3.3(c) shows a typical result. We emphasize that this method only identifies the convex hull of the set: we do not know if the set is convex and therefore do not know how good an approximation the convex hull is to the actual set. However, extremal properties are of particular interest in the design and this method identifies these.

Finally, we address the full problem of identifying a structure that has a given static stiffness E^*, a given density ρ^*, and a given wave speed C^* for a particular mode m of propagation with a given frequency ω^*. We can again pose this as an optimal design problem: given $\delta_1, \delta_2 \geq 0$,

$$\min_{\underset{\sim}{\chi}\in\mathcal{D}_{\rho^*}} \left(\delta_1\left(C^{(m)}\left(\underset{\sim}{\chi}, \underset{\sim}{k}^*\left(\underset{\sim}{\chi}\right)\right) - C^*\right)^2 + \delta_2\left(E^{(m)}\left(\underset{\sim}{\chi}\right) - E^*\right)^2\right). \tag{3.13}$$

This objective is non-negative and equal to zero exactly when we find an optimal design. If the objective cannot be driven to zero, then we have a design that does not meet all the requirements. If this is the case, the ratio between δ_1 and δ_2 can be adjusted to find a design that matches the group velocity or the static stiffness. Again, we solve (3.13) using a descent method which requires the computation of the gradients as we presently describe.

3.1.3.3 Sensitivity analysis

We address the optimization problems (3.10), (3.11), and (3.13) using a descent method. We start by calculating the sensitivity of the group velocity to the design variables. Using the chain rule, we have

$$\frac{d}{d\underset{\sim}{\chi}_j}\underset{\sim}{C}^{(m)}\left(\underset{\sim}{\chi},\underset{\sim}{k}^*(\underset{\sim}{\chi})\right)=\frac{\partial\underset{\sim}{C}^{(m)}}{\partial\underset{\sim}{\chi}_j}\left(\underset{\sim}{\chi},\underset{\sim}{k}^*(\underset{\sim}{\chi})\right)+\sum_l\frac{\partial\underset{\sim}{C}^{(m)}}{\partial k_l}\left(\underset{\sim}{\chi},\underset{\sim}{k}^*(\underset{\sim}{\chi})\right)\times\frac{dk_l^*}{d\underset{\sim}{\chi}_j}\left(\underset{\sim}{\chi}\right) \tag{3.14}$$

recalling that $\underset{\sim}{k}^*$ is defined implicitly via the relation $\omega^{(m)}\left(\underset{\sim}{\chi},\underset{\sim}{k}^*(\underset{\sim}{\chi})\right)=\omega^*$. Let the direction of propagation of the wave be perpendicular to the plane containing unit vectors $\hat{\underset{\sim}{b}}$ and $\hat{\underset{\sim}{c}}$. We incorporate the constraints and calculate the sensitivities using the adjoint method, by modifying eq. (3.5) as

$$\underset{\sim}{C}^{(m)}\left(\underset{\sim}{\chi},\underset{\sim}{k}^*(\underset{\sim}{\chi})\right)=\frac{\partial\omega^{(m)}}{\partial\underset{\sim}{k}}\left(\underset{\sim}{\chi},\underset{\sim}{k}^*(\underset{\sim}{\chi})\right)+\underset{\sim}{\lambda}^{(1)}\left(\det\left(\underset{\sim}{K}\left(\underset{\sim}{\chi},\underset{\sim}{k}^*(\underset{\sim}{\chi})\right)-\omega^{*2}\underset{\sim}{M}\left(\underset{\sim}{\chi},\underset{\sim}{k}^*(\underset{\sim}{\chi})\right)\right)\right)+$$
$$\underset{\sim}{\lambda}^{(2)}\left(\underset{\sim}{k}^*(\underset{\sim}{\chi}).\hat{\underset{\sim}{b}}\right)+\underset{\sim}{\lambda}^{(3)}\left(\underset{\sim}{k}^*(\underset{\sim}{\chi}).\hat{\underset{\sim}{c}}\right), \tag{3.15}$$

where det(.) denotes the determinant of a matrix. Notice that $\det\left(\underset{\sim}{K}-\omega^{*2}\underset{\sim}{M}\right)=0$, when the relation $\omega^{(m)}=\omega^*$ is satisfied and $\underset{\sim}{k}^*.\hat{\underset{\sim}{b}}=\underset{\sim}{k}^*.\hat{\underset{\sim}{c}}=0$ when the wave vector is along $\hat{\underset{\sim}{k}}=\hat{\underset{\sim}{b}}\times\hat{\underset{\sim}{c}}$. This allows us to choose adjoint variables $\underset{\sim}{\lambda}^{(1)}$, $\underset{\sim}{\lambda}^{(2)}$, and $\underset{\sim}{\lambda}^{(3)}$ such that we avoid the computation of the derivative, $\frac{dk_l^*}{d\chi_j}$ in eq. (3.14). Substituting eq. (3.15) in eq. (3.14), we get

$$\frac{d\underset{\sim}{C}_i^{(m)}}{d\underset{\sim}{\chi}_j}=\frac{\partial^2\omega^{(m)}}{\partial k_i\partial\underset{\sim}{\chi}_j}+\lambda_i^{(1)}\mathrm{tr}\left(\mathrm{adj}\left(\underset{\sim}{K}-\omega^{*2}\underset{\sim}{M}\right)\left(\underset{\sim}{K}_{\underset{\sim}{\chi}_j}-\omega^{*2}\underset{\sim}{M}_{\underset{\sim}{\chi}_j}\right)\right)+$$
$$\sum_l\left(\frac{\partial^2\omega^{(m)}}{\partial k_i\partial k_l}+\lambda_i^{(1)}\mathrm{tr}\left(\mathrm{adj}\left(\underset{\sim}{K}-\omega^{*2}\underset{\sim}{M}\right)\left(\underset{\sim}{K}_{k_l}-\omega^{*2}\underset{\sim}{M}_{k_l}\right)\right)+2\lambda_i^{(2)}\sum_q\delta_{ql}\hat{b}_q+2\lambda_i^{(3)}\sum_q\delta_{ql}\hat{c}_q\right)\times\frac{dk_l^*}{d\underset{\sim}{\chi}_j}, \tag{3.16}$$

where tr(.) and adj(.) are the trace and adjoint of a matrix, respectively [110].

Let $\hat{a}_l=\mathrm{tr}\left(\mathrm{adj}\left(\underset{\sim}{K}-\omega^{*2}\underset{\sim}{M}\right)\left(\underset{\sim}{K}_{k_l}-\omega^{*2}\underset{\sim}{M}_{k_l}\right)\right)$. We pick $\underset{\sim}{\lambda}^{(1)}$, $\underset{\sim}{\lambda}^{(2)}$, and $\underset{\sim}{\lambda}^{(3)}$ such that

$\left(\frac{\partial^2\omega^{(m)}}{\partial^2\underset{\sim}{k}} + \underset{\sim}{\lambda}^{(1)} \otimes \hat{\underset{\sim}{a}} + 2\underset{\sim}{\lambda}^{(2)} \otimes \hat{\underset{\sim}{b}} + 2\underset{\sim}{\lambda}^{(3)} \otimes \hat{\underset{\sim}{c}}\right) = 0$. This gives us

$$\underset{\sim}{\lambda}^{(1)} = -\frac{\frac{\partial^2\omega^{(m)}}{\partial^2\underset{\sim}{k}}\hat{\underset{\sim}{k}}}{\hat{\underset{\sim}{a}}.\hat{\underset{\sim}{k}}}, \tag{3.17}$$

$$\underset{\sim}{\lambda}^{(2)} = -\frac{\frac{\partial^2\omega^{(m)}}{\partial^2\underset{\sim}{k}}\hat{\underset{\sim}{b}} + \underset{\sim}{\lambda}^{(1)}\left(\hat{\underset{\sim}{a}}.\hat{\underset{\sim}{b}}\right)}{2\hat{\underset{\sim}{b}}.\hat{\underset{\sim}{b}}},$$

$$\underset{\sim}{\lambda}^{(3)} = -\frac{\frac{\partial^2\omega^{(m)}}{\partial^2\underset{\sim}{k}}\hat{\underset{\sim}{c}} + \underset{\sim}{\lambda}^{(1)}\left(\hat{\underset{\sim}{a}}.\hat{\underset{\sim}{c}}\right)}{2\hat{\underset{\sim}{c}}.\hat{\underset{\sim}{c}}}.$$

Substituting eq. (3.17) into eq. (3.16) gives us

$$\frac{d\underset{\sim}{C}_i^{(m)}}{d\chi_j} = \frac{\partial^2\omega^{(m)}}{\partial k_i \partial\chi_j} - \frac{\sum_l \frac{\partial^2\omega^{(m)}}{\partial k_i \partial k_l}\hat{k}_l}{\hat{\underset{\sim}{a}}.\hat{\underset{\sim}{k}}}\mathrm{tr}\left(\mathrm{adj}\left(\underset{\sim}{K} - \omega^{*2}\underset{\sim}{M}\right)\left(\underset{\sim}{K}_{\chi_j} - \omega^{*2}\underset{\sim}{M}_{\chi_j}\right)\right). \tag{3.18}$$

Let $\alpha = \chi_j$ or k_l. Then, $\frac{\partial^2\omega^{(m)}}{\partial k_i \partial\alpha}$ can be calculated by differentiating eq. (3.6) as

$$\frac{\partial^2\omega^{(m)}}{\partial k_i\partial\alpha} = \frac{1}{2\omega^{(m)}}\Bigg(2\,\mathrm{Re}\left(\underset{\sim}{U}_\alpha^{(m)}.\left(\underset{\sim}{K}_{k_i} - \left(\omega^{(m)}\right)^2\underset{\sim}{M}_{k_i}\right)\underset{\sim}{U}^{(m)}\right) +$$
$$\underset{\sim}{U}^{(m)}.\left(\underset{\sim}{K}_{k_i\alpha} - \left(\omega^{(m)}\right)^2\underset{\sim}{M}_{k_i\alpha} - 2\omega^{(m)}\omega_\alpha^{(m)}\underset{\sim}{M}_{k_i}\right)\underset{\sim}{U}^{(m)} - \frac{\omega_\alpha^{(m)}}{\omega^{(m)}}\underset{\sim}{U}^{(m)}.\left(\underset{\sim}{K}_{k_i} - \left(\omega^{(m)}\right)^2\underset{\sim}{M}_{k_i}\right)\underset{\sim}{U}^{(m)}\Bigg), \tag{3.19}$$

where Re(.) is the real part of a complex entity.

Evaluating eq. (3.19) poses a challenge, as the sensitivity of the eigenvector with respect to the topology and wavenumber, $\underset{\sim}{U}_\alpha^{(m)}$, is not trivial to calculate. This is because the explicit expression of the mode shape $\underset{\sim}{U}^{(m)}$ in terms of χ_j and k_l is often difficult to compute.

We now present a method to calculate the sensitivities $\underset{\sim}{U}_\alpha^{(m)}$, which can be used to compute the sensitivities of dispersion properties that depend on the eigenvector $\underset{\sim}{U}^{(m)}$. By analyzing the real and imaginary parts of eq. (4.1) separately, we arrive at the equations

$$\underset{\sim}{A}^R\underset{\sim}{U}^{(m)^R} - \underset{\sim}{A}^I\underset{\sim}{U}^{(m)^I} = 0, \tag{3.20}$$

$$\underset{\sim}{A}^I\underset{\sim}{U}^{(m)^R} + \underset{\sim}{A}^R\underset{\sim}{U}^{(m)^I} = 0, \tag{3.21}$$

where $\underset{\sim}{A} = \underset{\sim}{K} - \left(\omega^{(m)}\right)^2\underset{\sim}{M}$ and the superscripts R and I denote the real and imaginary parts of the complex entity. The mass orthogonality constraint $\underset{\sim}{U}^{(m)}.\underset{\sim}{M}\underset{\sim}{U}^{(m)} = 1$ can be written as

$$\left(\underset{\sim}{U}^{(m)^R} - i\underset{\sim}{U}^{(m)^I}\right).\left(\left(\underset{\sim}{M}^R\underset{\sim}{U}^{(m)^R} - \underset{\sim}{M}^I\underset{\sim}{U}^{(m)^I}\right) + i\left(\underset{\sim}{M}^I\underset{\sim}{U}^{(m)^R} + \underset{\sim}{M}^R\underset{\sim}{U}^{(m)^I}\right)\right) = 1. \tag{3.22}$$

Differentiating equations (3.20) to (3.22) with respect to α yields

$$\underset{\sim}{A}^R \underset{\sim}{U}_\alpha^{(m)R} - \underset{\sim}{A}^I \underset{\sim}{U}_\alpha^{(m)I} = \underset{\sim}{A}_\alpha^I \underset{\sim}{U}^{(m)I} - \underset{\sim}{A}_\alpha^R \underset{\sim}{U}^{(m)R} =: b_1, \tag{3.23}$$

$$\underset{\sim}{A}^R \underset{\sim}{U}_\alpha^{(m)I} + \underset{\sim}{A}^I \underset{\sim}{U}_\alpha^{(m)R} = -\underset{\sim}{A}_\alpha^I \underset{\sim}{U}^{(m)R} - \underset{\sim}{A}_\alpha^R \underset{\sim}{U}^{(m)I} =: b_2, \tag{3.24}$$

$$\underset{\sim}{U}_\alpha^{(m)R}.\left(\underset{\sim}{M}^R \underset{\sim}{U}^{(m)R}\right) + \underset{\sim}{U}_\alpha^{(m)I}.\left(\underset{\sim}{M}^R \underset{\sim}{U}^{(m)I}\right) = -\frac{1}{2}\left(\underset{\sim}{U}^{(m)R}.\underset{\sim}{M}_\alpha^R \underset{\sim}{U}^{(m)R} + \underset{\sim}{U}^{(m)I}.\underset{\sim}{M}_\alpha^R \underset{\sim}{U}^{(m)I}\right) =: c_1, \tag{3.25}$$

$$\underset{\sim}{U}_\alpha^{(m)R}.\left(\underset{\sim}{M}^I \underset{\sim}{U}^{(m)R}\right) + \underset{\sim}{U}_\alpha^{(m)I}.\left(\underset{\sim}{M}^I \underset{\sim}{U}^{(m)I}\right) = -\frac{1}{2}\left(\underset{\sim}{U}^{(m)R}.\underset{\sim}{M}_\alpha^I \underset{\sim}{U}^{(m)R} + \underset{\sim}{U}^{(m)I}.\underset{\sim}{M}_\alpha^I \underset{\sim}{U}^{(m)I}\right) =: c_2. \tag{3.26}$$

We notice that equations (3.20) to (3.24) together with the sum of equations (3.25) and (3.26) can be combined using a block matrix representation as

$$\begin{pmatrix} 0 & \left(\left(\underset{\sim}{M}^R + \underset{\sim}{M}^I\right)\underset{\sim}{U}^{(m)R}\right)^T & \left(\left(\underset{\sim}{M}^R + \underset{\sim}{M}^I\right)\underset{\sim}{U}^{(m)I}\right)^T \\ -b_1 & \underset{\sim}{A}^R & -\underset{\sim}{A}^I \\ -b_2 & \underset{\sim}{A}^I & \underset{\sim}{A}^R \end{pmatrix} \begin{pmatrix} 1 \\ \underset{\sim}{U}_\alpha^{(m)R} - (c_1+c_2)\underset{\sim}{U}^{(m)R} \\ \underset{\sim}{U}_\alpha^{(m)I} - (c_1+c_2)\underset{\sim}{U}^{(m)I} \end{pmatrix} = \begin{pmatrix} 0 \\ 0 \\ 0 \end{pmatrix}. \tag{3.27}$$

Superscript T denotes transpose of a matrix. Now, set

$$D_1 = \begin{pmatrix} 0 & \left(\left(\underset{\sim}{M}^R + \underset{\sim}{M}^I\right)\underset{\sim}{U}^{(m)R}\right)^T & \left(\left(\underset{\sim}{M}^R + \underset{\sim}{M}^I\right)\underset{\sim}{U}^{(m)I}\right)^T \\ -b_1 & \underset{\sim}{A}^R & -\underset{\sim}{A}^I \\ -b_2 & \underset{\sim}{A}^I & \underset{\sim}{A}^R \end{pmatrix},\ D_2 = \begin{pmatrix} \underset{\sim}{A}^R & -\underset{\sim}{A}^I \\ \underset{\sim}{A}^I & \underset{\sim}{A}^R \end{pmatrix},$$

$$D_3 = \begin{pmatrix} 0 & 0 & 0 \\ 0 & \underset{\sim}{A}^R & -\underset{\sim}{A}^I \\ 0 & \underset{\sim}{A}^I & \underset{\sim}{A}^R \end{pmatrix},\ D_4 = \begin{pmatrix} 0 & \left(\left(\underset{\sim}{M}^R + \underset{\sim}{M}^I\right)\underset{\sim}{U}^{(m)R}\right)^T & \left(\left(\underset{\sim}{M}^R + \underset{\sim}{M}^I\right)\underset{\sim}{U}^{(m)I}\right)^T \\ -b_1 & 0 & 0 \\ -b_2 & 0 & 0 \end{pmatrix}. \tag{3.28}$$

Let the size of matrix D_1 be $n \times n$. We have that $\text{rank}(D_2)$ is $n-2$, assuming single multiplicity of the eigenvalue at the fixed frequency ω^* for a chosen mode in eq. (4.1). As D_2 is a submatrix of D_1, $\text{rank}(D_1) \geq n-2$. From the previous argument, it is straightforward to show that $\text{rank}(D_3) = n-3$, and we also see that D_4 is a matrix of rank at most equal to one. Since D_1 is the sum of matrices D_3 and D_4, we have that $\text{rank}(D_1) \leq n-2$. Hence, we conclude that the nullity of matrix D_1 is two. Let the elements of this null space be represented by $\underset{\sim}{y}_1$ and $\underset{\sim}{y}_2$. Then, eq. (3.27) gives us

$$\begin{pmatrix} 0 \\ \underset{\sim}{U}_\alpha^{(m)^R} \\ \underset{\sim}{U}_\alpha^{(m)^I} \end{pmatrix} = \beta_1 \underset{\sim}{y}_1 + \beta_2 \underset{\sim}{y}_2 - \begin{pmatrix} 1 \\ -(c_1 + c_2)\underset{\sim}{U}^{(m)^R} \\ -(c_1 + c_2)\underset{\sim}{U}^{(m)^I} \end{pmatrix}. \tag{3.29}$$

Finally, the sensitivities $\underset{\sim}{U}_\alpha^{(m)}$ can be computed as $\underset{\sim}{U}_\alpha^{(m)} = \underset{\sim}{U}_\alpha^{(m)^R} + i\underset{\sim}{U}_\alpha^{(m)^I}$. The scalars β_1 and β_2 can be calculated from the equality that the first element of the vector $\beta_1 \underset{\sim}{y}_1 + \beta_2 \underset{\sim}{y}_2$ is 1, together with one of equations (3.25) or (3.26). For cases where the multiplicity of the eigenvalue ω^* is more than one, we have multiple eigenvectors satisfying the eigenvalue problem given by eq. (4.1) and as a result end up with more than two vectors in the null space from eq. (3.27). This requires additional information on the sensitivities of the desired mode shape. Such situations seldom happen and we stick to geometries and modes where the eigenvalue from eq. (4.1) has single multiplicity, in this section.

Plugging the sensitivities $\underset{\sim}{U}_\alpha^{(m)}$ into eq. (3.19) and subsequently into eq. (3.18) gives us the sensitivities of the group velocity with respect to the topological parameters. The sensitivities of the objectives in problems (3.10), (3.11), and (3.13) can be expressed in terms of the sensitivity of the group velocity, to solve them using a descent method. In the rest of the section, we look at waves propagating along one of the orthogonal axes, which is the direction of periodicity of a lattice i.e. $\hat{\underset{\sim}{k}} = (1, 0, 0)^T, \hat{\underset{\sim}{b}} = (0, 1, 0)^T, \hat{\underset{\sim}{c}} = (0, 0, 1)^T$, in which case we notice that $\hat{\underset{\sim}{a}}$ is parallel to $\hat{\underset{\sim}{k}}$. As we study waves propagating in this fixed direction, any function of the wave vector can be thought of as a function of wavenumber in that direction. We refer to the component of the group velocity vector from eq. (3.5) along the direction of propagation as the group velocity or wave speed.

3.1.4 Lattices

In this subsection, we solve the optimal design problems using the sensitivity analysis explained in the previous subsection to study five periodic lattice structures with masses at joints as shown in Fig. 3.2(a)-(e). However, the methods developed in this section are general and can be used on structures with arbitrary directions of periodicity and arbitrarily chosen frequencies of propagation.

We repeat each unit cell along one direction indicated by the arrow in Fig. 3.2(a)-(e), with a lattice parameter equal to the length of the unit cell in that direction, as to generate one dimensional arrays of cells. For these one dimensional arrays, we consider longitudinal waves propagating at a fixed frequency along the direction indicated by the arrow, and solve the optimal design problems from section 3.1.3.2. The topological parameters varied are the circular cross-sectional areas of the bars together with point masses at each node, while still maintaining symmetry of the structures. In

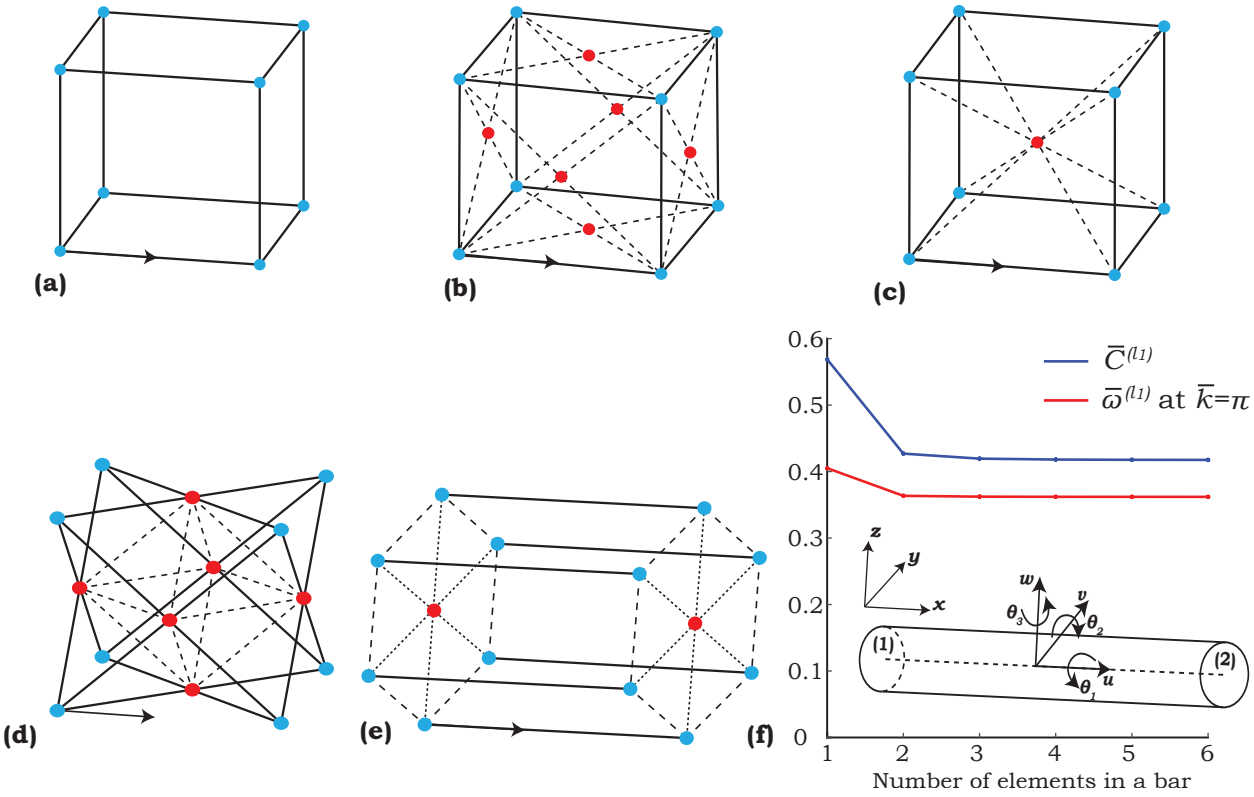

Figure 3.2: Lattices: ***(a)-(e)*** *Unit cells from the SC, FCC, BCC, octet and hexagonal lattices, respectively, where the lines are links, the colored dots are concentrated, point masses and the arrows indicate the direction of wave propagation.* ***(f)*** *Convergence study of wave speed and frequency of the first longitudinal mode with number of frame elements in a bar for a BCC lattice. Inset shows a frame element with two nodes and six degrees of freedom at each node.*

each unit cell, bars indicated by the same stroke (solid, dashed, or dotted) are constrained to have identical cross-sectional areas. Similarly, the points at the corner nodes (shown in blue) have the same mass in each unit cell and all the points marked in red have the same mass.

3.1.4.1 Frame elements

We discretize each bar in a lattice connecting two point masses into multiple frame elements. A frame element can deform along its axis as well as along the directions perpendicular to its axis. Each element can carry axial and shear loads, and bending and torsional moments. Hence, each point on the element has six degrees of freedom– three translational displacements (u, v, and w) and three rotational (θ_1, θ_2, and θ_3) as shown in Fig. 3.2(f). Assuming small deformations, these

displacements and angles can be calculated as

$$
\begin{aligned}
u &= N_1 u^{(1)} + N_2 u^{(2)}, \\
v &= N_3 v^{(1)} + N_4 \theta_3^{(1)} + N_5 v^{(2)} + N_6 \theta_3^{(2)}, \\
w &= N_3 w^{(1)} + N_4 \theta_2^{(1)} + N_5 w^{(2)} + N_6 \theta_2^{(2)}, \\
\theta_1 &= N_1 \theta_1^{(1)} + N_2 \theta_1^{(2)}, \\
\theta_2 &= \frac{\partial w}{\partial x}, \\
\theta_3 &= \frac{\partial v}{\partial x}
\end{aligned}
\tag{3.30}
$$

where the degrees of freedom $u^{(1)},\ v^{(1)},\ w^{(1)},\ \theta_1^{(1)},\ \theta_2^{(1)}$, and $\theta_3^{(1)}$ (three translational (displacement) degrees of freedom and three rotational (angular) degrees of freedom) correspond to one end of a frame element (labeled (1) in Fig. 3.2(f)). The degrees of freedom $u^{(2)},\ v^{(2)},\ w^{(2)},\ \theta_1^{(2)},\ \theta_2^{(2)}$, and $\theta_3^{(2)}$ are the corresponding degrees of freedom associated with the other end (labeled (2)) of the frame element. The shape functions $N_i,\ i = 1, \ldots, 6$ can be calculated from the boundary conditions as [53, 79]

$$
\begin{aligned}
N_1 &= \frac{1-\xi}{2}, \\
N_2 &= \frac{1+\xi}{2}, \\
N_3 &= \frac{2-3\xi+\xi^3}{4}, \\
N_4 &= \frac{a(1-\xi-\xi^2+\xi^3)}{4}, \\
N_5 &= \frac{2+3\xi-\xi^3}{4}, \\
N_6 &= \frac{a(-1-\xi+\xi^2+\xi^3)}{4},
\end{aligned}
\tag{3.31}
$$

where $a = L_{el}/2$, with L_{el} the length of the element, and $\xi = x/a$, with $-a \leq x \leq a$ and $x = 0$ and the center of the element.

From this point onward, we non-dimensionalize our analysis so that the designs derived in the following subsections can be scaled to any frequency of operation with just a length parameter of the lattice. Let L be the length of a unit cell along the direction of periodicity, ρ_s be the density of the solid material, and E_s be the Young's modulus of elasticity of the solid material. Then, every length, mass, and time dimension is non-dimensionalized by dividing them with L, $\rho_s L^3$, and $\sqrt{\frac{\rho_s}{E_s}}L$, respectively.

We non-dimensionalze the elemental stiffness and mass matrices for frame elements from ref. [53, 79] as detailed in Methods A. Assembling them for a wave propagating through the structure, while invoking Bloch's theorem, gives us the non-dimensional version of eq. (4.1)

$$\overline{\underset{\sim}{K}}\left(\overline{\underset{\sim}{\chi}},\overline{\underset{\sim}{k}}\right)\overline{\underset{\sim}{U}}\left(\overline{\underset{\sim}{\chi}},\overline{\underset{\sim}{k}}\right)=\overline{\omega}\left(\overline{\underset{\sim}{\chi}},\overline{\underset{\sim}{k}}\right)^{2}\ \overline{\underset{\sim}{M}}\left(\overline{\underset{\sim}{\chi}},\overline{\underset{\sim}{k}}\right)\overline{\underset{\sim}{U}}\left(\overline{\underset{\sim}{\chi}},\overline{\underset{\sim}{k}}\right), \tag{3.32}$$

where $\overline{\underset{\sim}{K}}$ and $\overline{\underset{\sim}{M}}$ are the non-dimensional self-adjoint global stiffness and mass matrices, and $\overline{\underset{\sim}{U}}$ is the non-dimensional global displacement vector. $\overline{\omega}$ and $\overline{\underset{\sim}{k}}$ represent the non-dimensional frequency and wave vector of propagation. The vector $\overline{\underset{\sim}{\chi}}$ represents the topology of a unit cell and comprises the non-dimensional cross sectional areas of bars (cross-sectional area divided by L^2) and the non-dimensional masses at the joints (mass divided by $\rho_s L^3$). Note that for a given frequency of wave propagation ω^* (in rad/s), the corresponding non-dimensional frequency $\overline{\omega}^*$ (in rad) can be calculated as $\omega^*\sqrt{\frac{\rho_s}{E_s}}L$. Hence, the optimal topology obtained from optimizing the wave speed at one particular frequency can be scaled by a function of the length of the unit cell L, in order to obtain the topology that optimizes the wave speed at any chosen frequency.

We perform a convergence study to test the effect of number of elements considered in a bar on dispersion properties, as shown in Fig. 3.2(f). As an example, we consider a BCC lattice without any point masses at the joints, and edge bars (solid in Fig. 3.2(c)) four times in the cross-sectional area compared to the diagonal bars (dotted). We first measure the non-dimensional wave speed of the first longitudinal mode at a non-dimensional frequency $\overline{\omega}^* = 0.35$ (illustrated by the slope of the blue solid line in Fig. 3.1). Second, we measure the non-dimensional frequency of the mode (red curve in Fig. 3.1) at a high non-dimensional wavenumber $\overline{k} = |\overline{\underset{\sim}{k}}| = \pi$, which tends to be sensitive to the number of elements considered. The change in wave speed is 1.70% and in frequency at $\overline{k} = \pi$ is 0.33%, on increasing the number of elements in a bar from two to three. As a result of this negligible increase, we consider in the rest of this section two elements in each bar.

In the following subsection, we calculate bounds on the non-dimensional group velocity of an n^{th} longitudinal mode, $\overline{C}^{(l_n)}$ as a function of non-dimensional density and longitudinal static stiffness of each 1-D periodic lattice, for a non-dimensional frequency of propagation $\overline{\omega}^* = 0.35$. To compute these bounds, we solve the problems formulated in section 3.1.3.2, which are non-dimensionalized as described earlier in this subsection.

3.1.4.2 Bounds on group velocity

For waves propagating along the directions indicated by the arrows in Fig. 3.2(a)-(e), the non-dimensional wavenumber $\overline{k}$ (in rad) ranges from 0 to π on $\mathcal{B}$. This zone corresponds to the path that the wave vectors are restricted to in section 3.1.3. We can calculate the non-dimensional

Table 3.1: Material properties and bounds on topological variables

Parameter	E_s	ρ_s	G_s	$\overline{A}_{min}$	$\overline{A}_{max}$	$\overline{m}_{min}$	$\overline{m}_{max}$
Value	1.7 GPa	930 kg/m^3	0.63 GPa	4.25×10^{-3}	17×10^{-3}	0	34×10^{-3}

frequency $\overline{\omega}$ associated with each $\overline{k}$ for a fixed topology of a unit cell, to obtain its band structure. An example of this dispersion relation is shown in Fig. 3.1, for a BCC lattice. Each frequency of propagation excites multiple modes within the lattice, highlighting the modal richness typical of lattice structures. The mode highlighted in red indicates the first longitudinal mode of the structure, i.e. the frequencies of this mode at any wavenumber correspond to $\overline{\omega}^{(l_1)}$. This longitudinal mode is the combination of a mode that involves displacements only along the direction of propagation of the wave and a flexural mode that involves bending of the beams along this direction. We obtain this longitudinal mode by isolating its frequency of propagation from the other modes. The algorithm used to obtain the frequency of propagation $\overline{\omega}^{(l_n)}$ of the n^{th} longitudinal mode at any given wavenumber $\overline{k}$ is discussed in Algorithm 7 of Methods B.

First, we calculate bounds on the non-dimensional group velocity as a function of density for each of the five lattices repeating in one direction as shown in Fig. 3.2 at $\overline{\omega}^* = 0.35$, by solving problem (3.10). To avoid bandgaps for the most part within the bounds of choice for the chosen frequency $\overline{\omega}^*$, we optimize the wave speed of the first longitudinal mode of the SC, BCC, hexagonal and octet lattices. For the FCC lattice, we pick the third longitudinal mode. In the rest of this section, we assign material properties of the solid material (Table 3.1) making the lattice to be that of EOS polyamide PA 2200 [1, 96], which we also use for our experimental validation. G_s is the shear modulus of rigidity of the material. We set constraints on the topology of each lattice (domain $\mathcal{D}$ in section 3.1.3.2), by choosing bounds on the non-dimensional cross-sectional areas of the bars and on the added masses, concentrated at the joints. These bounds can be chosen based on the manufacturing tolerances for specific applications. In our analysis, the minimum and maximum non-dimensional areas of a bar are chosen to be $\overline{A}_{min}$ and $\overline{A}_{max}$, respectively, indicated in Table 3.1. We pick these bounds so that the beams are slender enough to be modeled by our numerical method, while still ensuring their structural integrity to repeatedly test the 3-D printed samples. The maximum mass ($\overline{m}_{max}$) at a joint is considered to be twice as heavy as the thickest possible beam with a length equal to the lattice parameter and the minimum mass ($\overline{m}_{min}$) is taken to be zero. We can represent these bounds on the topology vector $\underset{\sim}{\overline{\chi}}$ by non-dimensional lower and upper bound vectors $\underset{\sim}{B}_l$ and $\underset{\sim}{B}_u$, respectively. As the topology of each unit cell is described by a vector of cross-sectional areas and masses, it is easy to calculate the non-dimensional density of a lattice from a linear equation of the form $f\left(\underset{\sim}{\overline{\chi}}\right) = \underset{\sim}{A}_{eq}.\underset{\sim}{\overline{\chi}} = \overline{\rho}$. We solve the optimization problems with MATLAB's gradient based solver *fmincon*, which also allows for linear equality and inequality

constraints.

To determine an initial guess for topology and wavenumber and to ensure we start with a geometry that has wave propagation at $\overline{\omega}^*$, we solve the problem,

$$\begin{aligned} \underset{\underset{\sim}{\overline{\chi}},\, \overline{k}}{\arg\min} \quad & \left(\overline{\omega}^* - \overline{\omega}^{(l_n)}\left(\underset{\sim}{\overline{\chi}}, \overline{k}\right)\right)^2 \\ \text{subject to} \quad & 0 \leq \overline{k} \leq \pi \\ & \underset{\sim}{B}_l \leq \underset{\sim}{\overline{\chi}} \leq \underset{\sim}{B}_u \\ & \underset{\sim}{A}_{eq} . \underset{\sim}{\overline{\chi}} = \overline{\rho}, \end{aligned} \tag{3.33}$$

using Algorithm 7 together with sensitivities derived in section 3.1.3.3, using a gradient based optimization method. Given a topology of a structure $\underset{\sim}{\overline{\chi}}_0$ with wave propagation of the desired longitudinal mode at $\overline{\omega}^*$, the corresponding wavenumber of propagation $\overline{k}_0\left(\underset{\sim}{\overline{\chi}}_0\right)$ can be calculated by solving

$$\begin{aligned} \underset{\overline{k}}{\arg\min} \quad & \left(\overline{\omega}^* - \overline{\omega}^{(l_n)}\left(\underset{\sim}{\overline{\chi}}_0, \overline{k}\right)\right)^2 \\ \text{subject to} \quad & 0 \leq \overline{k} \leq \pi. \end{aligned} \tag{3.34}$$

We now solve problem (3.10) to calculate bounds on the non-dimensional group velocity at a given non-dimensional density as follows. Starting from the initial guess for topology from problem (3.33), the gradient of the wave speed with respect to the unit cell topology from section 3.1.3.3 is used to increment the topology vector along the direction of steepest descent/ ascent (for minimization/ maximization). After this increment, the new wavenumber corresponding to the updated topology $\overline{k}\left(\underset{\sim}{\overline{\chi}}\right)$ at frequency $\overline{\omega}^*$ is calculated by solving problem (3.34). These increments are made until we converge to an optimum around the initial guess. Owing to the non-linearity of the problem, the topologies corresponding to the optimal values need not be unique.

For some geometries, we notice that more than one wavenumber can coexist at a given frequency for a selected mode, due to the fact that dispersion branches need not be monotonic. For example, this is the case for the highlighted longitudinal mode in Fig. 3.1. In such cases, we optimize the wave speed at the lower wavenumber. As a last note on the optimization problem, we fix the length of the diagonal bars in the hexagonal lattice as half the length of the unit cell along the direction of periodicity, so that we maintain the linear form of the function describing its density in terms of $\underset{\sim}{\overline{\chi}}$.

An example showing the construction of bounds is shown in Fig. 3.3(a) for the BCC lattice, where we calculate the maximum and minimum group velocities at fixed densities for the range of possible densities. Notice that a minimum wave speed of zero is achieved for a broad range of densities for the chosen longitudinal mode. This indicates that we either find topologies that force $\overline{\omega}^*$ to

a band edge or that we observe a standing wave. We pick two topologies of the BCC lattice to experimentally validate our results, one with the fastest propagating wave speed $\left(\overline{C}^{(l_1)} = 0.43\right)$ and the other with an arbitrarily chosen low speed $\left(\overline{C}^{(l_1)} = 0.1\right)$ within the bounds of wave speed, and roughly the same density. The properties of these structures are indicated by dashed lines and start markers in Fig. 3.3(a) and the topologies are calculated by solving problem (3.13). We are limited by the manufacturability of point masses at the nodes, which causes the slight variation in density between the two chosen geometries. In the lattice with the intermediate wave speed, the bars along the diagonal of a unit cell are the thickest ($\overline{A} = 17 \times 10^{-3}$) and the bars along the wave propagation vector are the thinnest ($\overline{A} = 4.25 \times 10^{-3}$), with point masses at the corners with non-dimensional mass $\overline{m} = 5.8 \times 10^{-3}$. In the lattice with the faster wave speed, the bars along the diagonal have the least cross-sectional areas ($\overline{A} = 4.25 \times 10^{-3}$) and the bars along the lattice vector have the highest areas ($\overline{A} = 17 \times 10^{-3}$) without any point masses at the joints.

Fig. 3.3(b) shows the results of the optimization for the five one-dimensional periodic lattices of choice at $\overline{\omega}^* = 0.35$, in terms of achievable regions of the wave speed vs. density space. The hexagonal lattice features the highest wave speeds at low relative densities. This can be attributed to its high static stiffness in the longitudinal direction provided by the six bars aligned along this direction (see Fig. 3.2(e)). Intuitively, placing the thickest bars along the propagation direction in all geometries boosts the long wavelength wave speed at a given density. The SC lattice is the least dense, while still featuring high wave speeds. FCC and BCC lattices allow to span wider density ranges, while presenting similar wave speeds. Finally, the octet lattice presents the lowest maximum wave speeds, owing to the absence of bars aligned in the direction of wave propagation.

Next, we calculate bounds on the non-dimensional group velocity vs. static stiffness for the five lattices, at $\overline{\omega}^* = 0.35$. We maintain the same constraints on the topology of each unit cell as indicated in Table 3.1. Once again, to avoid bandgaps for the most part within the topological bounds for $\overline{\omega}^* = 0.35$, we optimize the group velocity $\overline{C}^{(l_n)}$ of the first longitudinal mode for the SC, BCC, hexagonal, and octet lattices, and the third longitudinal mode for the FCC lattice. To calculate the bounds, we solve problem (3.11) using a gradient based method with the sensitivities derived in section 3.1.3.3. An example showing the construction of bounds is shown in Fig. 3.3(c) for the BCC lattice. Here $\overline{E}^{(l_n)}\left(\underset{\sim}{\overline{\chi}}\right) = E^{(l_n)}\left(\underset{\sim}{\chi}\right)/E_s$. The shaded region contains all the attainable values of group velocity and stiffness. Also, the properties at the corners of the shaded region where three or more hyperplanes are concurrent are always achieved. We repeat the process for all five lattices to calculate the bounds as shown in Fig. 3.3(d). We can achieve a large range of possible wave speeds at fixed stiffness values, even though the two properties are highly dependent and proportional. We are able to decouple these properties because of the presence of point masses, which allow us to vary the dispersion properties such as wave speed, without affecting the static

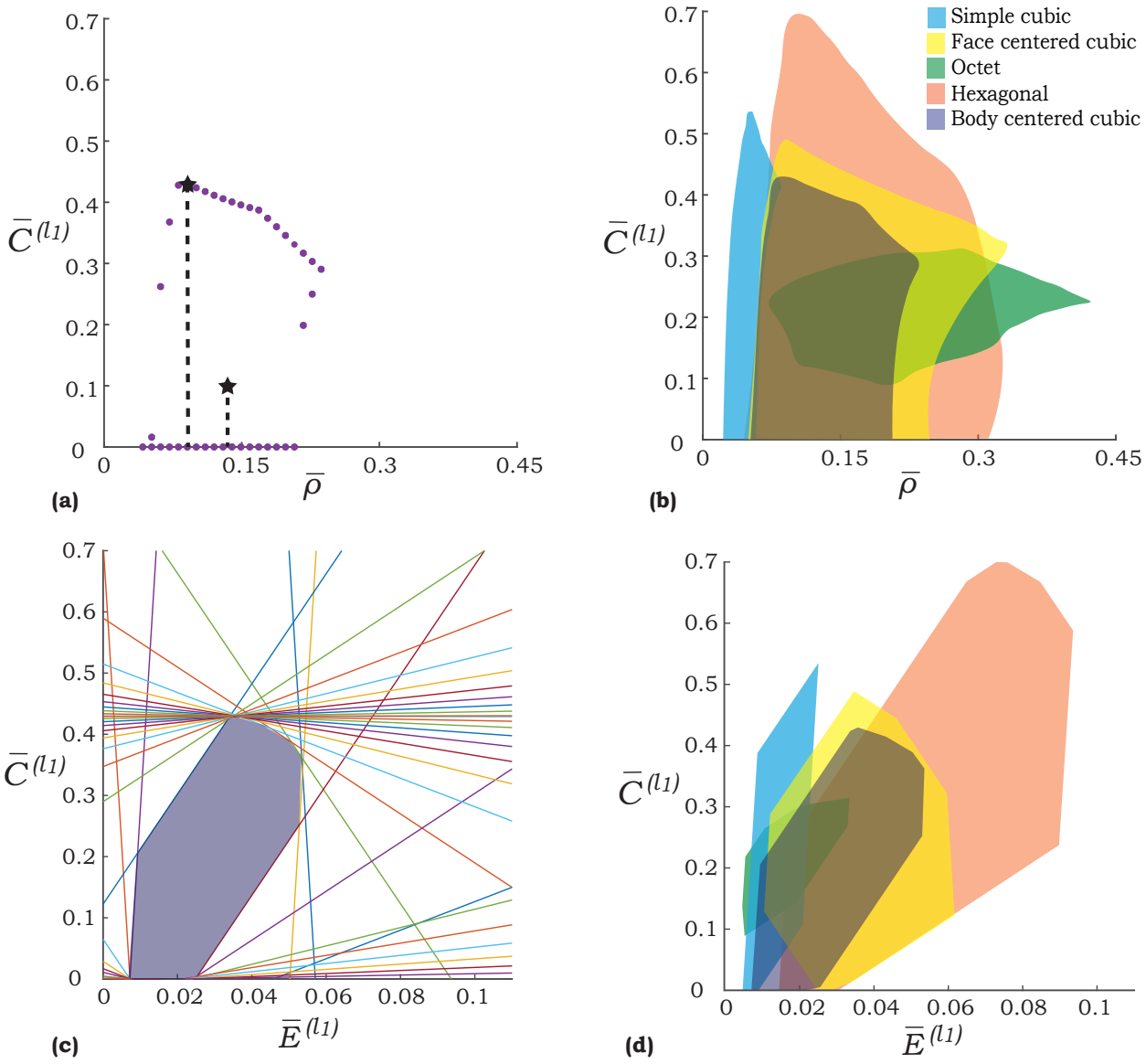

Figure 3.3: Bounds on properties: ***(a)*** *Construction of bounds on non-dimensional group velocity vs. non-dimensional density for the BCC lattice at* $\overline{\omega}^* = 0.35$. ***(b)*** *Bounds on the non-dimensional group velocity of the chosen longitudinal mode with respect to the non-dimensional density of each lattice.* ***(c)*** *Construction of bounds on non-dimensional group velocity vs. non-dimensional static stiffness for the BCC lattice at* $\overline{\omega}^* = 0.35$. ***(d)*** *Bounds on the non-dimensional group velocity of the chosen longitudinal mode with respect to the non-dimensional stiffness of each lattice.*

stiffness.

3.1.4.3 Verification with 3-D finite element solver

We obtain the optimal designs and bounds in section 3.1.4.2 by modeling the bars in each structure using frame elements, which assumes slender bars represented by one dimensional elements. In this subsection, we compare the group velocities and mode shapes of key optimal designs modeled using 3-D solid elements (tetrahedral elements) in COMSOL. Specifically, we compare the wave speeds and mode shapes of topologies that attain peak group velocity in Fig. 3.3(b) and (d) as these designs are achieved at extremal values of $\overline{\underset{\sim}{\chi}}$. To visualize the cell deformation that is characteristic of the longitudinal modes, we plot mode shapes for each of the five lattices in Fig. 3.4(a) and (b) obtained by modeling the structures using frame elements and 3-D solid elements, respectively, at extreme wavenumbers. Fig. 3.4(c) depicts the dispersion curves for the longitudinal modes considered in these lattices modeled using frame elements. Note that the dashed line indicates the frequency of interest, $\overline{\omega}^* = 0.35$.

In order to understand the mode shape of each mode depicted in Fig. 3.4(c), we evaluate the mode shape, i.e. the mass normalized eigenvector from eq. (3.32) at a given wavenumber $\overline{k}$ for each topology. This eigenvector contains the displacement vector of each node in the lattice from their initial position in the undeformed state. Note that a mode shape is qualitative in the sense that any scalar multiple of an eigenvector still represents the same mode. We calculate the mode shapes of the five one-dimensional lattices at non-dimensional wavenumbers $\overline{k} = 0$ and π, modeled using frame elements (Fig. 3.4(a)). We obtain the deformed geometries (indicated by solid curves) after displacing the underformed geometries (indicated by dashed lines) by some scalar multiple of the eigenvector (chosen based on adequate magnification) at each wavenumber. Notice that the mode shape in each geometry involves a rigid body translation of the lattice at the low wavenumber and transitions into a more flexural mode of propagation that involves bending of bars at the high wavenumber. Note that the direction of periodicity of these lattices, which is also the direction of propagation of the wave, is indicated by an arrow against each unit cell. In order to verify the mode shapes of propagation, we model the same five lattices in COMSOL with 3-D solid elements. The resulting mode shapes obtained from Bloch wave analyses in these lattices is shown in Fig. 3.4(b). Qualitatively comparing figures 3.4(a) and (b), it is clear that the mode shapes obtained from modeling the lattices as an assembly of bars represented by one dimensional frame elements is almost identical to modeling the whole lattice using 3-D solid elements.

In order to verify the mode shapes quantitatively, we take a look at a non-dimensional parameter that is a characteristic of the mode shape, and its correlation with longitudinal wave speed and mode shape. We have that the mass normalized eigenvector obtained from eq. (3.32) for a given topology

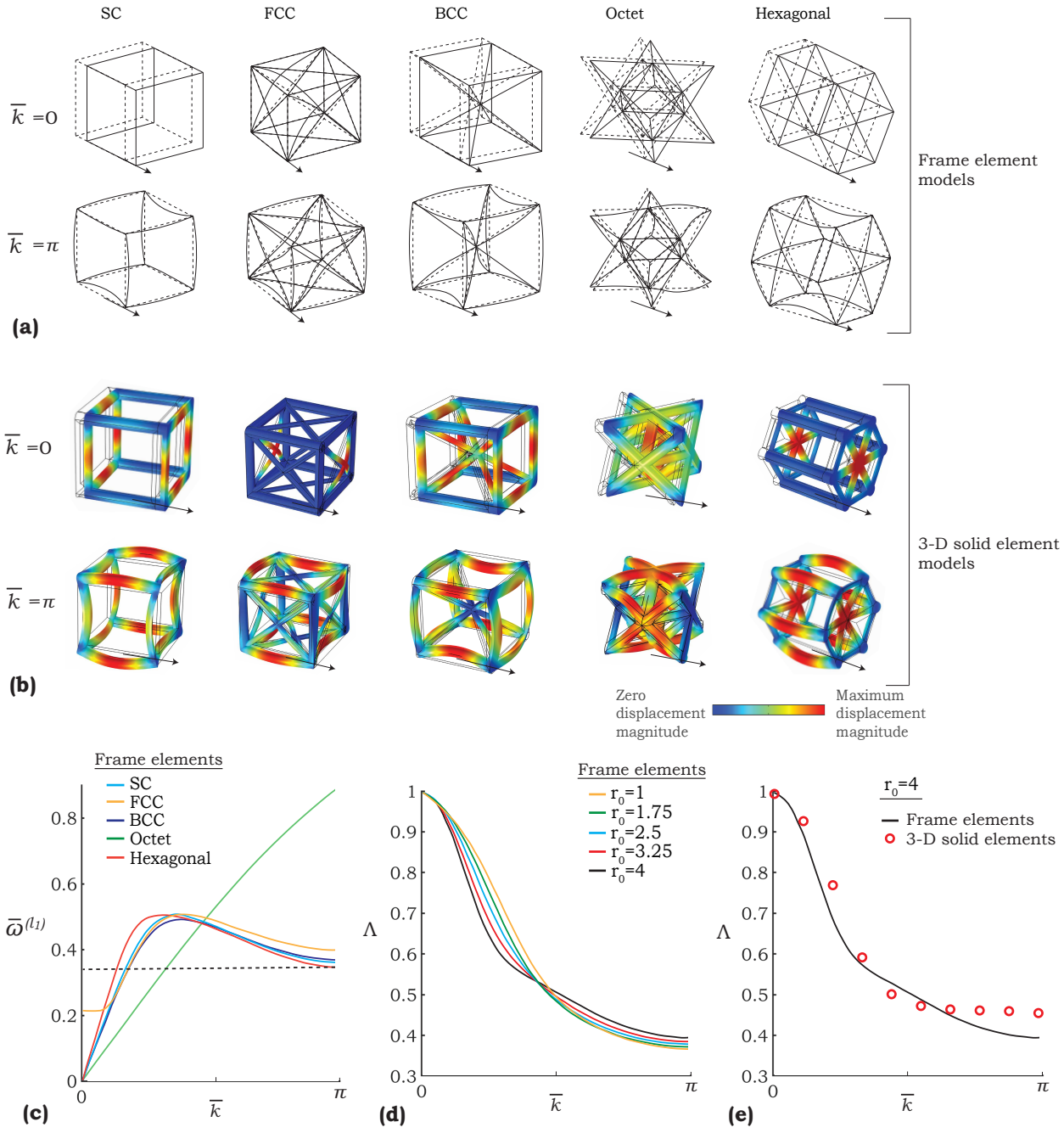

Figure 3.4: Numerical verification: ***(a)*** *and* ***(b)*** *Mode shapes of the five 1-D periodic lattices obtained by modeling them using frame elements and 3-D solid elements, respectively.* ***(c)*** *Dispersion curves for the topologies with highest wave speed of the longitudinal mode considered, in each of the five 1-D lattices at* $\overline{\omega}_0 = 0.35$. ***(d)*** *Variation of parameter* Λ *(eq.* (3.35)*) of the first longitudinal mode for the 1-D BCC lattice, with the non-dimensional wavenumber for five different ratios of cross-sectional areas.* ***(e)*** *Variation of parameter* Λ *of the first longitudinal mode for the BCC lattice with* $r_0 = 4$ *modeled using frame elements and 3-D solid elements.*

and wavenumber is $\overline{\underset{\sim}{U}}$. We can define constant projection matrices $\underset{\sim}{P}_1$, $\underset{\sim}{P}_2$, and $\underset{\sim}{P}_3$ so that the non-zero components of the vectors $\underset{\sim}{P}_1\overline{\underset{\sim}{U}}$, $\underset{\sim}{P}_2\overline{\underset{\sim}{U}}$, and $\underset{\sim}{P}_3\overline{\underset{\sim}{U}}$ indicate the non-zero non-dimensional displacements of the nodes along three mutually perpendicular directions with $\underset{\sim}{P}_1\overline{\underset{\sim}{U}}$ along the direction of wave propagation. Now, we define a ratio

$$\Lambda = \frac{\sqrt{\underset{\sim}{P}_1\overline{\underset{\sim}{U}}.\underset{\sim}{P}_1\overline{\underset{\sim}{U}}}}{\sum_i \sqrt{\underset{\sim}{P}_i\overline{\underset{\sim}{U}}.\underset{\sim}{P}_i\overline{\underset{\sim}{U}}}}, \tag{3.35}$$

which is a non-dimensional measure of the longitudinal displacement (i.e., the displacement along the direction of propagation of the wave) relative to the total displacement of all nodes for the mode under consideration at a given topology and wavenumber of propagation. To study the evolution of this ratio with topology, we pick as an example the one-dimensional BCC lattice with different topologies by varying the area of the diagonal bars. Let r_0 denote the ratio of the non-diagonal bars' cross-sectional area to the diagonal bars' cross-sectional area, with the thickest possible area along the non-diagonal bars. For every topology, we notice that the ratio Λ starts at one (i.e., all displacements are along the direction of propagation of the wave) at $\overline{k} = 0$ and decays to values that are less than half at $\overline{k} = \pi$, as shown in Fig. 3.4(d). This indicates that the majority of displacements at $\overline{k} = \pi$ are perpendicular to the direction of wave propagation. The behavior is consistent with the qualitative mode shapes indicated in Figures 3.4(a) and (b). To quantitatively compare the mode shapes of the lattices modeled using frame elements and 3-D solid elements, we compute the parameter Λ for the BCC lattice with $r_0 = 4$ using both models. The results are shown in Fig. 3.4(e). The mean squared error, calculated between the data points indicated by red circles (3-D solid elements) and the black curve (frame elements) is 0.67%, further indicating that both models display similar longitudinal mode shapes.

In Table 3.2 we compare the non-dimensional group velocities associated with the topologies of the five lattices with maximum wave speed (Fig. 3.3(b) and (d)) modeled using both methods. We see great agreement in measured wave speeds with the two methods as the bounds on the topological vector ensure that the bars remain slender for the most part. The discrepancies mainly occur when the thickest bars are placed between joints that are much closer to each other, reducing their slenderness (ratio of length to diameter), which is often the case to obtain maximum wave speeds in these lattices. For the topology of the BCC lattice with an intermediate wave speed (Fig. 3.3(a)), the non-dimensional wave speed calculated with a model using frame elements is 0.10, while the wave speed of the lattice modeled using 3-D solid elements is 0.245. This discrepancy can be attributed to a low slenderness ratio of 5.88 of the diagonal bars in the optimal design, which implies that the experiments in the next subsection must be verified with the 3-D solid element model over the frame element model for accuracy.

Table 3.2: Comparison of non-dimensional group velocities of lattices that attain maximum $\overline{C}^{(l_n)}$ in Fig. 3.3(b)

Lattice	1-D frame elements	3-D solid elements
Hexagonal	0.70	0.81
SC	0.54	0.57
BCC	0.43	0.50
FCC	0.48	0.46
Octet	0.32	0.40

In Fig. 3.5(a), we show the dispersion curve of the first longitudinal mode plotted using both models for the topologies of BCC lattice with maximum and intermediate wave speeds mentioned in the previous subsection. While the dispersion curves for the lattice with maximum wave speed are nearly identical (dashed curves), the difference in curves for the lattice with an intermediate speed (solid curves) mostly occurs at higher wave numbers and frequencies, where the lattice is more dispersive. As a result, we see differences in wave speeds between the two methods at larger frequencies such as $\omega^* = 0.35$ (black dotted line). We examine the sensitivity of topology variables on the wave speed in the lattice with maximum wave speed. For this lattice, the thickest bars are along the edges while the thinnest bars are along the body diagonal. When modeled using frame elements, the sensitivities of the wave speed with respect to the cross-sectional areas of edge bars, diagonal bars and masses at corners ($\overline{m}_{corner}$) are positive, negative, and negative, respectively, according to eq. (3.14). We verify these trends and ensure that the topology corresponds to a local maximum in wave speed when modeled using 3-D solid elements, as shown in Fig. 3.5(b), (c), and (d). This shows that the extremal topology still remains optimal or displays similar trends in wave speed with respect to topological parameters regardless of the method chosen to model.

3.1.5 Experiments

In this subsection, we explain how our samples are designed and fabricated, and we illustrate a procedure to excite and study the spectro-spatial characteristics of the longitudinal modes. We then measure the wave speed of the first longitudinal mode at a particular frequency in the samples and compare it to the wave speeds computed theoretically. We also experimentally reconstruct the dispersion curves for the selected mode around the frequency of operation, and compare them to our finite element calculations.

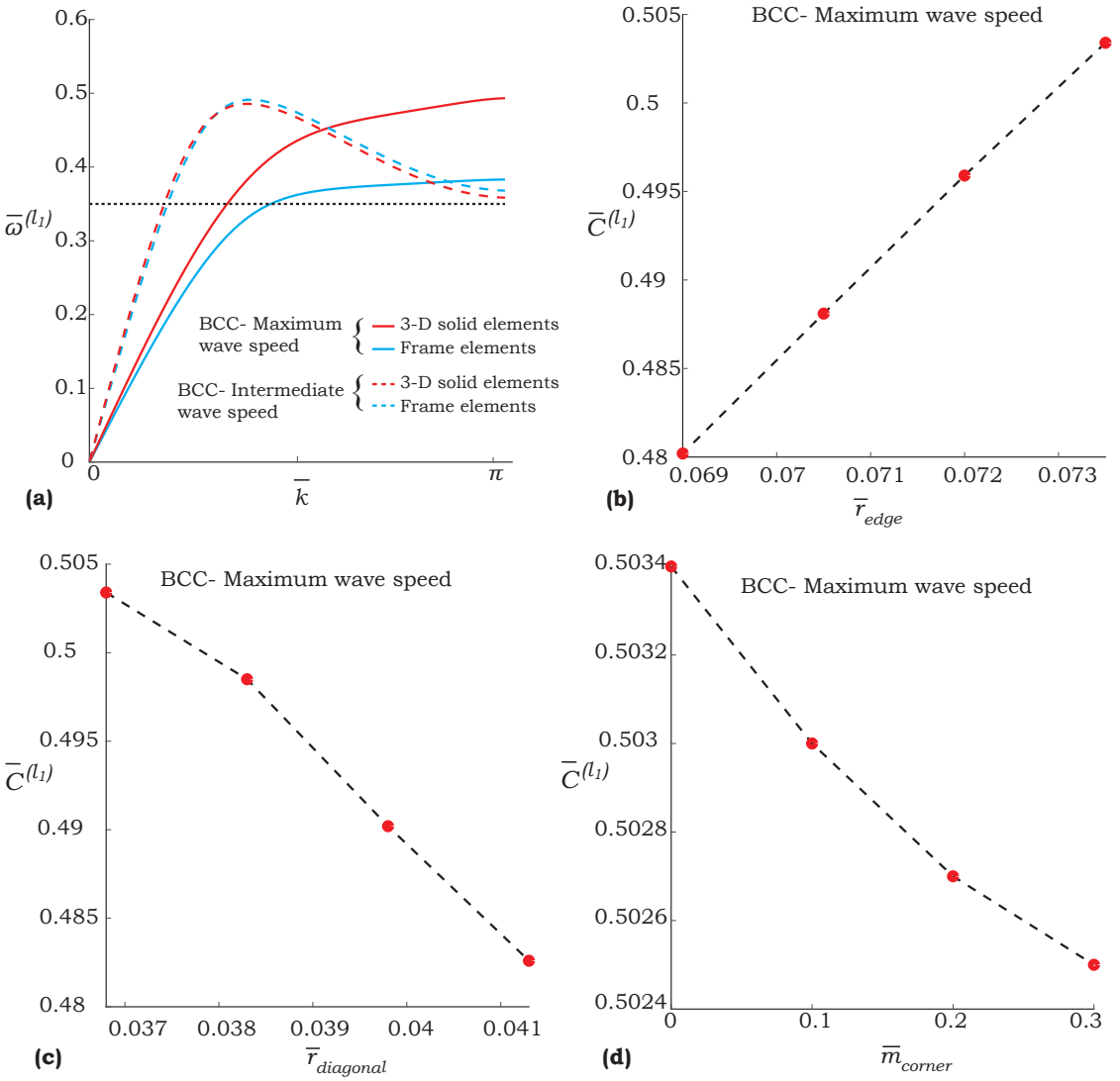

Figure 3.5: Optimal topology: ***(a)*** *Dispersion curves obtained by modeling the BCC lattice with maximum and intermediate wave speeds, using frame elements and 3-D solid elements.* ***(b)***, ***(c)*** *and* ***(d)*** *Variations of wave speeds of BCC lattice with maximum wave speed, with the radius of its edge bars, radius of its diagonal bars, and masses at the corners of a unit cell, respectively, modeled using 3-D solid elements.*

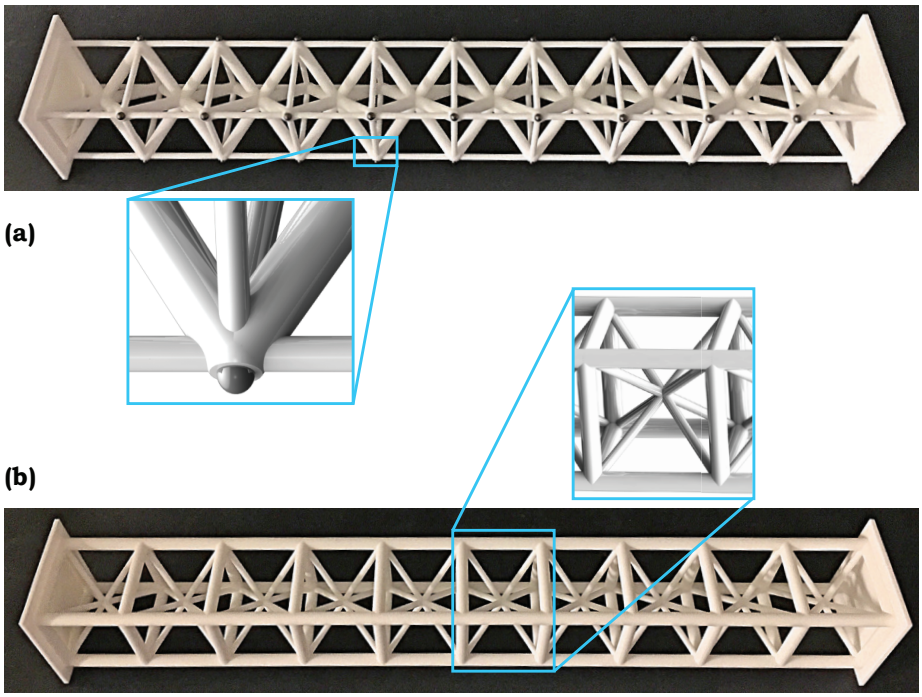

Figure 3.6: Experimental samples: ***(a)*** *BCC lattice with an intermediate wave speed (featuring point masses at the joints, as illustrated in the inset).* ***(b)*** *BCC lattice with the highest wave speed (the inset illustrates a closeup view of the unit cell).*

3.1.5.1 Design of structures with engineered group velocities

We focus our attention on two samples with properties indicated by the dashed lines in Fig. 3.3(a), as these lattices exhibit similar densities but vastly different wave speeds. The optimal values for both topologies are obtained from problem (3.13) and detailed in Section 3.1.4.2. We then pick the closest experimentally realizable topologies (Fig. 3.6). The first corresponds to the BCC lattice with the highest wave speed of 0.504 at $\overline{\omega}^* = 0.35$, and the second has an engineered non-dimensional wave speed of 0.245 at the same frequency, when modeled using 3-D solid elements.

As previously mentioned, in the lattice with the intermediate wave speed, the bars along the diagonal of a unit cell have area $\overline{A} = 17 \times 10^{-3}$ and the bars along the direction of periodicity have area $\overline{A} = 4.25 \times 10^{-3}$, with point masses at the corners with non-dimensional mass $\overline{m} = 5.8 \times 10^{-3}$ (Fig. 3.6(a)). In the lattice with the faster wave speed, the bars along the diagonal have area $\overline{A} = 4.25 \times 10^{-3}$ and the bars along the lattice vector have the area $\overline{A} = 17 \times 10^{-3}$ without any point masses at the joints (Fig. 3.6(b)).

In order to experimentally test the properties of these lattices, we fix our frequency of operation at 2200 kHz ($\omega^* = 350$ rad/s). This frequency gives us a lattice parameter (unit cell length, L) of 34 mm at $\overline{\omega}^* = 0.35$ according to the relation $\overline{\omega}^* = \omega^* \sqrt{\frac{\rho_s}{E_s}} L$. We choose this frequency as it

yields lattices within a convenient length scale to fabricate and test. However, as mentioned in the previous subsections, the designs can be scaled to any frequency of operation as the analysis in non-dimensionalized. A 3-D printed lattice at this length scale can be conveniently manufactured using a selective laser sintering process, which results in a homogeneous distribution of material properties of our chosen material (EOS polyamide PA 2200). These properties are summarized in Table 3.1.

The lattice with intermediate wave speed features non-zero point masses at the cell corners. We realize these experimentally by press-fitting 3 mm diameter tungsten ball bearings made of tungsten carbide into cavities that are designed at the corners of each unit cell, as shown in Fig. 3.6(a). The alloy is over 16 times more dense (density of 14900 $\mathrm{kg/m^3}$) than the solid material that the lattice frame is made of. The fact that we have a relatively high mass within a small volume at the joints supports our assumption of point masses. The sample with the highest wave speed (Fig. 3.6(b)) does not include point masses at the joints and does not need any special assembly after fabrication. As mentioned earlier, we slightly relax the constant density constraint as we are limited by the discrete nature of availability of the ball bearings. We fabricate two sets of samples: arrays of 10 units and arrays of 15 units. The 10-unit arrays are used to measure wave speeds while the longer ones are used for dispersion reconstruction.

3.1.5.2 Setup

The experimental setup is sketched in Fig. 3.7(a). To measure the group velocity through a sample at the frequency ω^*, we construct a burst input signal with four cycles and measure the time taken for the centroid of the wave packet to travel through the sample, as shown with the signals in Fig. 3.7(b). Note that the amplitude of each signal is normalized by the maximum positive amplitude of the input signal. This wave packet is narrow-banded around the frequency of interest, as indicated by the solid curve in Fig. 3.7(c), which is obtained from the DFT of the input signal. The signal is communicated to the signal generator (Agilent 33220A), sent to a piezoelectric amplifier (Piezomechanik LE 150/100 EBW) and to a piezoelectric transducer (Panametrics V1011). The transducer imparts a longitudinal excitation to the base of the lattice array. This ensures that no other modes (shear or torsional) are excited in the lattice. We then use a laser doppler vibrometer (LDV, Polytec OFV-5000) to measure the signal at the base and at the top of the specimen. The signals are read by an oscilloscope (Tektronix DPO3014) and fed back to a computer. The wave speed is then calculated from the signal's time-of-flight between measurement points. We choose arrays of 10 units for the wave speed measurements since this dimension corresponds to over five wavelengths of the longitudinal wave at the frequency of interest. This guarantees separation between the incoming and reflected wave packets when we measure at the top of the array (Fig.

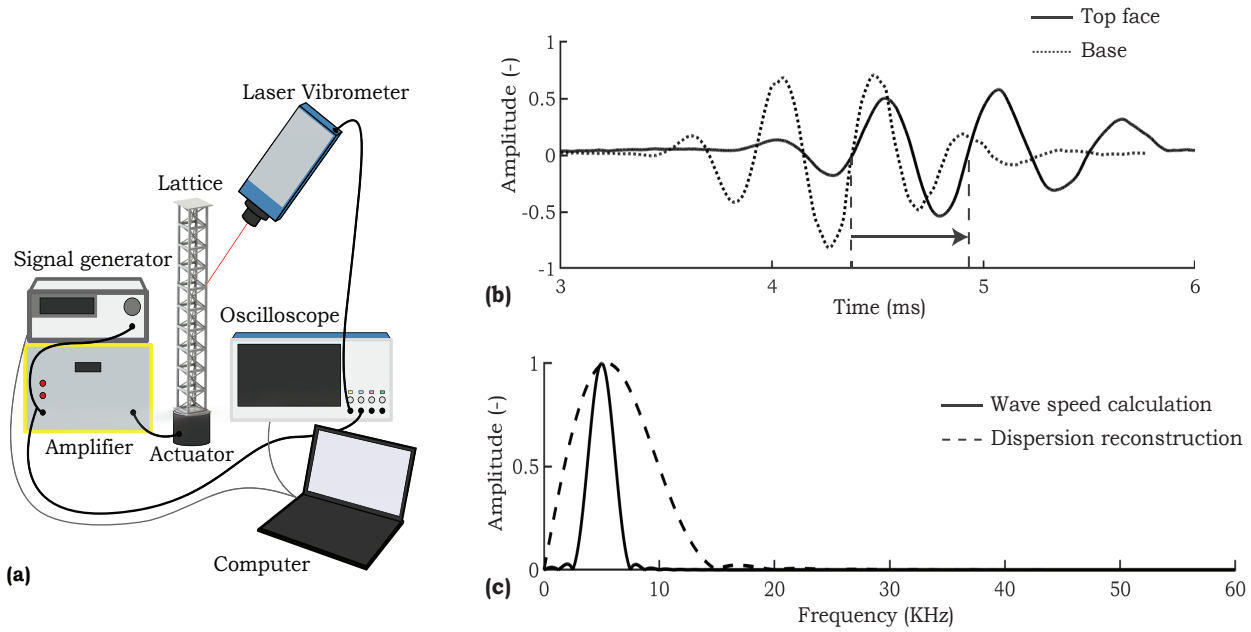

Figure 3.7: Experimental setup: ***(a)*** *Layout of the experimental setup used to measure the elastic wave response of the lattices.* ***(b)*** *Example of a measured transient wave response (normalized) at two points of the lattice.* ***(c)*** *Frequency response of the input signals used to calculate wave speed and reconstruct the dispersion structure.*

3.7(b)). To reconstruct the dispersion properties of the lattice, we instead use a broadband signal (a burst with carrier f_0 but featuring a single oscillation). The wave packet is broader around the frequency of interest, as indicated by the dashed curve in Fig. 3.7(c). We then record the response on the bars that are perpendicular to the direction of wave propagation. The time histories at all measurement points are then collected into a matrix. Upon 2D Discrete Fourier Transform (2D-DFT), we obtain a frequency-wavenumber matrix, containing information on the dispersion characteristics of a truncated lattice, from the time-space data [97]. In this case, we choose arrays of 15 cells since our setup only allows one measurement per cell plus one at the top of the lattice, and 16 measurement points guarantee enough spatial resolution.

3.1.5.3 Results

We record the burst input signal with four cycles at four corners of each sample on the base and its top face. From this, we calculate sixteen wave speeds of the longitudinal mode through a sample. Finally, we compute the group velocity as an average of these sixteen speeds. We repeat this over two samples for each of the BCC lattices, i.e., we obtain the group velocity as the average of 32 wave speeds measured across different points on different samples for each lattice of the types shown in Fig. 3.6. We non-dimensionalize the group velocity by dividing the measured speed by

Table 3.3: Comparison of non-dimensional group velocities between experiments and numerical calculations

Method	Fig. 3.6(a)	Fig. 3.6(b)
Experiments	**0.185 ± 0.002**	**0.485 ± 0.027**
3-D solid elements model	0.245	0.504

$\sqrt{\frac{E_s}{\rho_s}}$ and compare it to our finite element calculations. These results are summarized in Table 3.3. We notice that the numerical and experimental results agree well for the sample with maximum wave speed (Fig. 3.6(b)). We observe a considerable decrease in wave speed on introducing masses (Fig. 3.6(a)) at the joints, as verified by the solid elements model. The slight differences between experiments and numerics can occur due to the fact that the input wave, although concentrated at the frequency of interest, has a slight frequency spread as seen in Fig. 3.7(c). Note that the experimental results show that we can obtain more than a 160% increase in wave speed between the two BCC samples with nearly the same densities—an aspect that can have interesting practical implications.

3.1.5.4 Dispersion reconstruction

To understand if we are indeed measuring experimental wave speeds that correspond to the desired longitudinal mode, we experimentally reconstruct the dispersion relation around the frequency of interest ω^*. Choosing an input burst with just one cycle guarantees that the DFT of this signal has a wide frequency spread around ω^* as indicated by the dashed curve in Fig. 3.7(c). This input signal is used to excite the longer samples and, as explained above, the output signal (amplitude as a function of time) is measured at sixteen equally spaced points starting from the base of the sample to its top. The colormaps in Fig. 3.8 represent the reconstructed frequency vs. wavenumber plots for the two lattices we test. The darkest regions represent the highest amplitudes at a particular frequency and wavenumber. One can notice that some frequencies have higher amplitude than others. This originates from the fact that, due to the limited length of the samples, the recorded signals include several boundary reflections and, therefore, contain some signature of the natural frequencies of the sample [21]. We compare these color-maps to the first longitudinal branches obtained using both a frame element model (blue curve) and 3-D solid element model with COMSOL (red curve). One can appreciate how the numerical results roughly overlap the maxima of the experimental colormaps, indicating agreement between the dispersion for an infinite lattice and the experimental results on a finite sample. The discrepancy in Fig. 3.8(a), where the experiments match the results obtained by modeling the lattice using 3-D solid elements, better than the model that uses frame

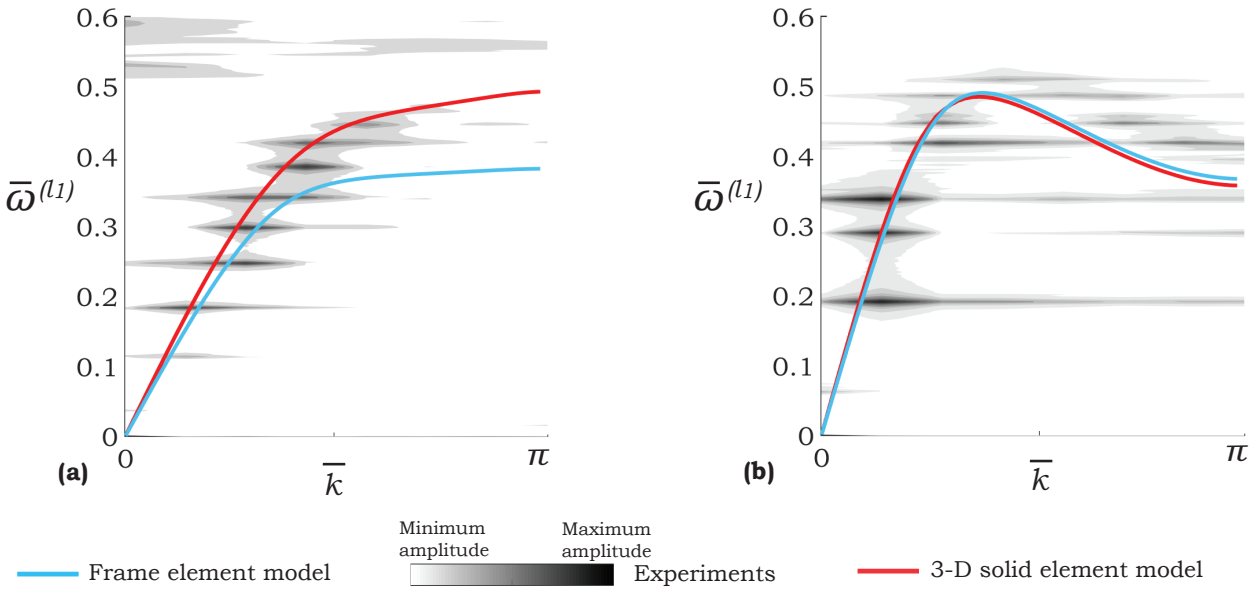

Figure 3.8: Results: ***(a)*** *and* ***(b)*** *Experimental dispersion reconstruction and comparison of the first longitudinal branch for the BCC lattices in Figures 3.6(a) and (b), respectively.*

elements, is consistent with arguments discussed in the previous subsection.

3.1.6 Discussion

We present a sensitivity analysis to optimize the elastic group velocity of a structure at a fixed frequency of propagation together with static properties such as mass density and static stiffness along any chosen direction. In calculating the sensitivities, we provide a method to compute the implicit derivatives, i.e., the sensitivities of the eigenvectors describing the mode shape, with respect to the topology of the structure. We then present a design method to optimize the elastic group velocity in lattice structures, independently from the static properties, density and stiffness. We are able to decouple these properties by adding point masses to the structure at specific locations. We target longitudinal modes in five common lattice structures (SC, BCC, FCC, octet, and hexagonal) and provide bounds on the wave speed with the density and static stiffness of each structure while varying cross-sectional areas of the bars and masses at their joints. The bounds are calculated in the structures by modeling them as an assembly of bars made of several frame elements. We then verify the theoretical model by comparing group velocities and mode shapes of representative structures modeled using 3-D solid elements. To experimentally validate our results, we test two 3-D printed BCC lattices, one with the highest group velocity within our chosen bounds and another with an intermediate wave speed. To verify that the experimentally calculated wave speeds correspond to the desired longitudinal mode, we reconstruct the dispersion relation around the frequency of

operation and compare it to the numerically simulated curves.

The methods presented in this section can be easily extended to optimize the wave speeds of other modes (e.g., shear or torsional) displayed by lattice structures. The non-dimensionalization of our analysis allows us to perform the optimization at a fixed non-dimensional frequency that scales with a chosen length dimension of the lattice for a given frequency of operation. Finally, the analysis in the section can be used to design stiff and lightweight structures with arbitrary dispersion characteristics.

3.1.7 Methods

Method A

The non-dimensional elemental stiffness matrix $\overline{\underset{\sim}{K}}_{el}$ and mass matrix $\overline{\underset{\sim}{M}}_{el}$ are 12×12 symmetric matrices with non-zero elements in their upper triangular portions being

$$\overline{\underset{\sim}{K}}_{el(1,1)} = \overline{A}n,\ \overline{\underset{\sim}{K}}_{el(1,7)} = -\overline{A}n,\ \overline{\underset{\sim}{M}}_{el(1,1)} = \frac{2}{3}\overline{A}\overline{a},\ \overline{\underset{\sim}{M}}_{el(1,7)} = \frac{1}{3}\overline{A}\overline{a}$$
$$\overline{\underset{\sim}{K}}_{el(2,2)} = 12\overline{I}n^3,\ \overline{\underset{\sim}{K}}_{el(2,6)} = 6\overline{I}n^2,\ \overline{\underset{\sim}{K}}_{el(2,8)} = -12\overline{I}n^3,\ \overline{\underset{\sim}{K}}_{el(2,12)} = 6\overline{I}n^2,$$
$$\overline{\underset{\sim}{M}}_{el(2,2)} = \frac{78}{105}\overline{A}\overline{a},\ \overline{\underset{\sim}{M}}_{el(2,6)} = \frac{22}{105}\overline{A}\overline{a}^2,\ \overline{\underset{\sim}{M}}_{el(2,8)} = \frac{27}{105}\overline{A}\overline{a},\ \overline{\underset{\sim}{M}}_{el(2,12)} = -\frac{13}{105}\overline{A}\overline{a}^2,$$
$$\overline{\underset{\sim}{K}}_{el(3,3)} = 12\overline{I}n^3,\ \overline{\underset{\sim}{K}}_{el(3,5)} = -6\overline{I}n^2,\ \overline{\underset{\sim}{K}}_{el(3,9)} = -12\overline{I}n^3,\ \overline{\underset{\sim}{K}}_{el(3,11)} = -6\overline{I}n^2,$$
$$\overline{\underset{\sim}{M}}_{el(3,3)} = \frac{78}{105}\overline{A}\overline{a},\ \overline{\underset{\sim}{M}}_{el(3,5)} = -\frac{22}{105}\overline{A}\overline{a}^2,\ \overline{\underset{\sim}{M}}_{el(3,9)} = \frac{27}{105}\overline{A}\overline{a},\ \overline{\underset{\sim}{M}}_{el(3,11)} = \frac{13}{105}\overline{A}\overline{a}^2,$$
$$\overline{\underset{\sim}{K}}_{el(4,4)} = \frac{G_s}{E_s}\overline{J}n,\ \overline{\underset{\sim}{K}}_{el(4,10)} = -\frac{G_s}{E_s}\overline{J}n,\ \overline{\underset{\sim}{M}}_{el(4,4)} = \frac{2}{3}\overline{A}\overline{a}\overline{r}^2,\ \overline{\underset{\sim}{M}}_{el(4,10)} = -\frac{1}{3}\overline{A}\overline{a}\overline{r}^2$$
$$\overline{\underset{\sim}{K}}_{el(5,5)} = 4\overline{I}n,\ \overline{\underset{\sim}{K}}_{el(5,9)} = 6\overline{I}n^2,\ \overline{\underset{\sim}{K}}_{el(5,11)} = 2\overline{I}n,$$
$$\overline{\underset{\sim}{M}}_{el(5,5)} = \frac{8}{105}\overline{A}\overline{a}^3,\ \overline{\underset{\sim}{M}}_{el(5,9)} = -\frac{13}{105}\overline{A}\overline{a}^2,\ \overline{\underset{\sim}{M}}_{el(5,11)} = -\frac{6}{105}\overline{A}\overline{a}^3,$$
$$\overline{\underset{\sim}{K}}_{el(6,6)} = 4\overline{I}n,\ \overline{\underset{\sim}{K}}_{el(6,8)} = -6\overline{I}n^2,\ \overline{\underset{\sim}{K}}_{el(6,12)} = 2\overline{I}n,$$
$$\overline{\underset{\sim}{M}}_{el(6,6)} = \frac{8}{105}\overline{A}\overline{a}^3,\ \overline{\underset{\sim}{M}}_{el(6,8)} = \frac{13}{105}\overline{A}\overline{a}^2,\ \overline{\underset{\sim}{M}}_{el(6,12)} = -\frac{6}{105}\overline{A}\overline{a}^3,$$
$$\overline{\underset{\sim}{K}}_{el(7,7)} = \overline{A}n,\ \overline{\underset{\sim}{M}}_{el(7,7)} = \frac{2}{3}\overline{A}\overline{a},$$
$$\overline{\underset{\sim}{K}}_{el(8,8)} = 12\overline{I}n^3,\ \overline{\underset{\sim}{K}}_{el(8,12)} = -6\overline{I}n^2,\ \overline{\underset{\sim}{M}}_{el(8,8)} = \frac{78}{105}\overline{A}\overline{a},\ \overline{\underset{\sim}{M}}_{el(8,12)} = -\frac{22}{105}\overline{A}\overline{a}^2$$
$$\overline{\underset{\sim}{K}}_{el(9,9)} = 12\overline{I}n^3,\ \overline{\underset{\sim}{K}}_{el(9,11)} = 6\overline{I}n^2,\ \overline{\underset{\sim}{M}}_{el(9,9)} = \frac{78}{105}\overline{A}\overline{a},\ \overline{\underset{\sim}{M}}_{el(9,11)} = \frac{22}{105}\overline{A}\overline{a}^2$$
$$\overline{\underset{\sim}{K}}_{el(10,10)} = \frac{G_s}{E_s}\overline{J}n,\ \overline{\underset{\sim}{M}}_{el(10,10)} = \frac{2}{3}\overline{A}\overline{a}\overline{r}^2,$$
$$\overline{\underset{\sim}{K}}_{el(11,11)} = 4\overline{I}n,\ \overline{\underset{\sim}{M}}_{el(11,11)} = \frac{8}{105}\overline{A}\overline{a}^3,$$
$$\overline{\underset{\sim}{K}}_{el(12,12)} = 4\overline{I}n,\ \overline{\underset{\sim}{M}}_{el(12,12)} = \frac{8}{105}\overline{A}\overline{a}^3,$$

where n is the number of elements in the bar, L is the length of the lattice vector, $\overline{A} = \frac{A}{L^2}$ with A being the circular cross-sectional area of the beam and $\overline{a} = \frac{L_{bar}}{2nL}$. L_{bar} is the total length of the bar that the element is a part of. $\overline{I} = \frac{\overline{A}^2}{4\pi}$, $\overline{r} = \frac{\overline{A}}{2\pi}$, and $\overline{J} = 2\overline{I}$ are the non-dimensional planar second moment of area, radius of gyration, and polar second moment of area, respectively. G_s, the shear modulus of rigidity can be calculated as $\frac{E_s}{2(1+\nu)}$ for the linear elastic material, where E_s and ν are the Young's modulus of elasticity and Poisson's ratio, respectively.

Method B

Algorithm 4 Non-dimensional frequency of propagation $\overline{\omega}^{(l_n)}$ of the n^{th} longitudinal mode for a non-dimensional wavenumber $\overline{k}$

For the fixed topology $\underset{\sim}{\overline{\chi}}$ of the unit cell and $\overline{k}$, find the eigenvalues and associated eigenvectors of $\underset{\sim}{\overline{M}}^{-1}\underset{\sim}{\overline{K}}$ ($\overline{\omega}_i^2$ and $\underset{\sim}{\overline{U}}_i,\ i = 1, \ldots, size\left(\underset{\sim}{\overline{M}}\right)$)
Modify $\underset{\sim}{\overline{U}}_i$ by subtracting from the displacement of each node, the displacement of the centroid of the unit cell
Compute the direction cosines of each bar before displacement, $\underset{\sim}{d}_j,\ j = 1, \ldots,$ number of bars
Denote the set of indices of bars on the outer frame of the front face of the unit cell by S1
Denote the set of indices of bars along $\underset{\sim}{\hat{k}}$ (direction of wave vector) by S2 and perpendicular $\underset{\sim}{\hat{k}}$ by S3. $\hat{(.)}$ represents a unit vector.
count=0
for $i = 1 : 1 : size\left(\underset{\sim}{\overline{M}}\right)$ **do**
    compute the direction cosines of the line joining the displaced end points of each bar, $\underset{\sim}{e}_j$ and the mean displacement of nodes along each bar $\underset{\sim}{v}_j$, $j = 1, \ldots,$ number of bars
    $p = 1$
    for $k = 1 : 1 : size(S1)$ **do**
        $p = p \times |\underset{\sim}{d}_{S1(k)}.\underset{\sim}{e}_{S1(k)}|$ (Indicates a shear/ torsional distortion of lattice if $p < 1$)
    end for
    $q = 1$
    for $k = 1 : 1 : size(S2)$ **do**
        $q = q \times \left(1 - |\underset{\sim}{\hat{k}}.\underset{\sim}{\hat{v}}_j|\right)$
    end for
    $t = 1$
    for $k = 1 : 1 : size(S3)$ **do**
        $t = t \times |\underset{\sim}{\hat{k}}.\underset{\sim}{\hat{v}}_j|$
    end for
    $s = p \times q \times t$ (s=1 for a longitudinal mode)
    if $s == 1$
        count=count+1
        if count== n
            break all
        end if
    end if
end for
$\overline{\omega}^{(l_n)} = \overline{\omega}_i$

Chapter 4

ENGINEERING A MODE DEMULTIPLEXER

Research presented in this chapter has been adapted from the following publication:

Injeti, S. S., Bhattacharya, K. & Daraio, C. Data intensive architecture of a mode demultiplexer. *In preparation* (2021).

4.1 Data intensive architecture of a mode demultiplexer

4.1.1 Motivation

Analogues to electronic devices in phononic (elastic and acoustic) and photonic (electromagnetic) systems can open up a plethora of applications in wireless information transfer and processing. A mode demultiplexer, a device that can decouple mixed modes of wave propagation, can allow for increased data transmission over fewer lines and help realize more efficient thermal and acoustic computers. However, most studies have focused on manipulating vibrations associated with a single mode of wave propagation, whereas designing a demultiplexer requires simultaneously controlling multiple arbitrarily chosen modes spanning several frequencies. This is the focus of our work. We couple a sensitivity analysis to track the wave speeds and frequency band gaps associated with any mode of choice in a structure, with a data-intensive method to design a metamaterial-based mode demultiplexer. This device consists of multiple architected lattice channels, each capable of extracting a different mode in a range of frequencies from a mixed elastic vibration. We validate our designs with experiments on 3-D printed lattices that decouple a mixed signal containing both longitudinal and shear elastic waves. As a result of low relative densities of lattices, these channels could be interpenetrated into each other without contact, enabling extremely compact demultiplexing. The design methodology presented could help pave the way towards economic thermal and acoustic computing.

4.1.2 Introduction

Exploiting the periodicity in materials has been useful to control waves in phononic [16, 111] and photonic [38, 81] systems. Specifically in phononics, architected lattices have proven effective due to their ease of fabrication spanning vast length scales and materials using additive manufacturing [7, 35, 58, 84, 89, 103]. But more importantly, they allow us to manipulate waves with complex modal behavior [56]. Due to the heterogeneous nature of these metamaterials, waves propagating through the structure undergo dispersion, giving rise to properties such as frequency band gaps [16] that are key in designing a mode demultiplexer. In order to demultiplex a mixture of multiple

modes, we create individual channels (lattices periodic in one direction as shown by the schematic in Fig. 4.1(a)), where each channel dissipates the energy associated with all but one mode at a frequency, i.e. the mode that the channel propagates.

Fig. 4.1(b) shows a schematic of a dispersion plot between frequency ω and wavenumber k (magnitude of wave vector $\underset{\sim}{k}$) of propagation of waves through a heterogeneous periodic structure. We obtain such a plot by solving the following eigenvalue problem obtained on a discretized domain and applying Bloch's theorem [49],

$$\underset{\sim}{K}(\underset{\sim}{k})\underset{\sim}{u}(\underset{\sim}{k}) = \omega(\underset{\sim}{k})^2\underset{\sim}{M}(\underset{\sim}{k})\underset{\sim}{u}(\underset{\sim}{k}). \tag{4.1}$$

For a structure modeled using finite elements, $\underset{\sim}{K}$ and $\underset{\sim}{M}$ are the self-adjoint stiffness and mass matrices [56]. We solve eq. (4.1) at distinct wave vectors along a path called the irreducible Brillouin zone ($\mathcal{B}$) [16]. In this section, we consider waves propagating along a periodic lattice channel made of unit cells repeating along one-direction $\underset{\sim}{\hat{\theta}}$, the wave vector can be written as $\underset{\sim}{k} = k\underset{\sim}{\hat{\theta}}$. $\mathcal{B}$ contains wavenumbers that belong to the range $[0, \pi/L]$, where L is the lattice parameter i.e. length of a unit cell along the direction of periodicity. The eigenvector/mode shape $\underset{\sim}{u}$ (vector of displacements at nodes in the finite element domain) and angular frequency ω are obtained by solving the eigenvalue problem at wave vector $\underset{\sim}{k}$. We normalize the eigenvector in our analysis such that $\underset{\sim}{u}.\underset{\sim}{M}\underset{\sim}{u} = 1$. If a majority of nodes displace along the wave vector, the mode shape is said to describe a longitudinal mode. If the displacements of nodes are primarily in an orthogonal direction to the wave propagation, the mode shape describes a shear mode. Let us say that in Fig. 4.1(b) the first three shear modes are tracked by the blue curves, the first shear band gap (a frequency range where no shear waves propagate) is indicated by the blue shaded region, and the first longitudinal mode by the orange curve. Such a structure (Fig. 4.1(b)) would propagate a longitudinal wave at frequencies in the shear band gap while dissipating shear modes. Hence, putting together multiple such structures that possess band gaps associated with specific modes at desired frequencies, while propagating certain other modes at those frequencies can help us realize a demultiplexer.

4.1.3 Design of the demultiplexer

Traditionally, identifying and tracking specific modes for a given structure on the dispersion curve involves solving the eigenvalue problem (eq. (4.1)) at a large number of distinct wavenumbers and visually inspecting the mode shapes (eigenvectors) associated with each frequency [82, 126]. For complex structures, which demonstrate interesting wave propagation characteristics, this becomes a cumbersome task. For example, in [56], the authors show that longitudinal modes in several cubic lattices periodic in one direction start as rigid body motion at low wavenumber and transition to flexural deformation of certain bars at higher wavenumber, implying steep changes in mode shapes with wavenumber. This makes the automation of mode tracking challenging. We overcome this

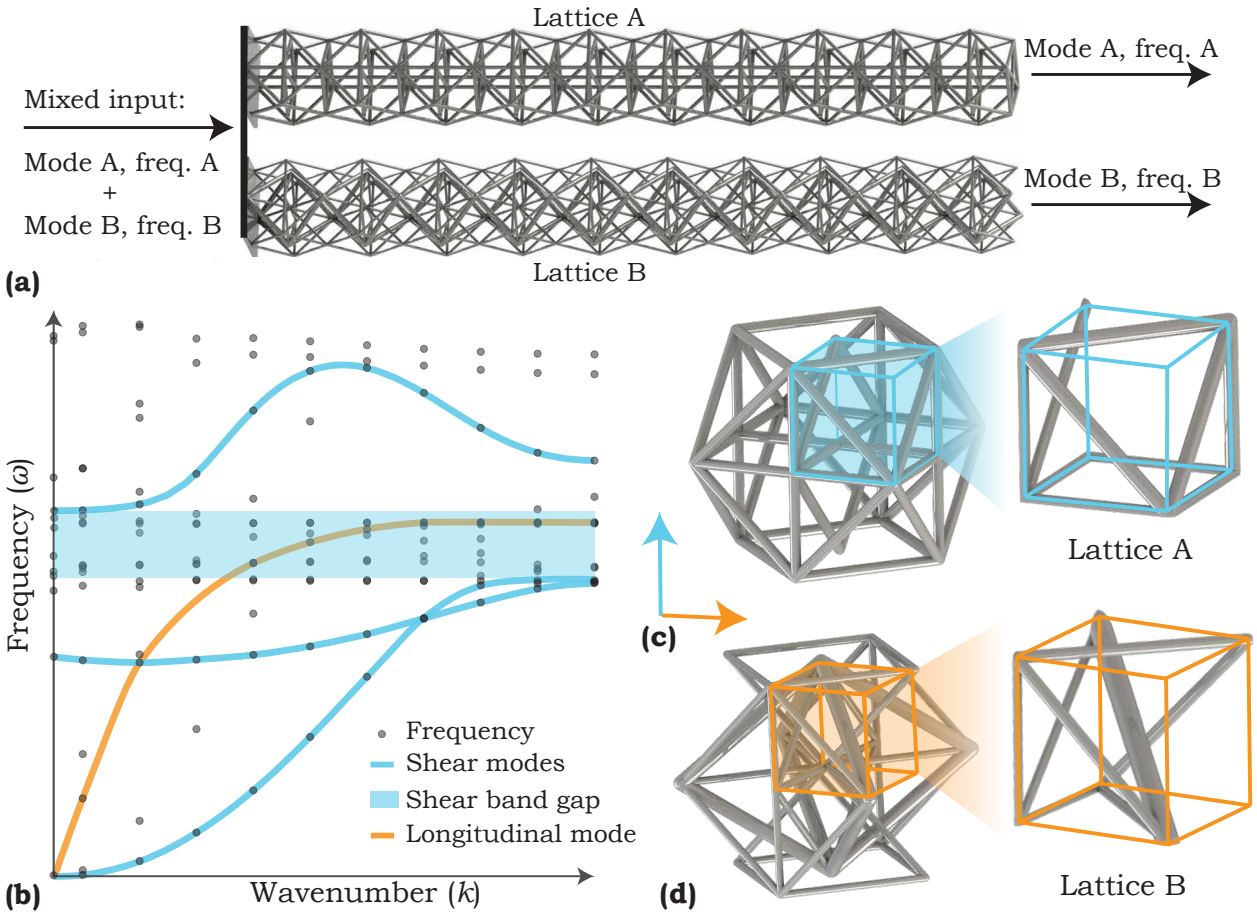

Figure 4.1: Mode demultiplexer: ***(a)*** *Example of a mode demultiplexer consisting of two lattice channels.* ***(b)*** *Schematic of a dispersion plot indicating the first three shear modes, the first shear band gap, and a longitudinal mode.* ***(c)*** *and* ***(d)*** *Unit cells of lattices that propagate longitudinal modes and dissipate shear modes ((c)), and propagate shear modes and dissipate longitudinal modes ((d)), in the same frequency range. The direction of periodicity is indicated by the longitudinal direction (orange arrow) and the blue arrow indicates direction of shear vibrations.*

issue by using a mode tracking algorithm (Appendix) that estimates the frequency of a mode being tracked from one wavenumber to the next for any general structure. We do so by estimating the eigenvectors up to the first derivative, and frequencies up to the second derivative with respect to the wavenumber, allowing us to automate the process of mode tracking and solve the eigenvalue problem at much fewer wavenumbers (see Methods). The algorithm described can be used to track modes for a structure with arbitrary heterogeneities, that may even intersect other similar modes on the dispersion curve. Owing to the automation of our mode tracking algorithm and modal richness displayed by lattices, we employ a data-intensive method where we study several lattice geometries (modeled using frame elements – a combination of beam and truss elements [56]) and several modes of interest associated with each structure.

In order to build a large database of lattice structures periodic in one direction, we focus our attention on lattices made from repeating cubic symmetric unit cells. Each unit cell can be constructed through reflections of an octant about mutually orthogonal planes as seen in Fig. 4.5. Fig. 4.1(c), (d) show two such examples. These unit cells can be made fairly complex with the arrangement of bars within them, allowing for interesting dispersion behavior. We construct a database of unit cells containing close to 1 million cubic symmetric geometries using an algorithm, which ensures compatibility (non-intersecting bars) within an octant and structural stability (no dangling bars) as described in Appendix. Further, we fix a uniform slenderness ratio T (ratio of strut length to diameter) for each bar in an octant to 10, lattice parameter L (equal to unit cell length) of 30 mm, and material properties (Young's modulus E, density ρ, and Poisson's ratio ν) of the base material we use to 3-D print our samples for experiments (see Methods) while building the database. Finally, we can study the modal behavior associated with several modes of choice for a large number of lattices (a thousand randomly selected) that are part of this database, using our mode tracking algorithm. Although we fix the values of parameters L, E, and ρ, we non-dimensionalize our analysis and as a result, the frequencies of associated modes in the dispersion curve would scale for other values of those parameters as detailed in Appendix.

In our work, as a proof of concept we consider an input wave that is a combination of longitudinal and shear waves at a certain frequency (f_0 =1435 Hz), and we wish to separate these waves. However, the method can be easily extended to other modes with a similar analysis, and we also show that the input signal can be separated even with a mixture of frequencies. The non-dimensional frequency of the signal is calculated as $\overline{\omega}_0 = 2\pi f_0 \sqrt{\frac{\rho}{E}} L$ ($\overline{\omega}_0 = 0.2$ for values of parameters mentioned above). We then choose two lattices from the database, one that displays a longitudinal band gap with shear wave propagation at the frequency of interest $\overline{\omega}_0$, while another exhibits a shear band gap with longitudinal wave propagation at the same frequency. The unit cells associated with these lattices have connectivities as shown in Fig. 4.1(c), (d). Once we obtain these lattices from the database

(with uniform slenderness of struts), we engineer the topology such that the frequency $\overline{\omega}_0$ is within the band gap but away from a band edge (see Methods). The results are depicted in Fig. 4.1(c), (d). Lattice A contains bars with uniform cross-sectional areas, i.e. slenderness ratio of 10 for the bars along the edge of the octant and slenderness ratio of 14.14 for bars along the face diagonal of the octant. In lattice B, the slenderness ratio of bars along the edge of the octant is 14.14, along the face diagonal of the octant is 20, and along the body diagonal of the octant is 12.25.

The dispersion curves corresponding to the longitudinal and shear modes in both lattices are shown in Fig. 4.2(a),(b), obtained using the mode tracking algorithm. Note that we non-dimensionalize the wavenumber as $\overline{k} = kL$, and the range of non-dimensional wavenumbers is $[0, \pi]$. $\overline{\omega}$ is calculated from the angular frequency ω, as $\overline{\omega} = \omega\sqrt{\frac{\rho}{E}}L$. Lattice A propagates a longitudinal mode within the first shear band gap at $\overline{\omega}_0 = 0.2$, while lattice B propagates a shear mode within the second longitudinal band gap at the same frequency. The corresponding non-dimensional (dimensional) band gaps in lattices A and B are 0.144 (1032.9 Hz) and 0.084 (602.5 Hz), respectively. The group velocity of the propagating mode can be calculated as the slope on the dispersion curve, i.e. $\frac{d\overline{\omega}}{d\overline{k}}$, indicated by the slope of the dashed lines in Fig. 4.2(a),(b). The corresponding non-dimensional (dimensional) wave speeds in lattices A and B are 0.265 (358.3 m/s) and 0.167 (225.8 m/s), respectively.

Understanding the bounds on attainable wave speed and band gap of a lattice is important while choosing target values for the material properties. We find these bounds on attainable values by varying the non-dimensional cross-sectional areas of the bars (cross-sectional area divided by L^2), which can also be thought of as varying the slenderness ratios of bars. We obtain the convex envelope of the attainable region by minimizing the weighted combination of bang gap and wave speed for several weights using a sensitivity analysis (see Methods and Appendix). The results of this optimization for lattices A and B are shown in Fig. 4.2(c),(d). We set the minimum slenderness ratio within an octant to be 10 and the maximum to be 25, remaining in a range where the bars are slender enough to be modeled using frame elements [56]. In order to reach close to the global optima, we start the gradient-based optimization algorithm from several initial guess values. Note that every combination of values in the shaded region may not be achieved, but the values at the corners of the shaded regions are achieved. Such points are of interest as the extremal properties occur there. In order to engineer a specific combination of properties of each lattice in the shaded region, we would optimize a norm of the difference between the property (wave speed or band gap) and the target value using the same sensitivity analysis.

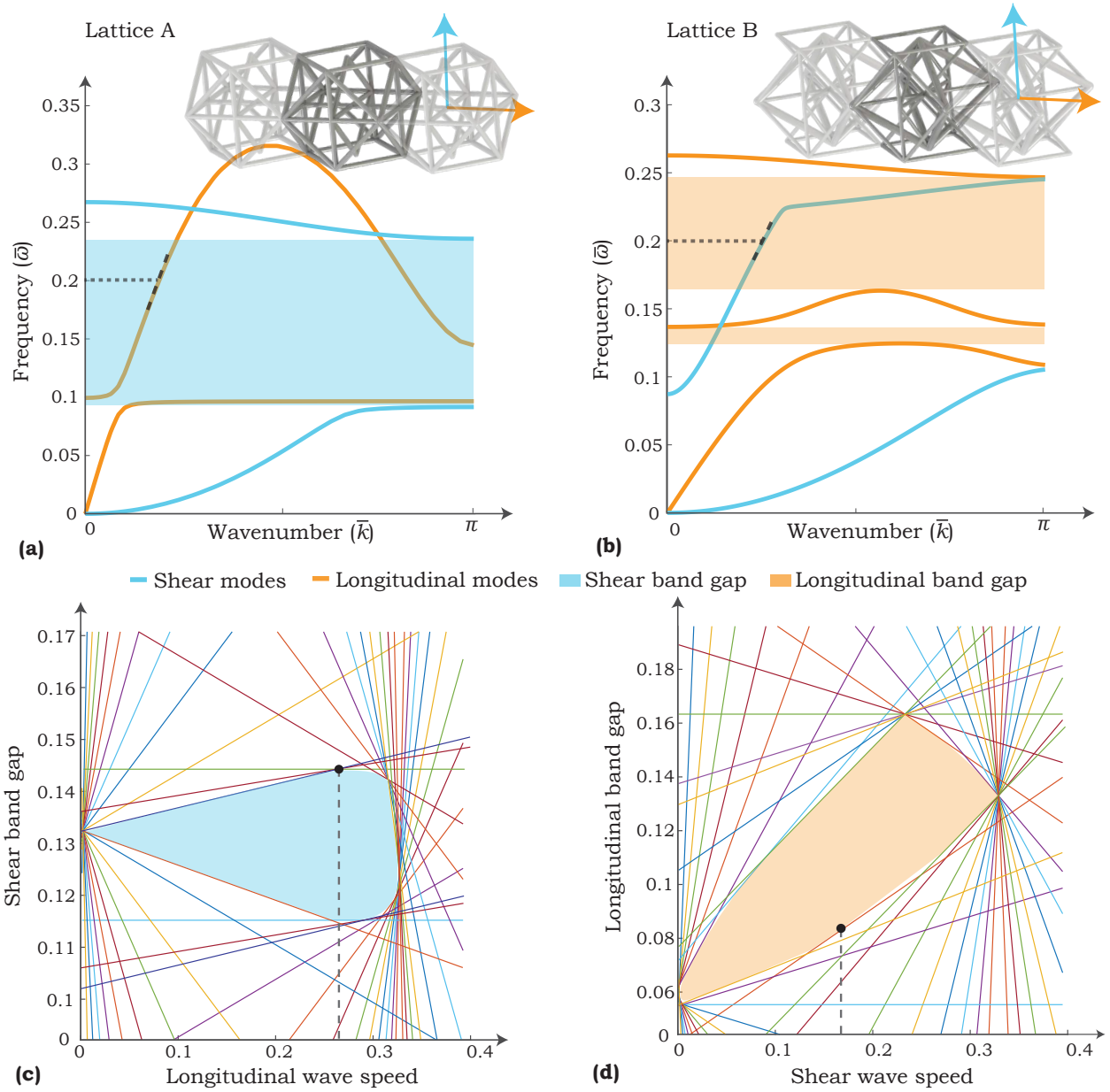

Figure 4.2: Bounds on properties: ***(a)*** *and* ***(b)*** *Shear and longitudinal modes tracked in lattices A and B. The respective band gaps are shaded in blue and orange with the slope of dashed lines indicating group velocity.* ***(c)*** *and* ***(d)*** *Bounds on the attainable band gap and wave speed values, in lattices A and B. The properties of designs in (a) and (b) (experimentally tested designs) marked with black dots.*

4.1.4 Experiments and results

We chose to fix the frequency f_0 at 1435 Hz and the lattice parameter of each lattice at L = 30 mm. As a result, the non-dimensional frequency is fixed at $\overline{\omega}_0 = 0.2$. However, we can vary the unit cell length in each lattice across a range while still splitting the mixed wave at a frequency of 1435 Hz, owing to the width of bang gaps in either lattice. For example, in lattice A, we could shrink the lattice parameter down to 20 mm and the non-dimensional frequency now associated with 1435 Hz is at $\overline{\omega}_0 = 0.13$, which still falls in the blue shaded region in Fig. 4.2(a). We test in experiments each lattice A and B with a lattice parameter of L = 30 mm and theoretical wave speed and band gap mentioned earlier, and indicated by the black dots in Fig. 4.2(c),(d). We excite both lattices with a mixture of modes at the same frequency (f_0 = 1435 Hz), but note from Fig. 4.2(a),(b) and subsequently in experiments that we can separate a mixture with different frequencies that lie in a range common to both band gaps. This means the frequencies of longitudinal and shear modes can be different and anywhere in between 1196 Hz and 1675 Hz and still be separated, as can be deduced from Fig. 4.2(a) and (b).

We pick 10 unit cells in each 3-D printed structure to allow for sufficient wavelengths within the length of the structure to approximate the behavior of infinite lattices (Fig. 4.3(a)). The wedge (base of the samples) at the surface of the piezoelectric actuator in Fig. 4.3(b) simulates a combined longitudinal and shear excitation, along the orange and blue arrows in Fig. 4.3(a), respectively. The sample preparation and experimental setup are detailed in Methods.

We first measure the frequency transmission – ratio of output frequency response at the top unit cell of each lattice to the input at the base (see Methods). For maximum response anticipated from the mode shapes (Fig. 4.8(a)), we pick the body center of the unit cell (orange dot in Fig. 4.3(a)) to measure the longitudinal response, while orienting the vibrometer along the orange arrow. Similarly, we pick the edge center (blue dot in Fig. 4.3(a)) to measure the shear response along the blue arrow. To measure the transmission, the frequency spectrum of input signal centered around f_0 is shown in Fig. 4.7(a). Fig. 4.4(a),(b) indicate a clear shear band gap in the response of lattice A and a longitudinal band gap in the response of lattice B, as predicted. We also perform numerical simulations on the finite structures with each strut modeled using frame elements (details in Appendix). We see great agreement in regions of attenuation between the theoretically predicted values (for infinite lattices), numerical results (for lattices with 10 unit cells), and experiments, for both lattices A and B. Also, Fig. 4.4(c),(d) show healthy transmission of the longitudinal wave (in lattice A) and shear wave (in lattice B) over a range of frequencies as designed, and confirmed by both experiments and numerical simulations.

Further, we reconstruct the dispersion curve for the propagating modes in each lattice using an input signal with a frequency spectrum shown in Fig. 4.7(a), to compare the dominant propagating

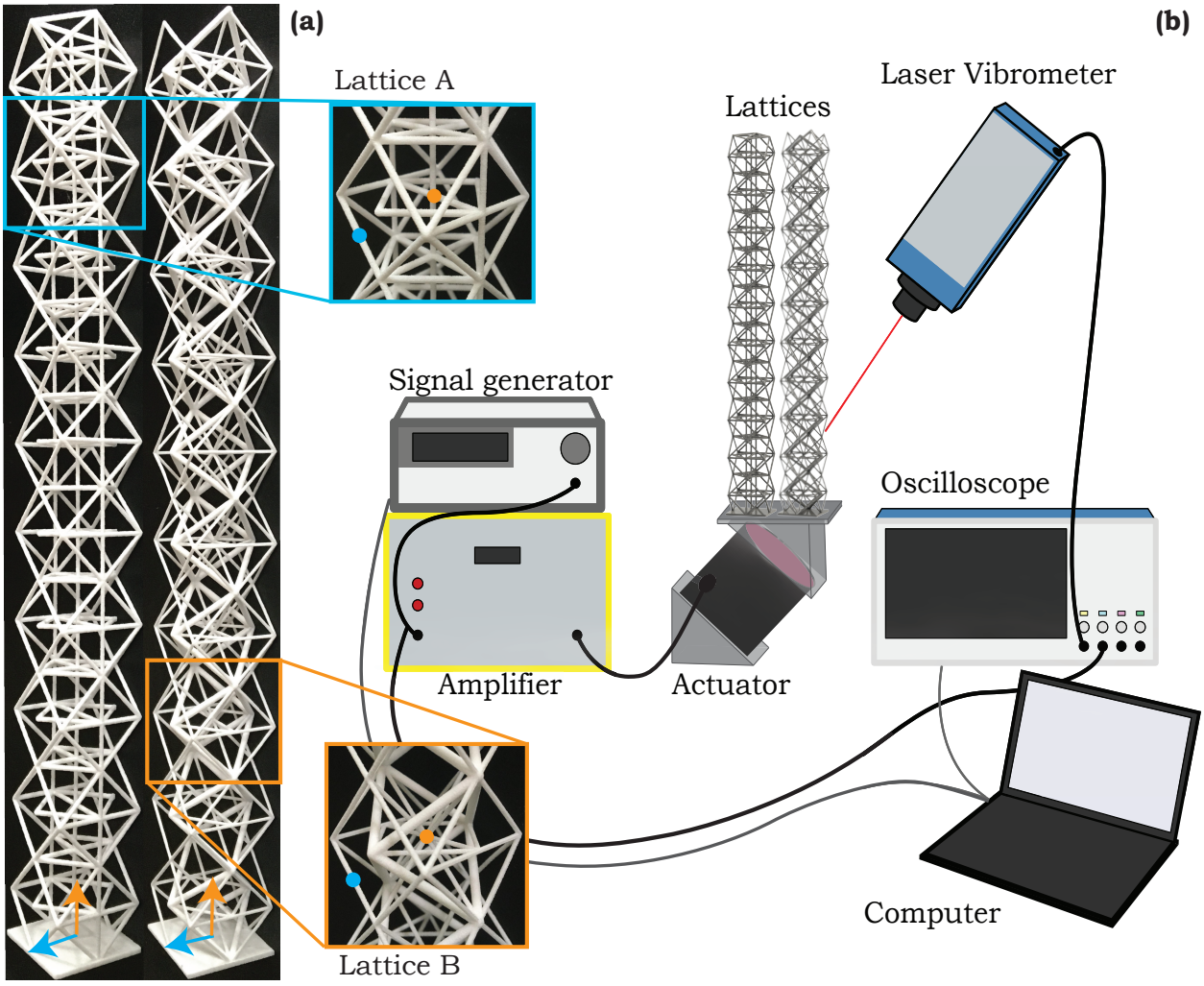

Figure 4.3: Experimental setup: ***(a)*** *3-D printed lattices A and B, with equal lattice parameters (L = 30 mm). The longitudinal and shear directions are indicated by orange and blue arrows, respectively. Orange and blue dots in the close-up views of the unit cells indicate measurement points for longitudinal and shear response, respectively.* ***(b)*** *Experimental setup layout to measure the elastic wave response in each lattice and demonstrate decoupling of the mixed signal at* f_0 = 1435 Hz.

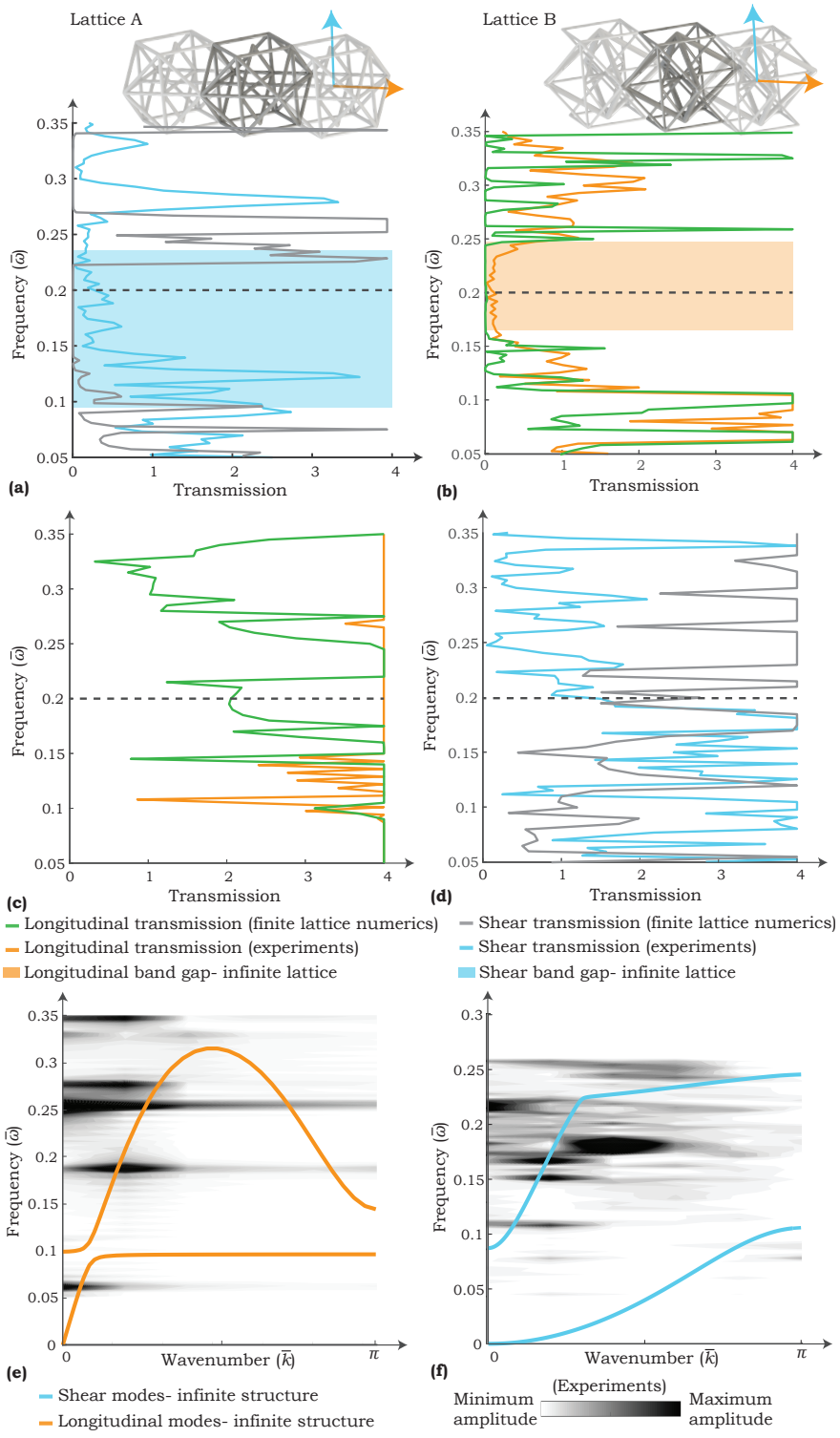

Figure 4.4: Results: ***(a)*** *and* ***(b)*** *Frequency transmission comparing experiments, numerics, and theory, showing attenuation of shear waves lattice in A and longitudinal waves in lattice B.* ***(c)*** *and* ***(d)*** *Frequency transmission comparing numerics and experiments, showing propagation of longitudinal waves in lattice A and shear waves in lattice B.* ***(e)*** *and* ***(f)*** *Dispersion reconstruction of the propagating longitudinal mode (in lattice A) and shear mode (in lattice B).*

frequencies (see Methods). As shown in 4.4(e),(f), we see propagation of waves (longitudinal in lattice A and shear in lattice B) for a range around the frequency of interest ($\overline{\omega}_0 = 0.2$). The dominant frequencies of propagation at a wavenumber are indicated by the darker regions. In this calculation, due to the finite nature of the samples, we are limited to fewer discrete wavenumber measurements and we may also observe effects due to boundary reflections. Finally, with the mixed input wave packet shown in Fig. 4.7(b), we measure the wave speed of propagation close to 1435 Hz of the longitudinal mode in lattice A as 424.9 ± 2.2 m/s and of the shear mode in lattice B as 210.8 ± 1.1 m/s (details in Methods). These values compare well with the theoretically predicted values for the infinite structures (358.3 m/s and 225.8 m/s for lattices A and B, respectively).

We demonstrate a conceptual design of a mode demultiplexer which is capable of separating mixed modes of wave propagation into its individual components spanning multiple frequencies. Using a data-intensive method, we pick lattices that propagate and dissipate selected modes, and further optimize their properties (wave speeds and band gaps) using a sensitivity analysis. Given our non-dimensional analysis along with the slenderness of struts in a lattice, the resulting channels can be *woven* into each other giving us close-packed demultiplexers that are load-bearing. The proposed method can be used to decouple arbitrary mixtures of modes at any frequency of operation, allowing for the integration of several phononic and photonic devices.

4.1.5 Methods

4.1.5.1 Summary of techniques

Mode tracking

If the modes are indexed by frequency for a long wavelength (or small wavenumber), we are interested in tracking the frequency $\omega^{(n)}(k)$ of the n^{th} mode with increasing wavenumber k, $n = 1, \ldots, d$, where d is the dimension of stiffness or mass matrix in eq. (4.1). Along $\mathcal{B}$, we discretize the wavenumbers as $k^{(i)}$, $i = 1, \ldots, N$, where N is the total number of discrete wavenumbers. Let the frequency associated with the n^{th} mode at the smallest wavenumber $k^{(1)}$ be $\omega^{(n)}(k^{(1)})$, and its corresponding eigenvector/mode shape be $\underset{\sim}{u}^{(n)}(k^{(1)})$. For any other wavenumber $k^{(i)}$ along $\mathcal{B}$, let the frequency and mode shape corresponding to this mode be $\omega^{(n)}(k^{(i)})$ and $\underset{\sim}{u}^{(n)}(k^{(i)})$, respectively. Then from eq. (4.1), we have

$$\underset{\sim}{K}(k^{(i)})\underset{\sim}{u}^{(n)}(k^{(i)}) = \omega^{(n)}(k^{(i)})^2 \underset{\sim}{M}(k^{(i)})\underset{\sim}{u}^{(n)}(k^{(i)}), \tag{4.2}$$

for this n^{th} mode indexed by frequency at $k^{(1)}$.

The principle behind our mode tracking (algorithm in Appendix), is to estimate the values of

$\underset{\sim}{u}^{(n)}(k^{(i+1)})$, $\omega^{(n)}(k^{(i+1)})$ and $\dfrac{\partial\omega^{(n)}}{\partial k}(k^{(i+1)})$ given $\omega^{(n)}(k^{(i)})$ and $\underset{\sim}{u}^{(n)}(k^{(i)})$.

$$\underset{\sim}{u}^{(n)}(k^{(i+1)}) \approx \underset{\sim}{u}^{(n)}(k^{(i)}) + \left.\frac{\partial \underset{\sim}{u}^{(n)}}{\partial k}\right|_{k^{(i)}} (k^{(i+1)} - k^{(i)}), \tag{4.3}$$

$$\omega^{(n)}(k^{(i+1)}) \approx \omega^{(n)}(k^{(i)}) + \left.\frac{\partial \omega^{(n)}}{\partial k}\right|_{k^{(i)}} (k^{(i+1)} - k^{(i)}) + \frac{1}{2}\left.\frac{\partial^2 \omega^{(n)}}{\partial k^2}\right|_{k^{(i)}} (k^{(i+1)} - k^{(i)})^2, \tag{4.4}$$

$$\frac{\partial\omega^{(n)}}{\partial k}(k^{(i+1)}) \approx \frac{\partial\omega^{(n)}}{\partial k}(k^{(i)}) + \left.\frac{\partial^2 \omega^{(n)}}{\partial k^2}\right|_{k^{(i)}} (k^{(i+1)} - k^{(i)}). \tag{4.5}$$

We take these estimated values of mode shape, frequency, and group velocity at wavenumber $k^{(i+1)}$ and compare them to the eigenvectors, frequencies, and group velocities from solving eq. (4.1) at $k = k^{(i+1)}$, to correctly classify the n^{th} mode at wavenumber $k^{(i+1)}$. A method to calculate the sensitives $\dfrac{\partial \underset{\sim}{u}^{(n)}}{\partial k}$ and $\dfrac{\partial^2\omega^{(n)}}{\partial k^2}$ analytically is detailed in Appendix. Calculation of these sensitivities and hence eq. (4.3), (4.4), and (4.5) allows us to take large wavenumber steps ($k^{(i+1)} - k^{(i)}$) while tracking a mode of interest. The algorithm in Appendix allows us to automate the process of tracking any mode starting from low wavenumber to the end of $\mathcal{B}$.

Optimal design of band gap

We are interested in calculating the slenderness ratios of the bars in a unit cell such that the frequency of interest ω_0 lies away from a band edge, while still improving the width of the band gap. Let the cross-sectional areas of the struts be represented by χ_j, $j = 1, \ldots, m$, where m is the number of struts in an octant describing the cubic symmetric unit cell. Suppose the band gap exists between the l^{th} and n^{th} modes, we formulate the problem

$$\begin{aligned} &\underset{\underset{\sim}{\chi}\in\mathcal{D}}{\arg\max} \quad \delta_1 \left(\omega_0 - \Omega^{(l)}_{\max}\right)^2 + \delta_2 \left(\omega_0 - \Omega^{(n)}_{\min}\right)^2 \\ &\text{s.t.} \quad \Omega^{(l)}_{\max} \le \omega_0 \le \Omega^{(n)}_{\min}, \end{aligned} \tag{4.6}$$

where $\Omega^{(l)}_{\max} = \max_i \omega^{(l)}(k^{(i)})$, $\Omega^{(n)}_{\min} = \min_i \omega^{(n)}(k^{(i)})$, and $\mathcal{D}$ is the set of allowable values for $\underset{\sim}{\chi}$. The ratio between non-negative weights δ_1 and δ_2 can be chosen to achieve a target separation of ω_0 from individual band edges. We choose a ratio of 1. We solve (4.6) using a descent method, with sensitivities discussed in Appendix.

Bounds on wave speeds and band gaps

The band gap between the l^{th} and n^{th} mode can be calculated as

$$O_1 = \Omega^{(n)}_{\min} - \Omega^{(l)}_{\max}. \tag{4.7}$$

Note that the accuracy of eq. (4.7) to estimate the bang gap is better with a finer discretization of the wavenumber. The wave speed for the p^{th} mode at a frequency ω_0 is [56]

$$O_2 = \left.\frac{\partial \omega^{(p)}}{\partial k}\right|_{k^{(p^*)}}, \text{ s.t. } \det(\underset{\sim}{K}(k^{(p^*)}) - \omega_0^2 \underset{\sim}{M}(k^{(p^*)})) = 0. \tag{4.8}$$

We calculate $k^{(p^*)}$ by finely dividing $\mathcal{B}$ around the wavenumber close to ω_0 for the p^{th} mode (see algorithm in Appendix). To calculate the bounds on attainable values as shown in Fig. 4.2(c),(d), for each lattice we define the objective $O = \gamma_1 O_1 + \gamma_2 O_2$. γ_1 and γ_2 are scalars between -1 and 1. We calculate the maximum value of O for several combinations of γ_1 and γ_2 while varying the cross-sectional areas of bars $\underset{\sim}{\chi}$ using a descent algorithm, with the sensitivities calculated in Appendix. Each maximum value gives us a half space that bounds the attainable values on the band gap and wave speed. Intersection of several such half spaces gives us the convex envelope of the attainable region (shaded regions in Fig. 4.2(c),(d)). In order to engineer target band gaps O_1^{target} or target wave speeds O_2^{target}, we would minimize the objectives $|O_1 - O_1^{\text{target}}|$ or $|O_2 - O_2^{\text{target}}|$, respectively.

Sample fabrication and experimental setup

We 3-D print our lattices using a selective laser sintering process, which gives us a homogenous distribution of material properties in each strut. The material properties of the base material used for 3-D printing (EOS polyamide PA 2200) are, Young's modulus $E = 1.7$ GPa, density $\rho = 930\,\text{kg/m}^3$, and Poisson's ratio $\nu = 0.35$ [1, 56]. The layout of the experimental setup in sketched in Fig. 4.3(b). The input wave packet information from the signal generator (Agilent 33220A) is communicated to a piezoelectric transducer (Panametrics V1011) after amplification via the piezoelectric amplifier (Piezomechanik LE 150/100 EBW). Due to the wedge mechanism, the longitudinal excitation from the transducer excites the samples at the base at an angle, i.e. a combination of longitudinal and shear waves. We measure the response at desired points using a laser doppler vibrometer (LDV, Polytec OFV-5000) and read the output signal (amplitude vs time) on the oscilloscope (Tektronix DPO3014).

Experimental measurements

For frequency transmission measurements and dispersion reconstruction, the input signal (amplitude vs time) is a burst signal with 1 cycle and has a broad frequency spread centered around the frequency of interest (Fig. S3(a)). To measure the frequency transmission, we first take the discrete Fourier transform (DFT) of the input (at the base of a lattice) and output (at the top unit cell) signals to get the amplitude associated with each frequency. We then take the ratio of amplitudes of each

frequency at the output to the input to get the frequency transmission. We cap the values at large enough transmission in both cases, to avoid analyzing resonant peaks. Note that the shear band gap region in lattice A numerically shows zero transmission whereas in experiments shows a small amplitude. We believe this is due to the slender nature of the structure causing flexural motion. To reconstruct the dispersion curve, we measure the output at 10 equidistant points (one in each unit cell) for a lattice. To reconstruct the longitudinal modes, we measure the output at the body center and for the shear modes, we measure the response at the edge center (orange and blue dots in Fig. 4.3(a), respectively). From the DFT of the output signals along the length of the sample, we get the dominant frequencies at each wavenumber [56]. To measure the wave speed, the input is a burst signal with 4 cycles and has a frequency spectrum that is narrow around the frequency of interest (Fig. S3). We calculate the wave speed from the time taken by the input signal to traverse through each lattice, i.e. from the middle of the first unit cell to the middle of the last unit cell. Due to the presence of boundary reflections, it is difficult to locate the centroid of the wave packet at the output. Hence, we measure time taken for the first peak in the signal to traverse through the lattice (Fig. S3(b)). This is reasonable as the group and phase velocities are almost identical (Fig. 4.2(a),(b)).

4.1.5.2 Sensitivity analysis

Let the band gap exist between the l^{th} and n^{th} modes, and we are interested in the wave speed of the p^{th} mode, where all modes are indexed by frequency at the lowest wavenumber along the Brillouin zone. In order to optimally design a band gap, wave speed, or calculate bounds on band gaps and wave speeds (see Methods) using a gradient descent algorithm, we require the gradients of $\Omega^{(l)}_{\max}$, $\Omega^{(n)}_{\min}$, and O_2 (wave speed) with respect to the cross-sectional areas of the struts χ_j, $j = 1, \ldots, m$. m is the number of struts in an octant describing the cubic symmetric unit cell. We have that $\Omega^{(l)}_{\max} = \max_i \omega^{(l)}(k^{(i)})$, $\Omega^{(n)}_{\min} = \min_i \omega^{(n)}(k^{(i)})$, and $O_2 = \left.\dfrac{\partial \omega^{(p)}}{\partial k}\right|_{k^{(p^*)}}$, s.t. $\det(\underset{\sim}{K}(k^{(p^*)}) - \omega_0^2 \underset{\sim}{M}(k^{(p^*)})) = 0$, where $i = 1, \ldots, N$ index the discrete wave numbers along the Brillouin zone. Let $l^* = \arg\max_i \omega^{(l)}(k^{(i)})$ and $n^* = \arg\min_i \omega^{(n)}(k^{(i)})$.

$$\frac{d\Omega^{(l)}_{\max}}{d\chi_j} = \frac{\partial \Omega^{(l)}_{\max}}{\partial \chi_j} + \left.\frac{\partial \Omega^{(l)}_{\max}}{\partial k}\right|_{k^{(l^*)}} \frac{\partial k^{(l^*)}}{\partial \chi_j}. \tag{4.9}$$

The eigenvalue problem can be written as

$$\left(\underset{\sim}{K}(k^{(l^*)}(\chi_j), \chi_j) - \Omega^{(l)}_{\max}(k^{(l^*)}(\chi_j), \chi_j)^2 \underset{\sim}{M}(k^{(l^*)}(\chi_j), \chi_j)\right) \underset{\sim}{u}^{(l)}(k^{(l^*)}(\chi_j), \chi_j) = 0. \tag{4.10}$$

Partial derivatives of eq. (4.10) with respect to χ_j and k give us

$$\frac{\partial \Omega_{\max}^{(l)}}{\partial \chi_j} = \underset{\sim}{u}^{(l)} . \left(\frac{\partial \underset{\sim}{K}}{\partial \chi_j} - {\Omega_{\max}^{(l)}}^2 \frac{\partial \underset{\sim}{M}}{\partial \chi_j} \right) \underset{\sim}{u}^{(l)},$$
$$\left. \frac{\partial \Omega_{\max}^{(l)}}{\partial k} \right|_{k^{(l^*)}} = \underset{\sim}{u}^{(l)} . \left(\left. \frac{\partial \underset{\sim}{K}}{\partial k} \right|_{k^{(l^*)}} - {\Omega_{\max}^{(l)}}^2 \left. \frac{\partial \underset{\sim}{M}}{\partial k} \right|_{k^{(l^*)}} \right) \underset{\sim}{u}^{(l)}. \tag{4.11}$$

Taking the total derivative of eq. (4.10) with respect to χ_j, we get

$$\frac{\partial k^{(l^*)}}{\partial \chi_j} = -\frac{\underset{\sim}{y}_1 \cdot \underset{\sim}{y}_2}{\underset{\sim}{y}_2 \cdot \underset{\sim}{y}_2}, \tag{4.12}$$

where

$$\underset{\sim}{y}_1 = \left(\frac{\partial \underset{\sim}{K}}{\partial \chi_j} - {\Omega_{\max}^{(l)}}^2 \frac{\partial \underset{\sim}{M}}{\partial \chi_j} - 2\Omega_{\max}^{(l)} \frac{\partial \Omega_{\max}^{(l)}}{\partial \chi_j} \underset{\sim}{M} \right) \underset{\sim}{u}^{(l)} + \left(\underset{\sim}{K} - {\Omega_{\max}^{(l)}}^2 \underset{\sim}{M} \right) \frac{\partial \underset{\sim}{u}^{(l)}}{\partial \chi_j},$$
$$\underset{\sim}{y}_2 = \left(\left. \frac{\partial \underset{\sim}{K}}{\partial k} \right|_{k^{(l^*)}} - {\Omega_{\max}^{(l)}}^2 \left. \frac{\partial \underset{\sim}{M}}{\partial k} \right|_{k^{(l^*)}} - 2\Omega_{\max}^{(l)} \left. \frac{\partial \Omega_{\max}^{(l)}}{\partial k} \right|_{k^{(l^*)}} \underset{\sim}{M} \right) \underset{\sim}{u}^{(l)} + \left(\underset{\sim}{K} - {\Omega_{\max}^{(l)}}^2 \underset{\sim}{M} \right) \left. \frac{\partial \underset{\sim}{u}^{(l)}}{\partial k} \right|_{k^{(l^*)}}.$$

Substituting eq. (4.11) and (4.12) in eq.(4.9), we get the sensitivities of $\Omega_{\max}^{(l)}$ with respect to the cross-sectional areas of the struts χ_j. The sensitivities $\dfrac{d\Omega_{\min}^{(n)}}{d\chi_j}$ are calculated in a similar manner to the above.

$$\frac{dO_2}{d\chi_j} = \left. \frac{\partial^2 \omega^{(p)}}{\partial \chi_j \partial k} \right|_{k^{(p^*)}} + \left. \frac{\partial^2 \omega^{(p)}}{\partial k^2} \right|_{k^{(p^*)}} \frac{\partial k^{(p^*)}}{\partial \chi_j}. \tag{4.13}$$

The partial derivatives in eq. (4.13) can be calculated as [56]

$$\frac{\partial^2 \omega^{(p)}}{\partial \chi_j \partial k} = \frac{1}{2\omega^{(p)}} \left(2\,\mathrm{Re} \left(\frac{\partial \underset{\sim}{u}^{(p)}}{\partial \chi_j} \cdot \left(\frac{\partial \underset{\sim}{K}}{\partial k} - {\omega^{(p)}}^2 \frac{\partial \underset{\sim}{M}}{\partial k} \right) \underset{\sim}{u}^{(p)} \right) + \right.$$
$$\left. \underset{\sim}{u}^{(p)} \cdot \left(\frac{\partial^2 \underset{\sim}{K}}{\partial \chi_j \partial k} - {\omega^{(p)}}^2 \frac{\partial^2 \underset{\sim}{M}}{\partial \chi_j \partial k} - 2\omega^{(p)} \frac{\partial \omega^{(p)}}{\partial \chi_j} \frac{\partial \underset{\sim}{M}}{\partial k} \right) \underset{\sim}{u}^{(p)} - \frac{\frac{\partial \omega^{(p)}}{\partial \chi_j}}{\omega^{(p)}} \underset{\sim}{u}^{(p)} . \left(\frac{\partial \underset{\sim}{K}}{\partial k} - {\omega^{(p)}}^2 \frac{\partial \underset{\sim}{M}}{\partial k} \right) \underset{\sim}{u}^{(p)} \right). \tag{4.14}$$

where Re(.) is the real part of an entity. Similarly,

$$\frac{\partial^2 \omega^{(p)}}{\partial k^2} = \frac{1}{2\omega^{(p)}} \left(2\,\mathrm{Re} \left(\frac{\partial \underset{\sim}{u}^{(p)}}{\partial k} \cdot \left(\frac{\partial \underset{\sim}{K}}{\partial k} - {\omega^{(p)}}^2 \frac{\partial \underset{\sim}{M}}{\partial k} \right) \underset{\sim}{u}^{(p)} \right) + \right.$$
$$\left. \underset{\sim}{u}^{(p)} \cdot \left(\frac{\partial^2 \underset{\sim}{K}}{\partial k^2} - {\omega^{(p)}}^2 \frac{\partial^2 \underset{\sim}{M}}{\partial k^2} - 2\omega^{(p)} \frac{\partial \omega^{(p)}}{\partial k} \frac{\partial \underset{\sim}{M}}{\partial k} \right) \underset{\sim}{u}^{(p)} - \frac{\frac{\partial \omega^{(p)}}{\partial k}}{\omega^{(p)}} \underset{\sim}{u}^{(p)} . \left(\frac{\partial \underset{\sim}{K}}{\partial k} - {\omega^{(p)}}^2 \frac{\partial \underset{\sim}{M}}{\partial k} \right) \underset{\sim}{u}^{(p)} \right). \tag{4.15}$$

From the total derivative of the fixed frequency condition $\omega^{(p)}\left(k^{(p^*)}(\chi_j),\chi_j\right)=\omega_0$ with respect to χ_j, we get

$$\frac{\partial k^{(p^*)}}{\partial \chi_j}=-\frac{\dfrac{\partial \omega^{(p)}}{\partial \chi_j}}{\dfrac{\partial \omega^{(p)}}{\partial k}}=-\left.\frac{\underset{\sim}{u}^{(p)}.\left(\frac{\partial \underset{\sim}{K}}{\partial \chi_j}-\omega^{(p)2}\frac{\partial \underset{\sim}{M}}{\partial \chi_j}\right)\underset{\sim}{u}^{(p)}}{\underset{\sim}{u}^{(p)}.\left(\frac{\partial \underset{\sim}{K}}{\partial k}-\omega^{(p)2}\frac{\partial \underset{\sim}{M}}{\partial k}\right)\underset{\sim}{u}^{(p)}}\right|_{k^{(p^*)}}. \tag{4.16}$$

Substituting eq. (4.14), (4.15) and (4.16) in eq.(4.13), we get the sensitivities of the wave speed O_2 with respect to the cross-sectional areas of the struts χ_j.

For calculation of sensitivities of the eigenvector, $\dfrac{\partial \underset{\sim}{u}}{\partial \chi_j}$ and $\dfrac{\partial \underset{\sim}{u}}{\partial k}$ in equations (4.12), (4.14), and (4.15) we use the analysis carried out in [56].

Their formulation states that for an eigenvalue problem of the form

$$\left(\underset{\sim}{K}(k(\chi_j),\chi_j)-\omega(k(\chi_j),\chi_j)^2\underset{\sim}{M}(k(\chi_j),\chi_j)\right)\underset{\sim}{u}(k(\chi_j),\chi_j)=0, \tag{4.17}$$

and $\alpha=k$ or χ_j, the sensitivities $\dfrac{\partial \underset{\sim}{u}}{\partial \alpha}$ can be calculated from the null-space of the matrix

$$\begin{pmatrix} 0 & \left(\left(\underset{\sim}{M}^R+\underset{\sim}{M}^I\right)\underset{\sim}{u}^R\right)^T & \left(\left(\underset{\sim}{M}^R+\underset{\sim}{M}^I\right)\underset{\sim}{u}^I\right)^T \\ -b_1 & \underset{\sim}{A}^R & -\underset{\sim}{A}^I \\ -b_2 & \underset{\sim}{A}^I & \underset{\sim}{A}^R \end{pmatrix}, \tag{4.18}$$

where superscripts R and I denoted the real and imaginary parts of quantities, where

$$\begin{aligned} &\underset{\sim}{A}=\underset{\sim}{K}-\omega^2\underset{\sim}{M},\\ &\underset{\sim}{A}^R\underset{\sim}{u}_\alpha{}^R-\underset{\sim}{A}^I\underset{\sim}{u}_\alpha{}^I=\underset{\sim}{A}^I_\alpha\underset{\sim}{u}^I-\underset{\sim}{A}^R_\alpha\underset{\sim}{u}^R=:b_1,\\ &\underset{\sim}{A}^R\underset{\sim}{u}_\alpha{}^I+\underset{\sim}{A}^I\underset{\sim}{u}_\alpha{}^R=-\underset{\sim}{A}^I_\alpha\underset{\sim}{u}^R-\underset{\sim}{A}^R_\alpha\underset{\sim}{u}^I=:b_2. \end{aligned}$$

In [56], the authors show that for eigenvalues with single multiplicity, the null space of (4.18) has exactly two vectors $\underset{\sim}{y}_1$ and $\underset{\sim}{y}_2$. If however the multiplicity is more than 1, we can always perturb our wavenumber infinitesimally such that the eigenvalue has single multiplicity on the mode of interest. The real and imaginary parts of $\dfrac{\partial \underset{\sim}{u}}{\partial \alpha}$ and hence the sensitivity of the eigenvector can be calculated from

$$\begin{pmatrix} 0 \\ \dfrac{\partial \underset{\sim}{u}}{\partial \alpha}^R \\ \dfrac{\partial \underset{\sim}{u}}{\partial \alpha}^I \end{pmatrix}=\beta_1\underset{\sim}{y}_1+\beta_2\underset{\sim}{y}_2-\begin{pmatrix} 1 \\ -(c_1+c_2)\underset{\sim}{u}^R \\ -(c_1+c_2)\underset{\sim}{u}^I \end{pmatrix}. \tag{4.19}$$

The values of β_1 and β_2 can be calculated from the equation that sets the first element on the right hand side of eq. (4.19) to 0, and one of the following equations,

$$\frac{\partial \underset{\sim}{u}^R}{\partial \alpha} \cdot \left(\underset{\sim}{M}^R \underset{\sim}{u}^R \right) + \frac{\partial \underset{\sim}{u}^I}{\partial \alpha} \cdot \left(\underset{\sim}{M}^R \underset{\sim}{u}^I \right) = -\frac{1}{2} \left(\underset{\sim}{u}^R . \frac{\partial \underset{\sim}{M}^R}{\partial \alpha} \underset{\sim}{u}^R + \underset{\sim}{u}^I . \frac{\partial \underset{\sim}{M}^R}{\partial \alpha} \underset{\sim}{u}^I \right) =: c_1,$$
$$\frac{\partial \underset{\sim}{u}^R}{\partial \alpha} \cdot \left(\underset{\sim}{M}^I \underset{\sim}{u}^R \right) + \frac{\partial \underset{\sim}{u}^I}{\partial \alpha} \cdot \left(\underset{\sim}{M}^I \underset{\sim}{u}^I \right) = -\frac{1}{2} \left(\underset{\sim}{u}^R . \frac{\partial \underset{\sim}{M}^I}{\partial \alpha} \underset{\sim}{u}^R + \underset{\sim}{u}^I . \frac{\partial \underset{\sim}{M}^I}{\partial \alpha} \underset{\sim}{u}^I \right) =: c_2.$$

Now that we can calculate the sensitivities of $\Omega_{\max}^{(l)}$, $\Omega_{\min}^{(n)}$, and O_2, with respect to the cross-sectional areas of the struts χ_j for a given lattice, we can use a gradient descent method to optimally design a band gap, wave speed, or calculate bounds on band gaps and wave speeds.

As detailed in Methods, tracking the n^{th} mode (Algorithm 5), we require the sensitivities $\frac{\partial \omega^{(n)}}{\partial k}$, $\frac{\partial \underset{\sim}{u}^{(n)}}{\partial k}$, and $\frac{\partial^2 \omega^{(n)}}{\partial k^2}$ described above.

4.1.5.3 Cubic symmetric lattices

As noted in this chapter, we non-dimensionalize our analysis for lattices. Starting from the eigenvalue problem, we divide every length dimension by L (the lattice vector length/unit cell length), every mass dimension by ρL^3 and every time dimension by $\sqrt{\frac{\rho}{E}} L$. Here, ρ and E are the density and Young's modulus of the base material used to make the lattice. In a unit cell, we fix the quantities L, ρ, and E as described in the section. However, we can scale any quantity according to its dimensions, as these parameters change.

In a cubic symmetric unit cell, there is one repeating octant (indicated by the yellow cube in Fig. 4.5(a)). In order to generate the unit cell given the connectivity within the octant, we first take a reflection of the contents in this octant about the plane containing vertices labeled 2, 4, 6, 8 (keeping the old contents). Then we reflect the resulting structure about the plane containing vertices 1, 2, 5, 6 (keeping the old contents). Finally, we reflect the current structure about the plane containing vertices 1, 2, 3, 4 while keeping all the old contents.

In order to generate a large database of connectivities in an octant, we devise an algorithm shown in Fig. 4.5(b) implemented in the MATLAB code provided as data. Within an octant, we list all possible combinations of vertices (from 1 to 8) such that there is at least one vertex on each face of the octant. For each set in this list, we consider Delaunay triangulations of those vertices and connect the vertices with an edge, which represents a strut. We perform this triangulation and calculate all strongly connected subsets in each triangulation, for every single element in the list containing sets of vertices with at least one on each face of the octant. Note that in a strongly connected set of vertices and edges, we can draw a path connecting any two vertices along the

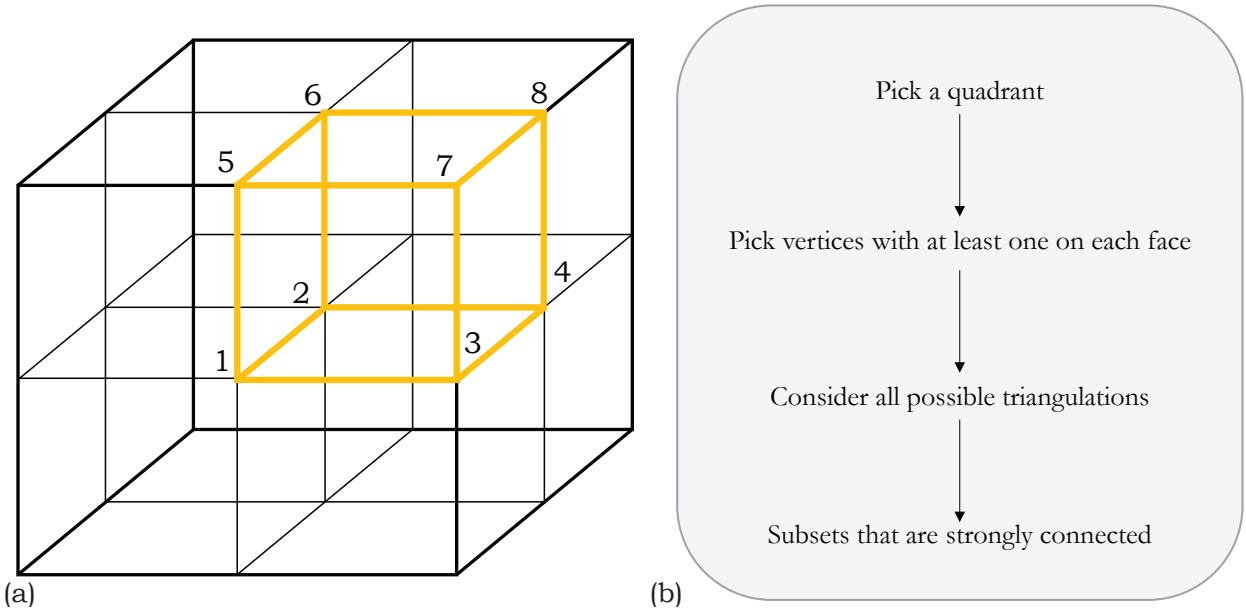

Figure 4.5: Cubic symmetric unit cell: ***(a)*** *The octant (highlighted in yellow) contains the repeating element of the cubic symmetric unit cell.* ***(b)*** *The algorithm used to generate a large database of such unit cells.*

edges. We fix the slenderness ratio of each strut (ratio of length to diameter) as 10. We then calculate the structure of the unit cell for every unique structure in an octant through reflections as described above. This exercise yields 815,550 total geometries for the unit cell. We also provide an option to calculate the geometries for a more populated octant with a larger number of vertices in our MATLAB code.

The condition where we pick vertices such that there is at least one on each face of the octant ensures compatibility of the resulting unit cell after taking the reflections as described. We consider a triangulation of each set of vertices so that we avoid any intersecting bars in an octant. Finally, the condition on each subset of the triangulation being strongly connected is sufficient to ensure that we avoid structures in which the struts are freely dangling. Hence, we ensure that the resulting unit cells are always structurally stable and free of intersecting bars in an octant.

4.1.5.4 Mode tracking

The mode tracking algorithm (Algorithm 5) uses the sensitivities derived earlier in this section to follow any mode of choice for an arbitrary structure on the dispersion curve. We use this algorithm on several lattices with cubic symmetric unit cells (generated by the algorithm in Fig. 4.5(b)) repeating in one direction. We model each strut in a unit cell using three 1-D frame finite elements, where a node associated with an element has 6 degrees of freedom (three translational and three

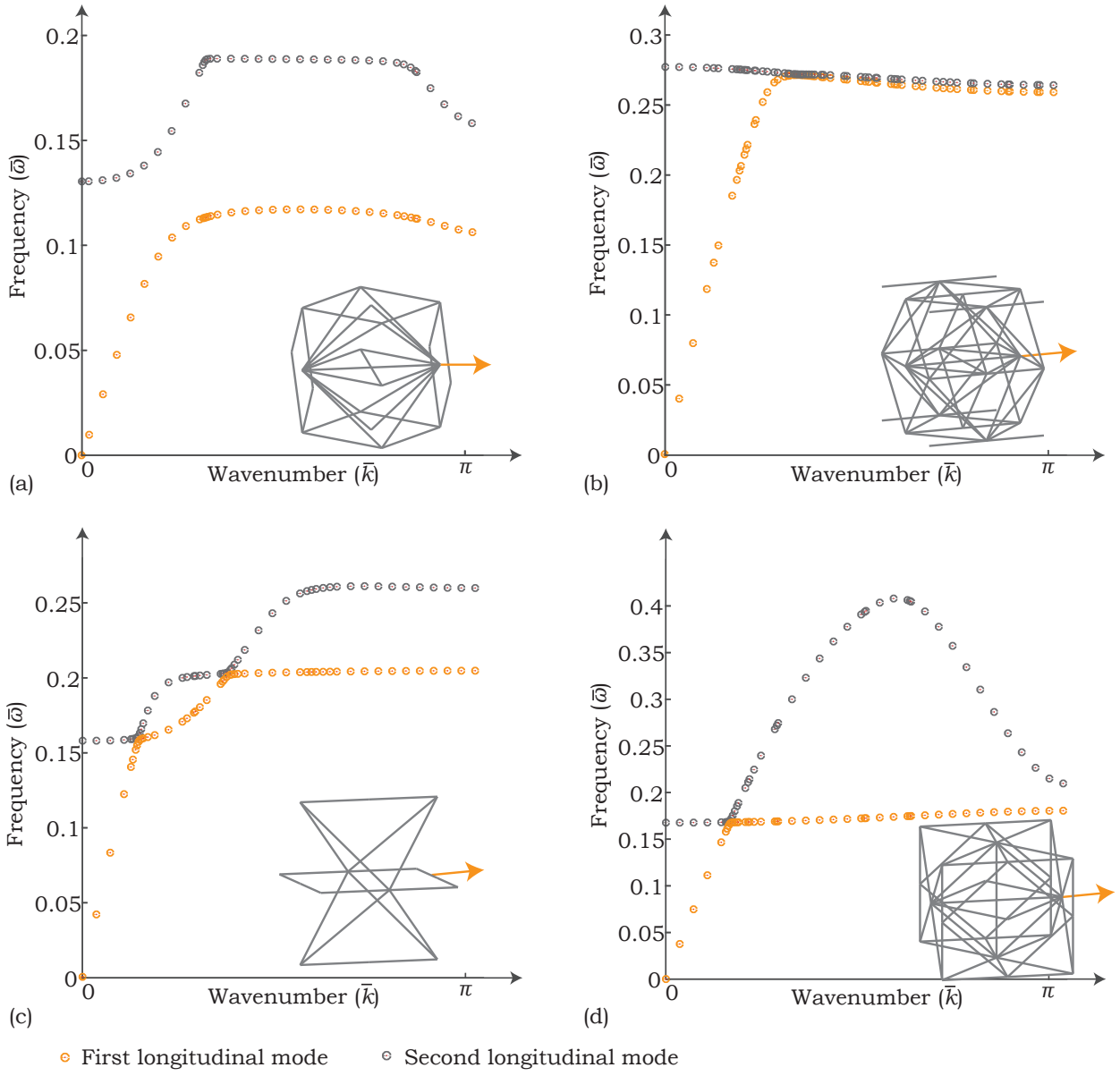

Figure 4.6: Mode tracking: ***(a)-(d)*** *Four examples showing the mode tracking algorithm (Algorithm 5) used to track the first two longitudinal modes. Orange arrows indicate direction of periodicity.*

rotational). Details of such a model with a convergence study can be found in [56]. Examples of the algorithm tracking the first two longitudinal modes is shown in Fig. 4.6.

As mentioned earlier, we non-dimensionalize our analysis, and plot the dispersion curves between non-dimensional angular frequency $\overline{\omega}$ and non-dimensional wavenumber $\overline{k}$. Notice that the algorithm takes larger steps along the wavenumber in regions of the curve that are linear ($\overline{\omega}$ vs $\overline{k}$). The first derivative approximation of the eigenvector is accurate and sufficient in such regions. In regions of the dispersion curve where there are sharp bends or intersection of curves, the algorithm

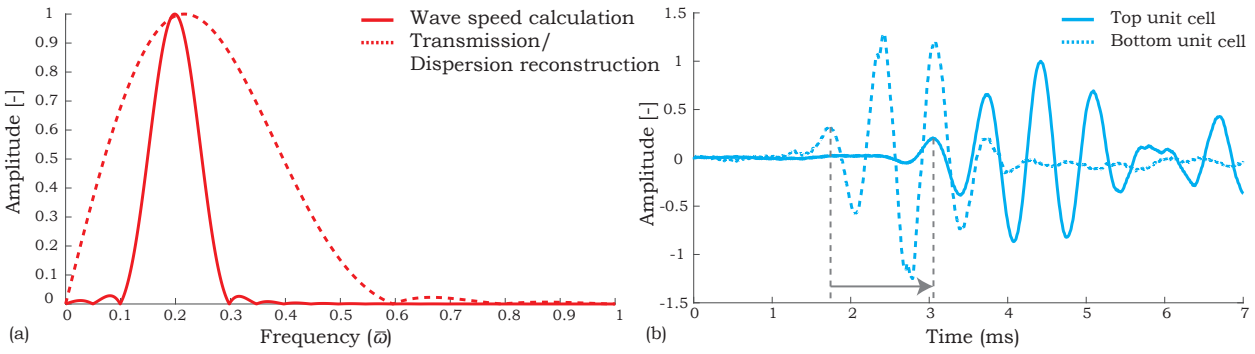

Figure 4.7: Excitation: ***(a)****Frequency response of input signals used for wave speed calculations, frequency transmission measurements, and dispersion reconstruction.* ***(b)*** *Time taken by the wave to travel from the first to last unit cell in lattice B indicated by the arrow.*

automatically takes finer steps to classify the modes correctly, and comparing the estimated eigenvalues and group velocities (Methods) to the actual values becomes important. Hence, we are efficient in the sense that we track the dispersion curve correctly associated with a mode of choice with fewer number of evaluations of the eigenvalue problem than is done traditionally. The implementation details of this algorithm can be found in the MATLAB code provided. Note that the accuracy of classification in Algorithm 5 depends on parameters δ and β, which determine the minimum step size in wavenumber and a threshold level of acceptable similarity between estimated and actual eigenvectors. Hence, reducing δ and increasing β increases the accuracy of the algorithm. In our work, we focus on tracking specific modes (longitudinal and shear). We achieve this by evaluating the mode shapes associated with points on the dispersion curve at low wavenumbers, and then track the ones that are either longitudinal or shear over the path along $\mathcal{B}$.

4.1.5.5 Experiments and numerics

For measuring frequency transmission and dispersion reconstruction, we send an input signal through the lattice that is a single cycle burst signal. The frequency response from the DFT of that signal has a spread as shown by the dotted curve in Fig. 4.7(a). In order to measure the wave speed at a particular frequency $\overline{\omega}_0 = 0.2$ (1435 Hz), we use a burst input signal with 4 cycles (Fig. 4.7(b)) that has a much narrower spread of frequencies around $\overline{\omega}_0$ (solid curve in Fig. 4.7(a)). As mentioned in Methods, we calculate the wave speed from the time taken by the input signal to traverse through the lattice. The arrow in Fig. 4.7(b) indicates this time calculated from the first peaks in the signals at the first and last unit cells, for a measurement in lattice B. Notice that we normalize the amplitudes in Fig. 4.7 by a maximum amplitude on the plots. For wave speed calculations in each lattice, we take the average of five measurements across two samples in each.

The mode shapes of propagating modes in each of the infinite periodic lattices is indicated qualitat-

ively on the respective unit cells in Fig. 4.8(a),(b) modeled in COMSOL using 3-D solid elements (for better visualization). The wire figures indicate original positions of unit cells and the solid figures indicate deformed positions. In Fig. 4.8(a) (lattice A), there is a clear translation of the body center along the longitudinal direction (orange arrow). In lattice B, there is a displacement of the edge center in the shear direction (blue arrow) as seen in 4.8(b).

We also perform simulations on the lattices that contain a finite number of unit cells to better compare the results from experiments. As seen in Fig. 4.8(c), each lattice (A and B) has 10 unit cells, in which each strut is modeled as a combination of 3 discrete frame elements. Let the assembled non-dimensional stiffness and mass matrices for a lattice be $\overline{\underset{\sim}{K}}$ and $\overline{\underset{\sim}{M}}$, respectively [56].

$$(\overline{\underset{\sim}{K}} - \overline{\omega}^2 \overline{\underset{\sim}{M}})\overline{\underset{\sim}{U}} = 0. \tag{4.20}$$

$\overline{\underset{\sim}{U}}$ represents the global vector of non-dimensional displacements at the nodes of the lattice. We apply a time varying (harmonic) displacement boundary condition to the nodes at the base of each unit cell, that is a combination of displacements in the longitudinal (orange arrows) and shear directions (blue arrows) to simulate experiments. We vary the non-dimensional frequency of the displacement boundary condition across a range of frequencies ($\overline{\omega}$ = 0.05 to 0.35) and measure the amplitude of non-dimensional displacements at the last unit cell, from the unknown quantities in $\overline{\underset{\sim}{U}}$ obtained by solving eq. (4.20). We measure longitudinal displacements at the body center (orange dots) along the orange arrows and the shear displacements at the edge center (blue dots) along the blue arrows.

For a given frequency $\overline{\omega}$, the ratio of amplitudes of displacement at the top unit cell to the base gives us the transmission of that frequency. The results of frequency transmission across a range shows a shear band gap in lattice A and a longitudinal band gap in lattice B. Further, they show longitudinal waves propagating in lattice A and shear waves propagating through lattice B. These results agree well with experiments.

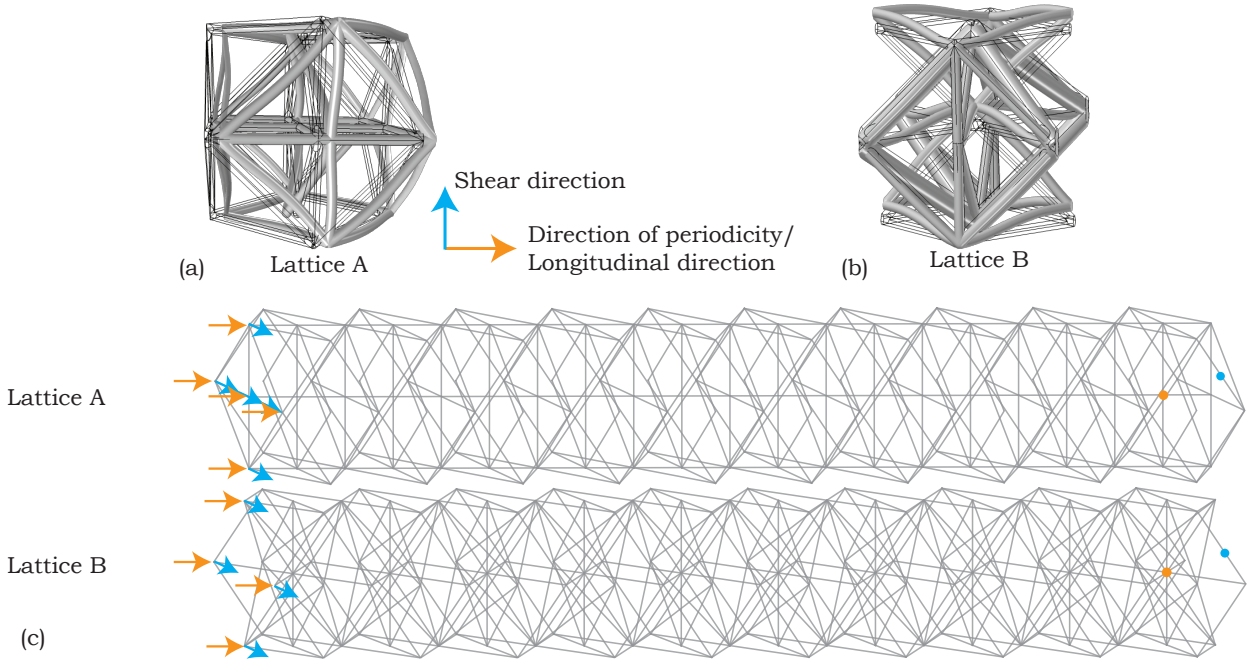

Figure 4.8: Mode shapes: ***(a)*** *Mode shapes qualitatively indicated in each unit cell show propagating longitudinal mode in lattice A and shear mode in lattice B.* ***(b)*** *Time varying harmonic loads applied at the base of finite lattices A and B with 10 unit cells each, modeled using frame elements.*

Algorithm 5 Tracking a mode with increasing wavenumber

Assign a value for γ (largest allowed increment in wavenumber)
Assign a value for β (threshold to classify a mode (set to a high value, say 15))
Assign a value for η (between 0 and 1)
Assign a value for δ (smallest allowed increment in wavenumber)
Assign a value for Γ (maximum value for wavenumber – end of path on $\mathcal{B}$)
Assign a value for n (index of mode being tracked (by frequency) at $k^{(1)}$)
Note: In the section, n is picked such that we track longitudinal/shear modes
$i = 1$
$k^{(i)} = \epsilon$ (small positive value, say 0.001)
$k_{track} = [\ ]$ (Wavenumbers at which the mode is tracked)
while $k^{(i)} \leq \Gamma$ **do**
    if $i = 1$ **then**
        Calculate $\underset{\sim}{w}$ (vector of frequencies sorted in ascending order at $k^{(i)}$) – using eq.(1)
        Calculate corresponding $\underset{\sim}{U}$ (matrix with columns as eigenvectors) – using eq.(1)
        $\omega_i^{(n)} = w_n$ and $\underset{\sim}{u_i}^{(n)} = U(:, n)$ (Frequency and mode shape of tracked mode)
        $dk = \gamma$
        Calculate $\underset{\sim}{u_{i+1}}^{(n),est}$, $\omega_{i+1}^{(n),est}$, $\left(\frac{\partial \omega^{(n),est}}{\partial k}\right)_{i+1}$ (estimate values at $k^{(i)} + dk$)
        $k^{(i+1)} = k^{(i)} + dk$
        $k_{track} = [k_{track}, k^{(i)}]$
        $i = i + 1$
    else
        Calculate $\underset{\sim}{w}$ and $\underset{\sim}{U}$ at $k^{(i)}$
        $\underset{\sim}{\theta}$= vector of sine of angles between $\underset{\sim}{u_i}^{(n),est}$ and each column in $\underset{\sim}{U}$
        Calculate $\underset{\sim}{\theta_s}$ ($\underset{\sim}{\theta}$ sorted in ascending order)
        if $\theta_{s,2}/\theta_{s,1} > \beta$ **then**
            check=1 (Mode classification does not need group velocity comparison)
        else
            $dk = \eta \times dk$
            check=0 (Mode classification needs group velocity comparison)
            while $dk \geq \delta$ and check=0 **do**
                Calculate $\underset{\sim}{u_i}^{(n),est}$, $\omega_i^{(n),est}$, $\left(\frac{\partial \omega^{(n),est}}{\partial k}\right)_i$ (estimate values at $k^{(i-1)} + dk$)
                Calculate $\underset{\sim}{w}$ and $\underset{\sim}{U}$ at $k^{(i-1)} + dk$
                $k^{(i)} = k^{(i-1)} + dk$
                Calculate $\underset{\sim}{\theta}$, $\underset{\sim}{\theta_s}$

if $\theta_{s,2}/\theta_{s,1} > \beta$ **then**
check=1
else
check=0
end
$dk = \eta \times dk$
end
$dk = dk/\eta$
end
if check=1 **then**
Calculate $\underset{\sim}{d_1}$ (Norm of difference between $\omega_i^{(n),est}$ and each element in $\underset{\sim}{w}$)
Calculate $\underset{\sim}{s} = \underset{\sim}{d_1} .* \underset{\sim}{\theta}$ (element wise product)
Calculate $\omega_i^{(n)}$ and $\underset{\sim}{u_i}^{(n)}$ using index of minimum value in $\underset{\sim}{s}$
$dk = \gamma$
Calculate $\underset{\sim}{u_{i+1}}^{(n),est}$, $\omega_{i+1}^{(n),est}$, $\left(\frac{\partial \omega^{(n),est}}{\partial k}\right)_{i+1}$ (estimate values at $k^{(i)} + dk$)
$k^{(i+1)} = k^{(i)} + dk$
$k_{track} = [k_{track}, k^{(i)}]$
$i = i + 1$
else
Calculate d_2 (Norm of difference between $\left(\frac{\partial \omega^{(n),est}}{\partial k}\right)_i$ and actual group velocities at $k^{(i)}$)
Calculate $\underset{\sim}{s} = \underset{\sim}{d_2} .* \underset{\sim}{\theta}$
Calculate $\omega_i^{(n)}$ and $\underset{\sim}{u_i}^{(n)}$ using index of minimum value in $\underset{\sim}{s}$
$dk = \gamma$
Calculate $\underset{\sim}{u_{i+1}}^{(n),est}$, $\omega_{i+1}^{(n),est}$, $\left(\frac{\partial \omega^{(n),est}}{\partial k}\right)_{i+1}$ (estimate values at $k^{(i)} + dk$)
$k^{(i+1)} = k^{(i)} + dk$
$k_{track} = [k_{track}, k^{(i)}]$
$i = i + 1$
end
end
end
Output 1- k_{track} (discrete wavenumbers at which the mode is tracked)
Output 2- $\omega_i^{(n)}$ (frequency at i^{th} wavenumber in k_{track}, of the tracked mode)
Output 3- $\underset{\sim}{u_i}^{(n)}$ (mode shape at i^{th} wavenumber in k_{track}, of the tracked mode)

Algorithm 6 Wavenumber $k^{(p^*)}$ associated with a fixed frequency ω_0 for the p^{th} mode

1: Track the p^{th} mode according to Algorithm 5 to obtain k_{track} and $\underset{\sim}{\omega}^{(n)}$.
2: Assign a value for Δ (more than 1)
3: Assign a value for δ (small positive value, say 0.001)
4: From $\underset{\sim}{\omega}^{(n)}$, identify the largest frequency smaller than ω_0 (ω_0^{lower}) and the smallest frequency larger than ω_0 (ω_0^{upper})
5: Identify from k_{track}, the wavenumbers associated with ω_0^{lower} and ω_0^{upper}. Let these be k^{lower} and k^{upper}, respectively
6: Divide the wavenumber region between k^{lower} and k^{upper} into Δ parts of width $w = (k^{upper} - k^{lower})/\Delta$
7: Set $k_{track} = [k_{lower}, k_{lower} + w, \ldots, k_{upper}]$
8: Evaluate the frequency by solving the eigenvalue problem (eq. (1)) at each wavenumber in k_{track} and assign as the new vector of frequencies $\underset{\sim}{\omega}^{(n)}$ (Use Algorithm 5 to track the frequencies associated with the n^{th} mode in this range)
9: Repeat steps 4-8 until $|\omega_0^{upper} - \omega_0^{lower}| < \delta$
10: Assign $k^{(p^*)} = (k^{upper} + k^{lower})/2$
11: Output – $k^{(p^*)}$ (Wavenumber associated with a fixed frequency for the p^{th} mode)

Chapter 5

ENGINEERING MULTI-STABLE SHAPE MORPHING

Research presented in this chapter has been adapted from the following publication:

Injeti, S. S., Daraio, C. & Bhattacharya, K. Multi-stable shape morphing. *In preparation* (2021).

5.1 Motivation

Multi-stable shape morphing allows for a number of applications from medical devices to deployable space structures where switching between rigid configurations with vastly different topologies is important. However, most designs are limited by bi-stability either at the macroscopic or unit cell level owing to the difficulty in engineering a highly non-linear energy landscape using just elements that display convex energy landscapes. In this work, we draw inspiration from protein folding and ion channel mechanisms, two key processes that regulate biological activity by manipulating contacts between amino acid residues. We apply the concept to a mechanical system by introducing rigid kinematic constraints simulating such contacts together with disengaging energy storing elements, to create multi-stability. We present the idea on a kagome lattice configuration, producing a quadri-stable unit cell and arbitrarily complex stable topologies with larger tessellations, validated by demonstrations on 3-D printed structures. Also, most designs that use passive actuation address one-way shape morphing along the direction of least resistance. We demonstrate reversible, thermally actuated shape morphing between stable open and closed topologies using shape memory springs. The designs can be extended to non-planar structures and fabricated at vastly different length scales.

5.2 The building block

In order to achieve several more stable states, we derive an idea from a biological self-assembly mechanism influenced by evolutionary selection, protein folding, which governs the configuration of a protein based on contact between amino acid residues. The left panel in Fig. 5.1(a) illustrates a protein as a strand of amino acid residues, showing weak (yellow arrows) and strong (pink arrows) contact between residues that are far away and close to each other, respectively [91]. A higher number of strong contacts minimizes the interaction potential energy in the system, resulting in a more stable configuration [37]. This idea is seen in the right panel in Fig. 5.1(a), where each amino acid residue is indicated by a bead. The structure starts from an unfolded configuration with minimum strong residue contacts and folds into a unique stable native structure with maximum number of strong contacts. In the process, the protein assumes several rich

intermediate configurations, each differing from the other by the set of residues in strong contact. In our work, we extend the concept to mechanical systems, where we utilize rigid kinematic constraints in a structure to engineer additional stable states at configurations identified by mechanical contact of surfaces. Further, conventional energy storing elements resist both tension and compression resulting in a strictly convex energy landscape, which limits the design of a non-convex energy landscape for a structure. We overcome this by utilizing *slack elements* (disengaging springs), that resist only tension and not compression.

We design a tri-stable switch (Fig. 5.1(b)) that is part of a kagome lattice configuration (Fig. 5.1(c)). It consists of two rigid equilateral triangles, connected by a pin-joint which is the origin in the inset. The configuration of the switch can be described by a single degree of freedom – the angle between the rigid triangles θ. The orthogonal axes are indicated by red and green arrows, and angles are measured counterclockwise from the axis indicated by the red arrow while the bottom triangle is fixed. The two slack elements with tensile stiffness k_j and rest lengths k_j^0, $j = 1, 2$, are indicated by dashed lines with end points marked by i, $i = 1, \ldots, 4$. Let the position vectors of an end point of a slack element be $\underset{\sim}{r}_i = (r_i \ \cos\theta_i, \ r_i \ \sin\theta_i)$, where r_i is the length of each position vector, $\theta_1 = \theta + \frac{\pi}{3}$, $\theta_2 = \theta + \pi$, $\theta_3 = \theta$, and $\theta_4 = 0$. The potential energy stored in the system at a configuration with angle θ can be calculated as

$$E(r_i, k_j, k_j^0, \theta) = k_1 f\left(|\underset{\sim}{r}_1(r_1, \theta) - \underset{\sim}{r}_2(r_2, \theta)| - k_1^0\right) + k_2 f\left(|\underset{\sim}{r}_3(r_3, \theta) - \underset{\sim}{r}_4(r_4, \theta)| - k_2^0\right), \quad (5.1)$$

where $k_j f(x) = \frac{1}{2} k_j \left(\frac{x(\tanh(x)+1)}{2}\right)^2$ calculates the energy per unit stiffness in a slack element for stretch x, illustrated by the inset in Fig. 5.1(b). Notice that $f(x) \approx 0$ when $x \leq 0$ and non-zero otherwise, indicating that the element resists tension and not compression. In order to engineer tri-stability, i.e. engineer local energy minima at the n^{th} configuration $\left(\text{indicated by } C_n \text{ in Fig. } 5.1(b) \text{ with degree of freedom } \theta = \theta^{(C_n)}\right)$, $n = 1, 2, 3$, we solve the problem

$$\begin{aligned} \underset{r_i, k_j, k_j^0}{\arg\min} \quad & \Phi_p\left(-\frac{\partial E}{\partial \theta}\right)_{\theta=\theta^{(C_1)}} + \left(\frac{\partial E}{\partial \theta}\right)^2_{\theta=\theta^{(C_2)}} + \Phi_p\left(\frac{\partial E}{\partial \theta}\right)_{\theta=\theta^{(C_3)}} \\ \text{subject to} \quad & 0 \leq r_i \leq L, \\ & k_j \geq 0, \ k_j^0 \geq 0, \end{aligned} \quad (5.2)$$

where $\theta^{(C_1)} = 0$, $\theta^{(C_2)} = \frac{2\pi}{3}$, $\theta^{(C_3)} = \frac{4\pi}{3}$, L is the side-length of a triangle, and $\Phi_p(y) = \frac{1}{p}\left(e^{py} - 1\right)$ is a penalty function [60] with large p (we take p=10 in our calculations). Notice that $\Phi_p(y) \approx 0$ when $x \leq 0$, and large otherwise, forcing the gradient of energy at configuration C_1 to be positive and configuration C_3 to be negative. The optimal values of problem (5.2), r_i^*, k_j^*, k_j^{0*} calculated using gradient descent, are not unique and can be picked according to fabricability. We take $r_i^* = 0.5L$, $k_j^{0*} = 0.78L$, and the stiffness values k_j^* can be arbitrary for identical slack elements.

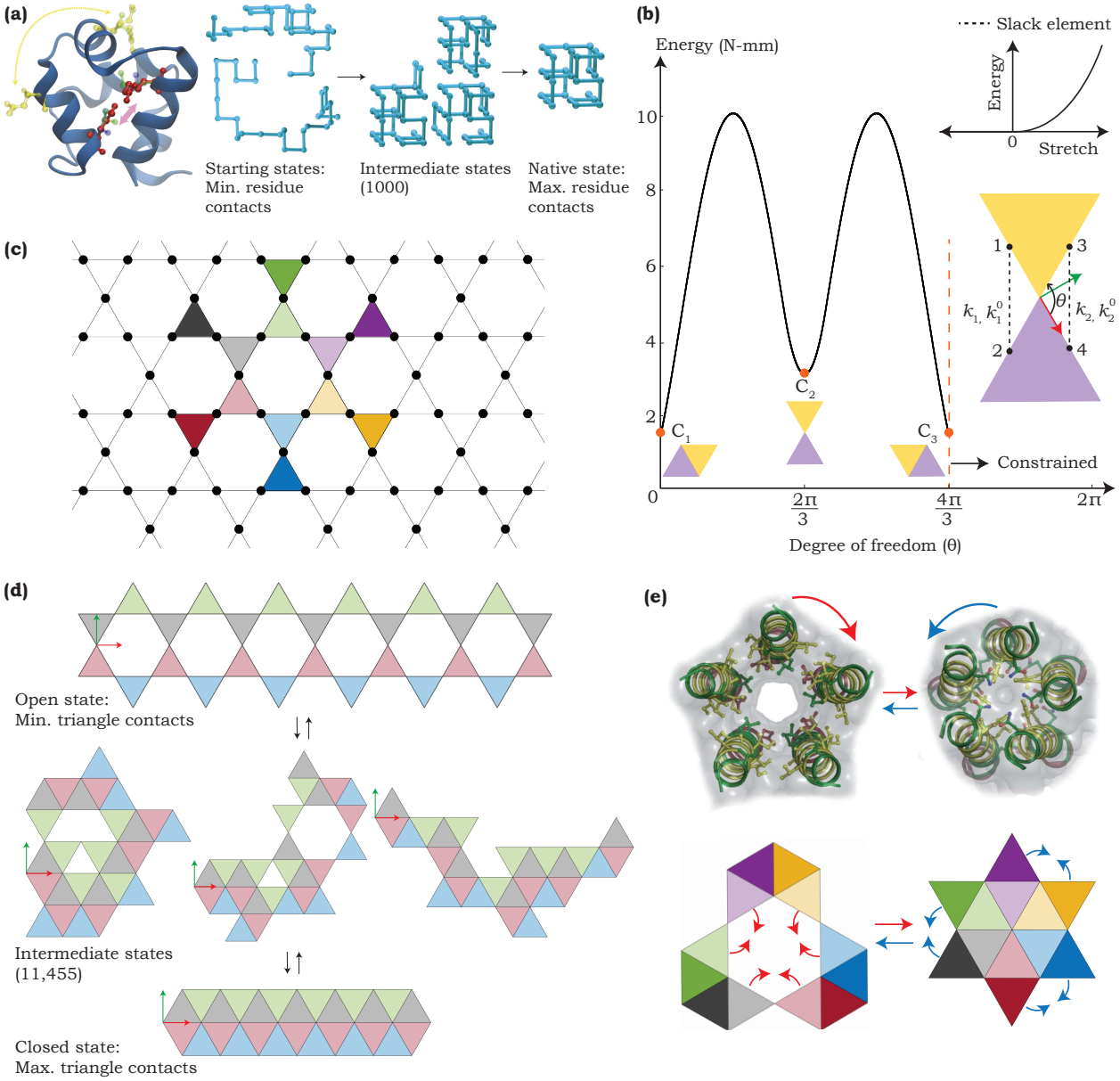

Figure 5.1: Multi-stable kagome lattice: ***(a)*** *Left panel: Illustration of a protein with amino acid residues in direct contact (pink arrows) and separated (yellow arrows), adapted from [91]. Right panel: Schematic of a 27-residue protein folding while increasing the number of residue contacts, adapted from [37].* ***(b)*** *Energy landscape of a tri-stable switch.* ***(c)*** *A unit cell of the kagome lattice shaded by light colors and nearest neighboring triangles to the unit cell in dark colors.* ***(d)*** *Examples of stable configurations of an array of 6 unit cells consisting of 26 triangles.* ***(e)*** *Top panel: Open and closed ligand-gated ion channels that differ by a twist about the pore axis, adapted from [14]. Bottom panel: Stable open and closed configurations obtained from a kagome lattice unit cell with its nearest neighbors. The red and blue arrows indicate the direction of twist (top panel) or rotation of rigid triangles (bottom panel) for forward and reverse transformations, respectively.*

Such an arrangement allows us to design an energy landscape for the switch that has three local minima – one that has zero energy gradient with respect to the degree of freedom $\left(\text{at } \theta^{(C_2)}\right)$ and two others that have non-zero gradient but act as local minima due to the rigid kinematic constraints imposed by the triangles $\left(\text{at } \theta^{(C_1)} \text{ and } \theta^{(C_3)}\right)$ as shown in Fig. 5.1(b). We consider $L = 50$ mm and $k_j^* = 0.1654$ N/mm measured from experiments. A simple tessellation of the tri-stable switch to form a unit cell of the kagome lattice (light colored triangles) is shown in Fig. 5.1(c). The arrangement can be made more complex by including the neighboring triangles to the unit cell (dark colored triangles). As shown in this work, the possible stable configurations for these tessellations display several interesting shapes with varying topologies (open and closed), and varying boundary area occupied including auxetic transformations. A larger array of unit cells periodic in one direction (Fig. 5.1(d)) closely mimics the idea of protein folding. In the array, we can identify the fully open stable state by least number of mechanical contacts between the faces of triangles and a fully closed stable state as one with the highest number of contacts. More importantly, there are thousands of intermediate stable states with arbitrarily complex shapes, identified by an intermediate number of contacts.

Combining multi-stable structures with stimuli-responsive materials allows for programmable and autonomous shape reconfigurability [23, 24, 51, 67]. Stimuli-responsive materials can also allow us to program multi-functional materials where a structure assumes different stable and functional configurations under different stimuli. The shape changes that are the most interesting for applications involve large changes in area and transformation between open and closed topologies. However, it is challenging to achieve reversible reconfigurability for a couple of reasons. First, the energy barrier to transform from one shape to another is often not the same as the reverse transformation and the difference tends to be large, and most studies focus on deployment along the direction with a smaller energy barrier. Second, most stimuli-responsive materials produce substantially larger forces under compression than expansion, which is rarely accommodated by the kinematics of the shape change in both directions. In this work, as our design allows us to create a large number of open and closed topologies with varying areas, we are able to pick pairs of shapes that can accommodate actuators that contract while morphing between the shapes in either direction. We demonstrate the reversible shape reconfigurability on two pairs of open and closed topologies using thermally actuated shape memory springs that are capable of exerting large forces. An example of a pair of open and closed structures is shown in the bottom panel of Fig. 5.1(e), where rigid triangles undergo rotations to transform from one stable shape to another. The mechanism closely resembles the working of a ligand-gated ion channel, where the pH of the surroundings causes a deformation that consists of an axial twist resulting in the rotation of individual protein helices, causing the pore to open or close [14, 95] (top panel in Fig. 5.1(e)).

5.3 Tessellating the tri-stable switch

In order to explore the possible stable shapes of different tessellations of the tri-stable switch, we first look at a single unit cell of a kagome lattice that has 6 rigid triangles (Fig. 5.1(c)). As each pair of adjacent triangles exhibits tri-stability, any internal angle of the hexagon formed by the inner loop in a stable state can take the values 0, $\frac{2\pi}{3}$, or $\frac{4\pi}{3}$. For example, the internal angles in the open configuration (Fig. 5.1(c) and Fig. 5.2(a)) are $\left[\frac{2\pi}{3}, \frac{2\pi}{3}, \frac{2\pi}{3}, \frac{2\pi}{3}, \frac{2\pi}{3}, \frac{2\pi}{3}\right]$. With 3 possibilities for each internal angle in a stable shape, and 6 total angles that need to be specified, there are a possible 729 combinations for the vector of internal angles. In the case where we are interested in the number of unique stable shapes, we eliminate the vectors of internal angles that are duplicates under circular permutation and under circular permutation of reversal of another vector. This eliminates shapes that are reflections and rotations of one another. We further ensure that the sum of internal angles in the hexagon equals 4π along with eliminating vectors that result in triangles overlapping with each other. The procedure yields a quadri-stable unit cell as shown in Fig. 5.2(a). The vectors of internal angles for the three closed stable shapes Closed 1, Closed 2, and Closed 3 are $\left[0, \frac{2\pi}{3}, \frac{4\pi}{3}, 0, \frac{2\pi}{3}, \frac{4\pi}{3}\right]$, $\left[0, \frac{4\pi}{3}, 0, \frac{4\pi}{3}, 0, \frac{4\pi}{3}\right]$, and $\left[0, \frac{2\pi}{3}, \frac{2\pi}{3}, 0, \frac{4\pi}{3}, \frac{4\pi}{3}\right]$, respectively.

Similarly to the identification of stable states of the tri-stable switch, we can identify the stable shapes of the quadri-stable unit cell by local minima on its energy landscape. The hexagonal unit cell with 6 rigid triangles is a 3 degree of freedom system from Maxwell's condition, that estimates the number of degrees of freedom of a planar n-bar mechanism as $n - 3$ [59, 83]. As it is difficult to represent the energy landscape with three varying angles, we pick kinematic paths where we fix the orientation of two triangles and vary the orientation of two others from 0 to 2π. The procedure to calculate the two remaining angles from n-2 known angles in a n-bar mechanism is detailed in Methods. The energy landscapes for two kinematic manifolds are shown in Fig. 5.2(b). The angle θ_i corresponds to the orientation of the i^{th} vector in Fig. 5.2(a), $i = 1, \ldots, 6$. The colored regions in the surface and contour plots in Fig. 5.2(b) indicate feasibility of a configuration, and the white regions indicate overlapping triangles (infeasible). In each case, the open stable shape is identified by a differentiable local minimum whereas stable shapes Closed 1, Closed 2, and Closed 3 occur at minima identified by corners of the landscape where we find mechanical contact between surfaces of triangles. The unmarked corners are stable configurations only for the specified kinematic paths, but are unstable otherwise.

We can increase the complexity of shapes by including the nearest neighboring triangles to the unit cell of the kagome lattice (Fig. 5.1(c)). In this case, there are 12 total angles that define a shape, i.e. 6 angles internal to a unit cell and 6 that are external, where each angle of a tri-stable switch can

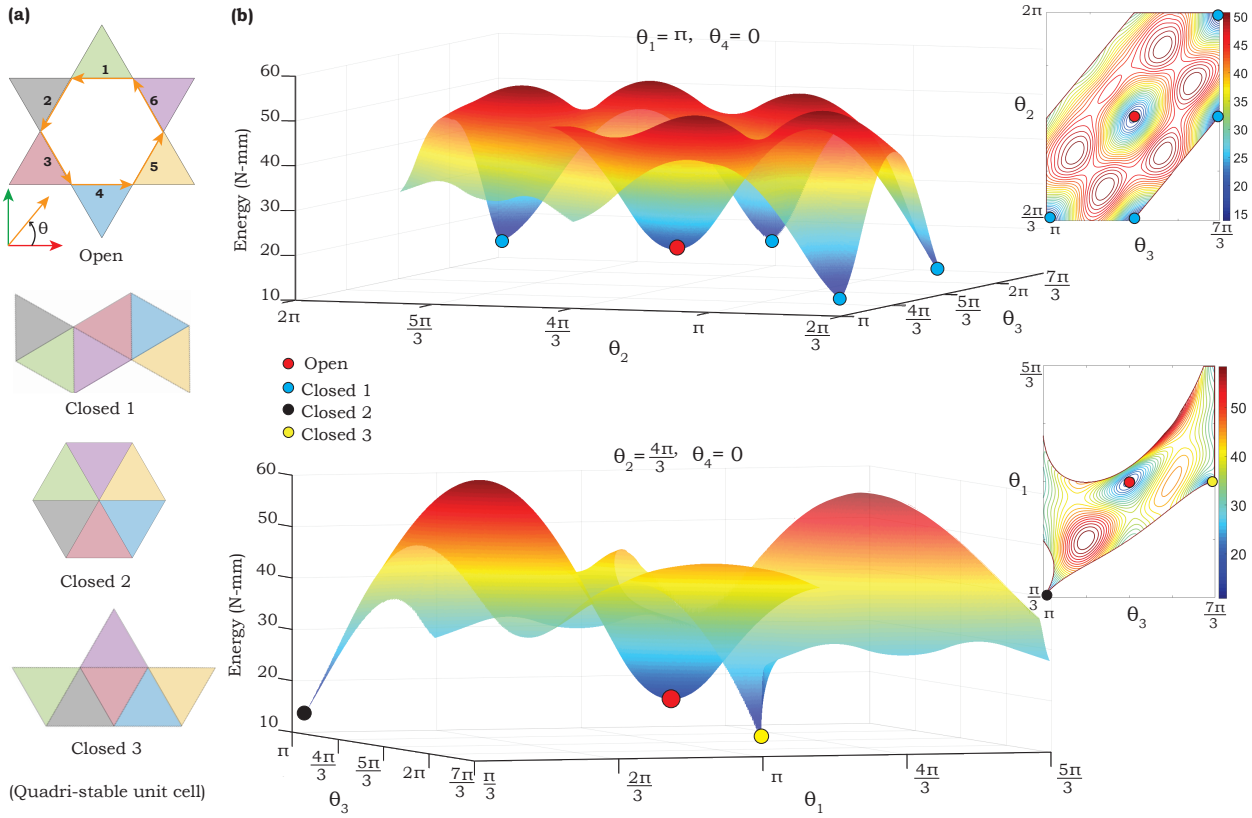

Figure 5.2: Energy landscapes: ***(a)*** *4 stable shapes of the kagome lattice unit cell.* ***(b)*** *Energy landscapes for two kinematic manifolds showing the stable shapes from (a) at local minima. The insets show the contour plots of energy for the respective manifolds.*

take a value 0, $\frac{2\pi}{3}$, or $\frac{4\pi}{3}$ for stability. For the inner loop assuming one of the 4 stable shapes in Fig. 5.2(a), we identify all sets of external angles for stability. Once again, we identify shapes that are unique under rotations and reflections with no overlapping triangles, which yields 116 unique stable shapes (Algorithm in Methods). Fig. 5.3(a) shows a few of the stable shapes, with the colored dots indicating the colors of triangles from Fig. 5.1(c). The first, second, and third rows display stable inner loops, Open, Closed 1, and Closed 2 from Fig. 5.2(a), respectively. The complete collection of stable shapes for the example can be found in the supplementary information. Another way to increase the complexity of shapes is by arraying a unit cell. The number of angles that defines the shape for a n-unit cell uni-directional array is $5n + 1$. Structures periodic in one direction with 2, 3, 4, 5, and 6 unit cells display 61, 227, 831, 3093, and 11457 stable configurations, respectively. Algorithm 8 in Methods outlines this calculation for n-unit cells. Examples of shapes with vastly different geometries and topologies are shown in Fig. 5.3(b) and Fig. 5.1(d). The origin in each configuration is located at the intersection of red and green axes.

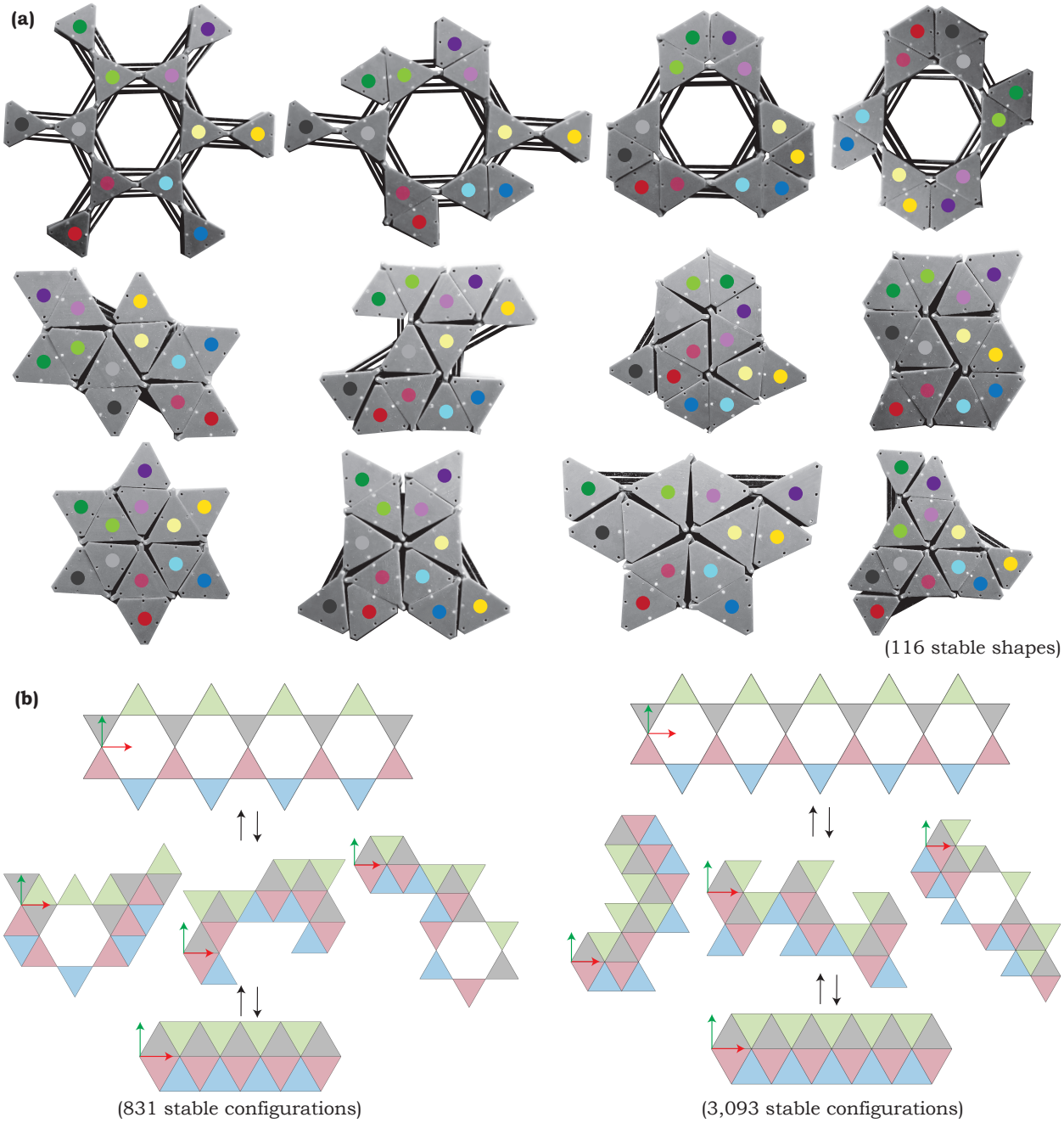

Figure 5.3: Multi-stable shapes: ***(a)*** *Examples of stable shapes for the structure with a single unit cell of the kagome lattice along with nearest neighboring triangles.* ***(b)*** *Examples of stable shapes for structures with an array of 4 and 5 unit cells of the kagome lattice.*

5.4 Experiments and results

We fabricate the structures discussed using a Stratasys Connex500 multi-material 3-D printer, where the rigid triangles are made from DM8530-GREY60 material, the pin joints from VeroWhite, and the slack elements from the soft TangoBlack [59]. The inset in Fig. 5.4(a) shows the construction of a tri-stable switch where the slack element is sandwiched between two layers of rigid triangles, to ensure that the structure remains planar when the element is stretched. Notice that the slack element engages only in tension due to its construction. The dimensions of the switch are obtained from the optimal design problem (5.2) and detailed earlier. The quasi-static stiffness of a slack element is measured over 4 samples using an Instron testing machine at a strain rate of 0.1 mm/s, as 0.1654 ± 0.0048 N/mm (Fig. 5.4(b)). Tessellating the switch to form a kagome lattice unit cell helps us realize the open and two closed stable shapes as show in in Fig. 5.4(a). The fourth shape, Closed 2 in Fig. 5.2(a), requires ideal pin joints with zero thickness, making it impossible to achieve experimentally. Fig. 5.3(a) shows 12 stable shapes on tessellating the tri-stable switch to include the nearest neighboring triangles to the unit cell.

We use the arrangement shown in Fig. 5.4(c) to measure the opening force for a tri-stable switch. The shaded triangles connected by a pin joint form a switch, which starts opening with Joule heating and subsequent contraction of a NiTi shape memory spring subjected to 1.5 V. The force exerted by the spring with a length of blue solid line in Fig. 5.4(c), with time is measured from the blue curve in Fig. 5.4(d). Here the spring is held at the fixed length in the Instron testing machine and force versus time is recorded on applying a voltage. We measure the time taken for the switch to open by a small angle $\beta = 2^\circ$ for 3 trials, where the spring is allowed to cool sufficiently long between cycles. The force is measured to be 0.6092 ± 0.0125 N. This closely matches the theoretically estimated force from a moment balance about the center of the switch, 0.5714 N. The parameters associated with the NiTi spring are detailed in methods.

We demonstrate reversible shape morphing between two pairs of open and closed stable shapes from Fig. 5.3(a) with an external stimulus. The two examples shown in Fig. 5.4(e) utilize multiple shape memory springs to manipulate the 3 degrees of freedom associated with the inner loop of triangles. In each example, the structure morphs from an open to closed state when the inner springs with ends marked by the red dots and indexed in white sufficiently contract on applying 1.5 V per spring for time T_1. Similarly the structure morphs from a closed to open shape when the outer springs connected by the blue dots and indexed in black sufficiently contract on applying the same voltage for time $T_3 - T_2$. The spring connecting the orange dots in Example 1 is not heated and maintains constant length while opening and closing. We measure the time for opening and closing while waiting sufficiently long between tests to allow for the NiTi springs to cool to room temperature, for 3 cycles. The NiTi springs are softer at room temperature compared to elevated temperatures,

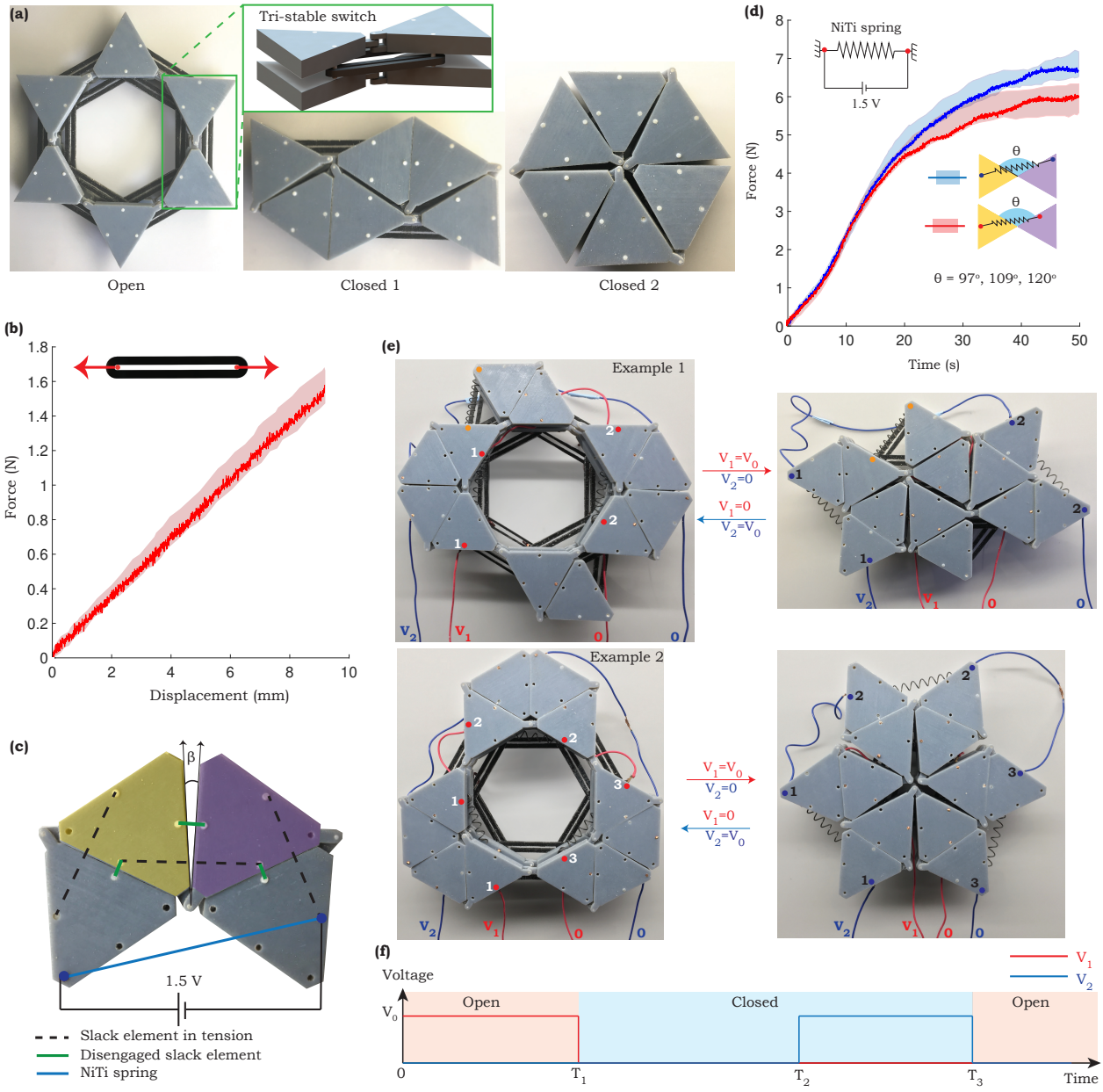

Figure 5.4: Experiments: ***(a)*** *Unit cell of the kagome lattice demonstrating 3 stable states. Close up shows the construction of a tri-stable switch.* ***(b)*** *Experimental results from tensile tests on a slack element. The solid curve indicates a representative sample.* ***(c)*** *Setup showing the opening of a tri-stable switch (shaded triangles) using Joule heating of shape memory spring.* ***(d)*** *Experimental results showing the force required to hold a shape memory spring at a fixed length versus time, for an applied voltage. The solid curves indicate* $\theta = 120°$. ***(e)*** *Two examples demonstrating reversible bi-stability between open and closed shapes with actuation triggered by Joule heating of shape memory springs.* ***(f)*** *Applied voltage over time to complete one cycle of opening and closing.*

Table 5.1: Summary of actuation time and force per NiTi spring for applied voltage of 1.5 V per spring

	Example 1	Example 2
T_1 (s)	17.495 ± 2.108	19.155 ± 1.836
$T_3 - T_2$ (s)	16.653 ± 1.368	16.660 ± 2.119
Closing force (N)	4.1220 ± 0.1231	4.3736 ± 0.1020
Opening force (N)	4.2363 ± 0.0882	4.2350 ± 0.0997

which allows the outer and inner springs to freely stretch in closing and opening, respectively. The measured times are summarized in Table 5.1. Notice that the springs are connected in series for actuation in each direction and the total applied voltage V_0 is 3V for Example 1 and 4.5 V for Example 2. This process is indicated in Fig. 5.4(f).

The locations of springs are chosen such that the kinematics of shape change in each direction allows for the desired springs to contract (see Methods). We observe that the structures snap in either direction, when the angle between triangles connected by heated springs decreases from 120° to 97° (see Methods). In order to estimate the force in a heated spring to close (open) a structure, we average the force in a spring heated for time T_1 ($T_3 - T_2$) spanning three lengths in the red (blue) region in Fig. 5.4(d). The force measurements are summarized in Table 5.1. These forces can be increases further at the expense of applied voltage, by using stiffer slack elements. Note that not only are the shape changes reversible, but each shape remains stable without needing an external stimulus.

5.5 Discussion

We utilize constraints such as rigid contact together with disengaging energy storing elements to introduce several additional stable states, compared to traditional methods that use linear energy storing elements alone. These constraints allow us to engineer highly non-linear energy landscapes to obtain complex shapes with arbitrary geometries and topologies. The array of unit cells (Fig. 5.1(d) and Fig. 5.3(b)) make it possible for any part of the structure to cover a large portion of a work-space, making it a useful candidate for a robotic arm with extensive reach. We can also obtain a great degree of control over the energy landscapes by altering the positions of energy storing elements, which can be useful in applications that involve gripping soft or hard objects. Further, as the structures can be engineered to display high structural rigidity together with large volume shape changes, they can be particularly useful in reversible aerospace deployment. Finally, the structure can snap into shapes with a varying number of holes, making the method extremely useful for flow control applications that may be triggered by heat, light, pH, or magnetic field, by using appropriate

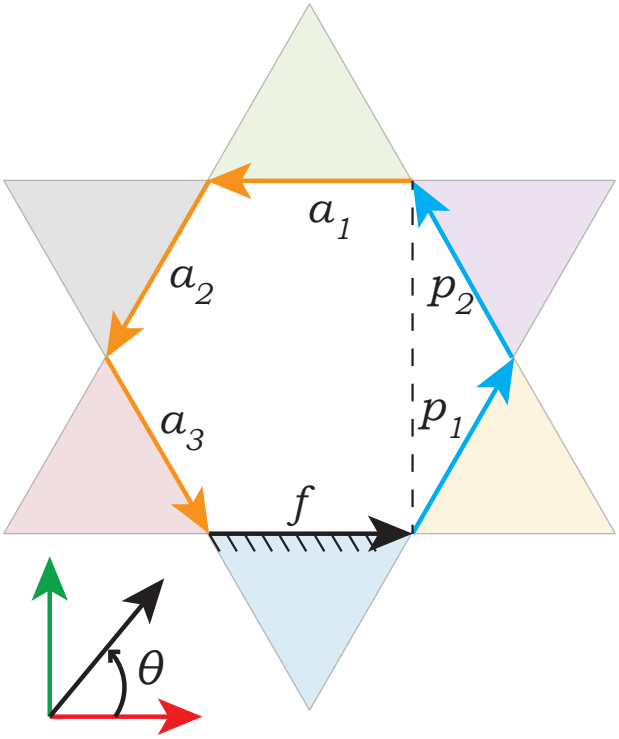

Figure 5.5: *A 6-triangle loop analyzed as a 6-bar mechanism.*

responsive materials. The same concept can be extended to shape morphing in higher dimensions, which leads to an increased kinematic space that would allow us to explore a much larger range of stable states.

5.6 Methods

5.6.1 Kinematics of a n-triangle loop

The kinematics of a loop of n rigid triangles can be treated as a loop of n rigid bars connected by pin-joints. Fig. 5.5 shows a configuration of the 6 triangle loop fully determined by the orientations of 6 bars. The kinematics of a planar n-bar mechanism can be understood from Maxwell's criterion [83],

$$2j - n - 3 = m - s, \tag{5.3}$$

where m is the number of degrees of freedom, s the number of states of self stress, and j the number of pin-joints. In a mechanism that is under-constrained (or without states of self stress), $s = 0$. When one of the bars is fixed to avoid translation or rotation, we need the orientations of $n - 3$ bars to determine the configuration of the system. Fig. 5.5 illustrates the concept where the black bar is fixed (f) and the orientations of the orange bars are the degrees of freedom (active bars a_1, a_2, a_3), when specified determine the orientation of the remaining bars in blue (passive bars p_1, p_2). Notice that the number of passive bars is 2 regardless of the number of bars n in the loop. We

denote each bar as a vector to represent its orientation with a unique direction. Let the lengths and orientations of the i^{th} active bar be r_{a_i} and θ_{a_i}, j^{th} passive bar be r_{p_j} and θ_{p_j}, and the fixed bar be r_f and θ_f, respectively. We have that

$$\begin{aligned}\sum_i r_{a_i}\cos\theta_{a_i} + \sum_j r_{p_j}\cos\theta_{p_j} + r_f\cos\theta_f = 0,\\ \sum_i r_{a_i}\sin\theta_{a_i} + \sum_j r_{p_j}\sin\theta_{p_j} + r_f\sin\theta_f = 0,\end{aligned} \tag{5.4}$$

where given θ_{a_i} and θ_f, we can calculate the orientation of passive bars as

$$\begin{aligned}\theta_{p_1} &= \tan^{-1}\left(\frac{B}{A}\right) + d\cos^{-1}\left(\frac{C}{\sqrt{A^2+B^2}}\right),\\ \theta_{p_2} &= \cos^{-1}\left(-\frac{\sum_i r_{a_i}\cos\theta_{a_i} + r_{p_1}\cos\theta_{p_1} + r_f\cos\theta_f}{r_{p_2}}\right),\end{aligned} \tag{5.5}$$

where

$$\begin{aligned}A =& 2r_{p_1}\left(\sum_i r_{a_i}\cos\theta_{a_i} + r_f\cos\theta_f\right),\\ B =& 2r_{p_1}\left(\sum_i r_{a_i}\sin\theta_{a_i} + r_f\sin\theta_f\right),\\ C =& r_{p_2}^2 - \left(r_f^2 + r_{p_1}^2 + \left(\sum_i r_{a_i}\cos\theta_{a_i}\right)^2 + \left(\sum_i r_{a_i}\sin\theta_{a_i}\right)^2 + 2r_f\cos\theta_f\sum_i r_{a_i}\cos\theta_{a_i}\right.\\ &\left. + 2r_f\sin\theta_f\sum_i r_{a_i}\sin\theta_{a_i}\right),\end{aligned}$$

and d is $+1$ or -1. In Fig. 5.5, the joint connecting the passive bars can lie on either side of the dashed line depending on the choice for d.

5.6.2 Actuation using shape memory springs

Each NiTi shape memory spring has a mandrel diameter of 4.75 mm, wire diameter of 0.75 mm and contains 18 turns. The springs are programmed to return to the fully contracted state (with no gaps between turns), when heated above the transition temperature of 45°C. In all our tests with Joule heating, each spring is subject to 1.5 V which corresponds to a current of 1.5 A.

In order to identify line segments that contract when a structure morphs from one configuration (C_1) to another (C_2), we evaluate all possible segments connecting pairs of triangles. Fig. 5.7 illustrates the idea where the line segment in red connecting two points indexed i and j in the i^{th} and j^{th} triangles, respectively, contracts when the structure closes. Let $\underset{\sim}{r}_{i,j}^{(C_n)}$ be a vector of length $r_{i,j}$ (orange arrows) connecting a pair of corner points in the triangles. Let the vector connecting

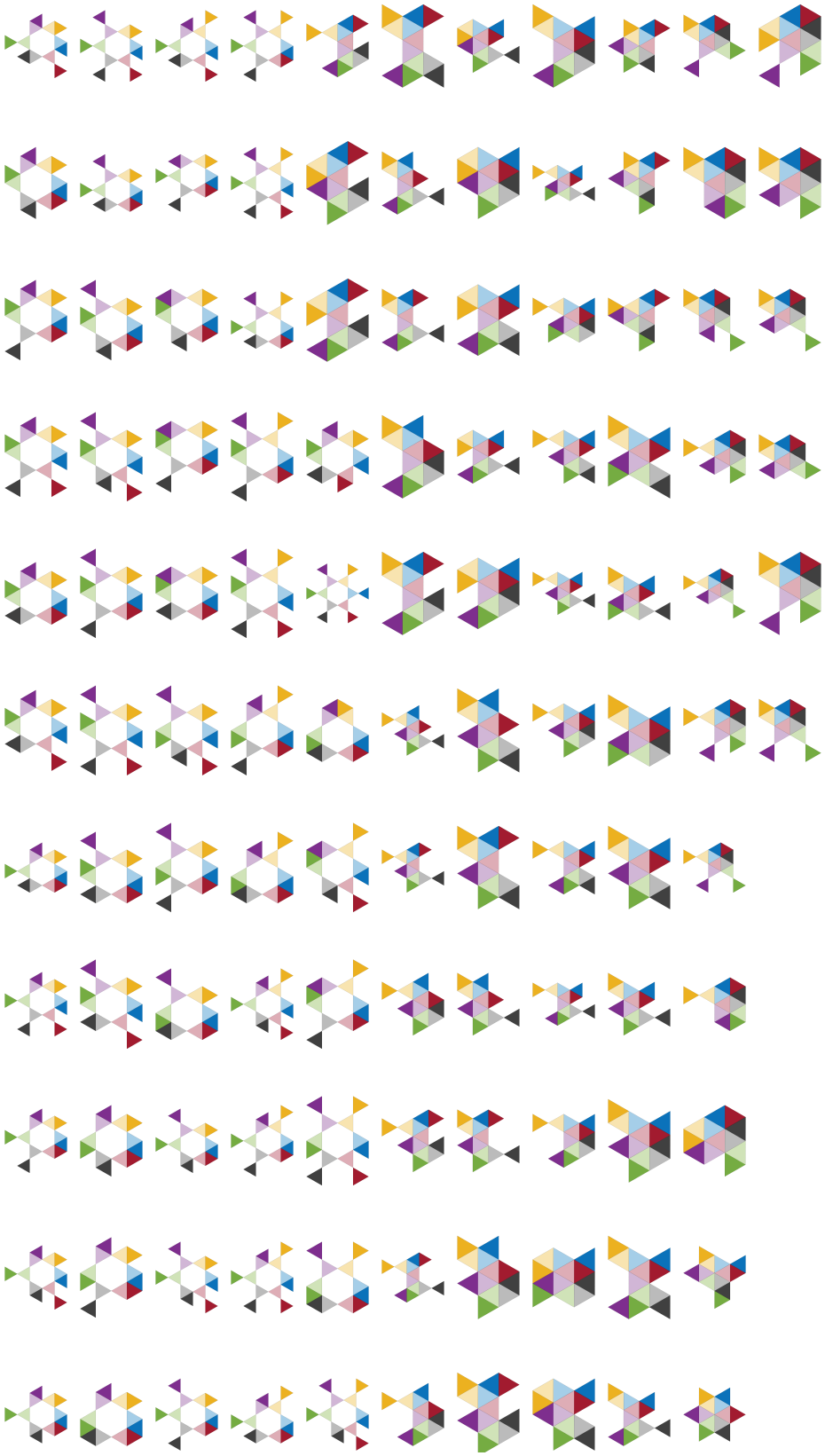

Figure 5.6: *116 stable shapes from the kagome lattice unit cell with nearest neighbors.*

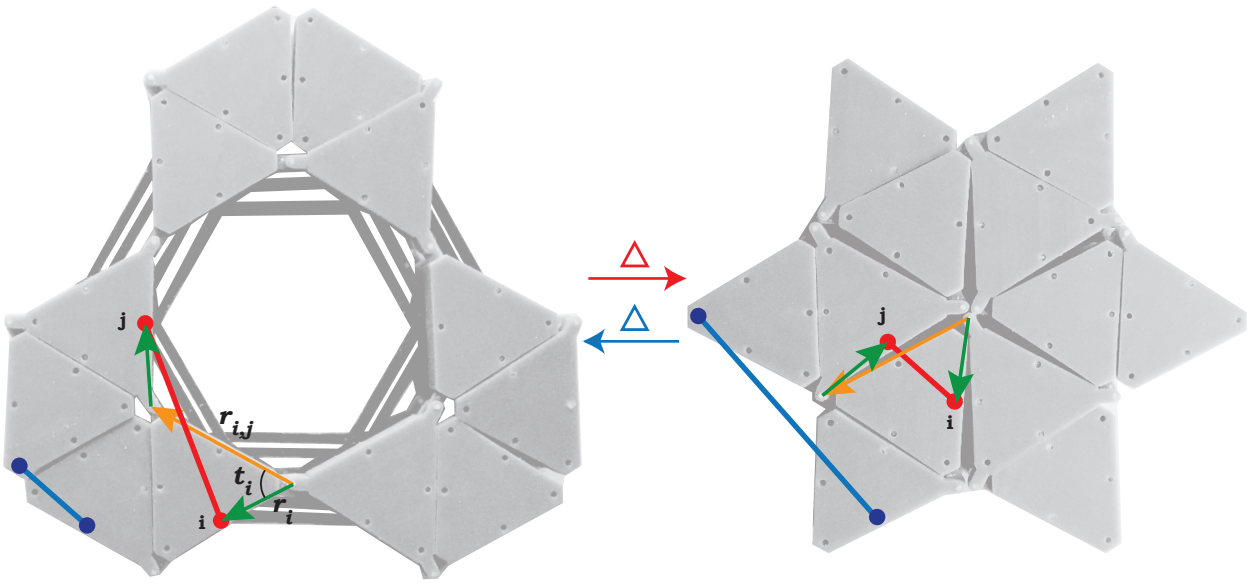

Figure 5.7: *Opening and closing of the structure involving red and blue segments/springs contracting, respectively.*

a corner point to an end of the line segment be $\underset{\sim}{r}_i^{(C_n)}$ (green arrows) in the i^{th} triangle. The vector has a length r_i and makes an angle t_i with $\underset{\sim}{r}_{i,j}^{(C_n)}$. The length of the segment connecting the points i and j in configuration C_n can be calculated from the sum of the orange and green vectors, i.e. $l_{i,j}^{(C_n)} = |\underset{\sim}{r}_i^{(C_n)} \pm \underset{\sim}{r}_{i,j}^{(C_n)} \pm \underset{\sim}{r}_j^{(C_n)}|$. We solve the optimization problem

$$\begin{aligned} \min_{r_i, r_j, t_i, t_j} \quad & l_{i,j}^{(C_2)} - l_{i,j}^{(C_1)} \\ \text{subject to} \quad & 0 \le r_q \le L, \\ & 0 \le t_q \le \frac{\pi}{3}, \\ & 0 \le r_q(\sin t_q + \sqrt{3}\cos t_q) \le L\sqrt{3}, \\ & q = i,\ j, \end{aligned} \tag{5.6}$$

for all pairs of triangles and identify those pairs where the objective is negative, which indicates that a line segment contracts between the pairs of triangles when the structure transforms from C_1 to C_2. Here L is the side-length of a triangle, and the constraints ensure that the points i and j lie within the respective triangles. Once we identify pairs of triangles where there exists a line segment that contracts, we pick a contracting segment (represents a shape memory spring) with end points that are accessible to attach the spring during fabrication. We also ensure that the spring is not obstructed during each cycle. In Fig. 5.7, the blue segment/spring contracts when the structure opens and the red segment/spring contracts when the structure closes. We achieve this contraction through Joule heating. As the inner loop is a 3 degree of freedom mechanism, we

need to manipulate the lengths of 3 springs in either direction as indicated in Fig. 4. Notice that opening the structure requires springs to contract outside the inner loop of triangles and closing the structure requires springs to contract interior to this loop.

5.6.3 Force of actuation

The shape changes in Fig. 4 are gradual on heating respective springs until the structure reaches an intermediate shape, at which the structure snaps close or open (Fig. 5.8 and Fig. 5.9). We obtain these intermediate shapes at the frame just before the structure snaps. We measure the least angle between the triangles connecting the heated springs in each intermediate state, and average it across all intermediate states. This average angle at which the structures snap is 97°. The amount of time the springs are heated for an open structure to reach intermediate 1 is T_1, and for a closed structure to reach intermediate 2 is $T_3 - T_2$, in both examples. This time is spent in gradually contracting the angle from 120° to 97°. In order to estimate the force in a heated spring at an intermediate state, we average the force exerted by a spring with its ends held at three lengths that correspond to angles 120°, 109°, and 97°, on passing a current for time T_1 (opening) or $T_3 - T_2$ (closing). These forces lie in the blue (a spring that opens the structure) and red (a spring that closes the structure) regions in Fig. 4(d).

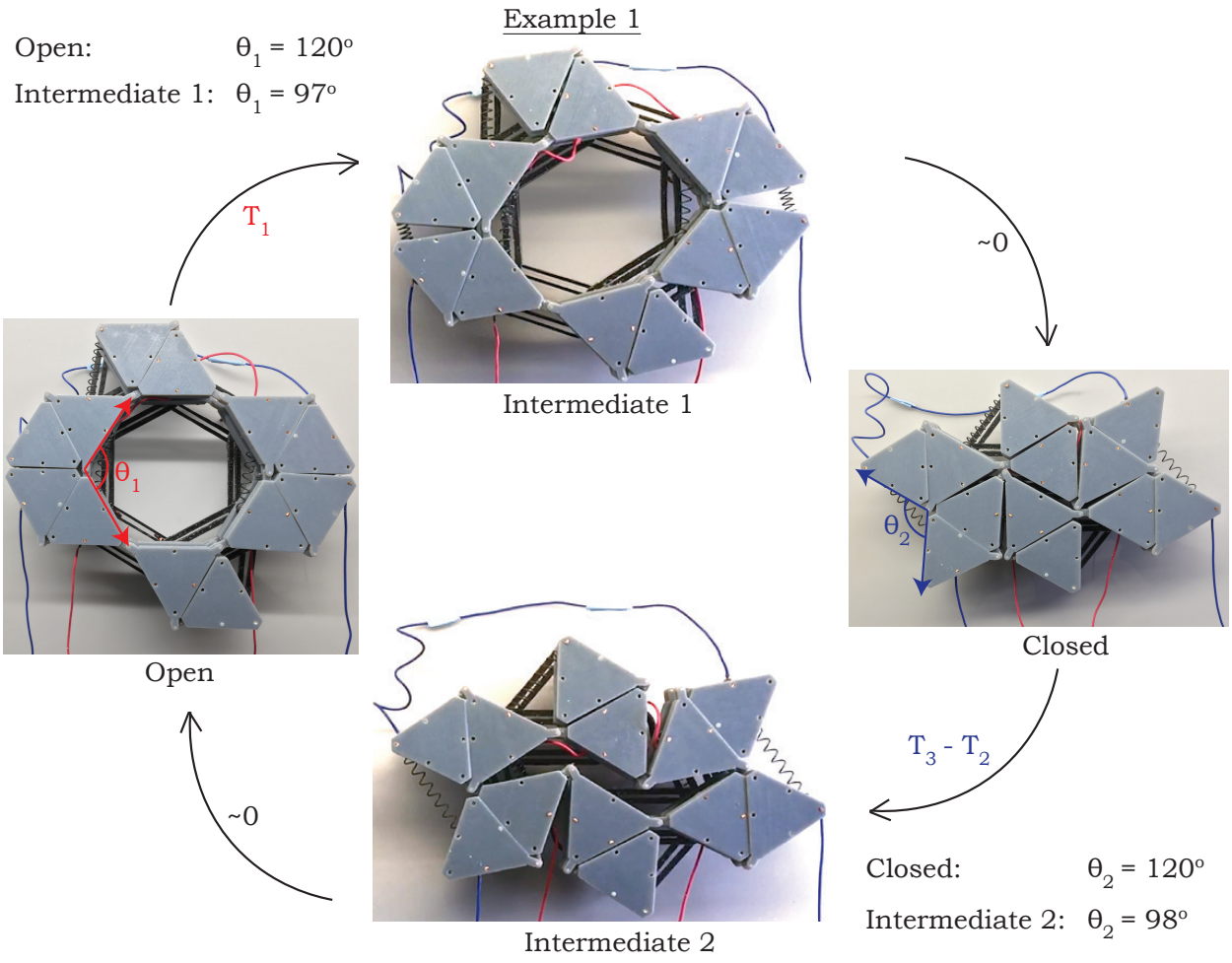

Figure 5.8: *The structures in Example 1 snap to open or closed shapes on reaching the intermediate shapes as the springs are heated.*

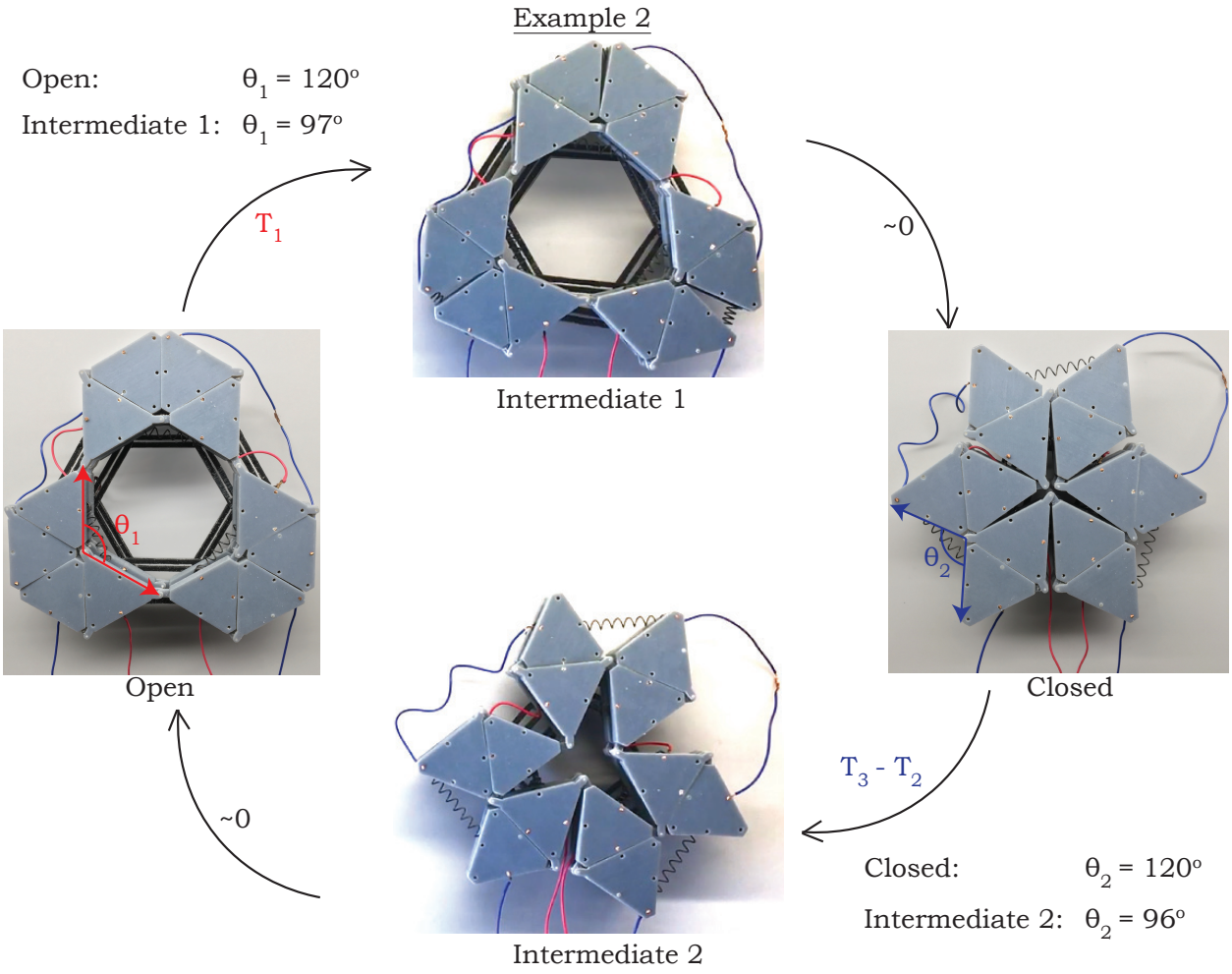

Figure 5.9: *The structures in Example 2 snap to open or closed shapes on reaching the intermediate shapes as the springs are heated.*

Algorithm 7 Unique stable shapes of kagome lattice unit cell with nearest neighboring triangles

V is a matrix of size 4×6 where a row is a vector of internal angles in the unit cell that corresponds to one of the 4 stable states.

P is a matrix of size 729×6 in which each element is either 0, 120, or 240 (degrees), and each row is unique. Each row of P represents a vector of angles external to the unit cell.

Shapes with no overlapping triangles:

count = 0 (number of shapes with no overlapping triangles)
for i_1=1 to size (V, 1) **do**
    for i_2=1 to size (P, 1) **do**
        Compute all end points of triangles
        Compute all centroids of triangles
        if Distance between two centroids < small positive tolerance
            Triangles overlap
        else
            No two triangles overlap
            count += 1
            Create matrix Q (count) such that its rows are unique end points of triangles
        end if
    end for
end for

Shapes unique under rotation, translation and/ or reflection:

Check if two sets of N points in 2-D differ by a rotation and translation:
Let the first set of points be S_1 and the second be S_2 (each of size $N \times 2$).
To each row of both matrices, add a third element equal to unity.
Compute the matrix A, such that S_1.A=S, where S = S_2.
Repeat the above step for all S that are obtained from permutations of the rows of S_2.
if A in the above two steps ever takes the form $\begin{pmatrix} \cos\theta & \sin\theta & x_{trans} \\ -\sin\theta & \cos\theta & y_{trans} \\ 0 & 0 & 1 \end{pmatrix}$, the sets of points S_1 and S_2 differ by a rotation and translation.

Pick two sets of points Q_i and Q_j that are elements of Q.
Check lines 17-21 for Q_i and Q_j, Q_i and reflection of Q_j about horizontal axis, and Q_i and reflection of Q_j about vertical axis.
If A ever takes the specified form, the shapes indexed by count= i and j differ by a rotation, translation, and/ or reflection.

Algorithm 8 Unique stable configurations of an array of N kagome lattice unit cells

1: Create a matrix U = V (from Algorithm S1). Add rows to U that are circular permutations of rows of V, and circular permutations of the flipped rows of V. Remove the duplicate rows from U such that every row is unique.
2: Initialize a matrix S=[ ]
3: Create a matrix M of size N $\times$ 6, such that a row in M is a row from U.
4: Check in M if the sum of the n^{th} element in a row and the m^{th} element in the preceding row is 240. n and m are chosen based on the triangles shared by two adjacent unit cells. If the check is true for all rows of M starting from the second row, then update S = [S; M].
5: Repeat the step above for all possible M.
6: For every element in S, eliminate the configurations with overlapping triangles using lines 6-11 in Algorithm S1.
7: In order to calculate shapes that are unique under rotation, translation, and/ or reflection, repeat steps 18-24 for all pairs of shapes obtained in the step above.
(Note that in the paper, we do not carry out the last step and we report the total number of unique configurations with respect to a fixed axis, which is useful in understanding the work-space covered by the array when used as a robotic arm)

Chapter 6

CONCLUSIONS AND FUTURE WORK

6.1 Summary

In this thesis, we study a series of problems that design and optimize multiple functions in architected structures and mechanisms. In the first part (Chapter 2), we decouple failure load from stiffness and density, by utilizing internal stresses in truss-like structures. In the second part (Chapter 3), we optimally design for the acoustic impedance in load-bearing structures by decoupling the wave speed from static stiffness and density. Such design is made possible by utilizing point masses embedded in an architected lattice. In the third part (Chapter 4), we engineer particular wave speeds and frequency bandgaps in a pair of architected lattices to demultiplex mixed modes. In the fourth part (Chapter 5), we design a structure that displays arbitrarily complex multi-stable topologies, by incorporating rigid kinematic constraints together with disengaging springs.

In Chapter 2, we express the failure load and stiffness of truss-like structures in terms of their geometrical parameters and internal stress distribution. We provide a sensitivity analysis using an adjoint method to calculate bounds on these mechanical properties. We first show the bounds when we vary the cross-sectional areas of bars alone, and recalculate bounds on varying both cross-sectional areas and pre-stress in bars. We show that with the addition of internal stress in an octahedral truss, we can increase the failure load two-fold, without changing its stiffness. Any desired internal stress state in the structure can be simulated by pre-compressing selected bars, which we do by introducing *slack* in those bars. The approach can be used to design lightweight structures with arbitrary stiffness and failure load, as the properties vary linearly with relative density for stretch dominated structures.

In Chapters 3 and 4, we present a sensitivity analysis to design the elastic wave speed in a structure for a chosen mode at a frequency of operation. In doing so, we calculate the implicit derivatives, which are the sensitivities of the mode shape with respect to the topological variables. We are able to optimize the group velocity independently from the static stiffness with the addition of point masses in lattice structures. We calculate bounds on group velocity and stiffness in the longitudinal direction for 5 periodic 3-D lattices (SC, BCC, FCC, octet, and hexagonal). As the lattices display slender struts, we model them using frame elements to calculate these bounds, and we verify our analysis with a finite element solver that uses 3-D solid elements. The point masses in experiments are made from Tungsten-Carbide ball bearings, that are attached to 3-D printed lattices. We measure the engineered group velocity and reconstruct the dispersion curve experimentally in two

BCC lattices, one which displays the highest wave speed and another with an intermediate wave speed. We also design and demonstrate a mode demultiplexer that can split longitudinal and shear waves at a chosen frequency into its individual components. We do so by engineering two lattice channels, one that propagates longitudinal modes but not shear modes and the other propagates shear modes but not longitudinal modes. We optimize the respective group velocities and band gaps using the sensitivity analysis derived. We validate our analysis with experiments on 3-D printed channels, by studying the frequency transmission in each lattice as well as reconstructing the dispersion curves.

In Chapter 5, we design a tri-stable switch which, when arranged in a kagome lattice configuration, produces a quadri-stable unit cell and thousands of stable states in larger tessellations. We are able to engineer highly non-linear energy landscapes by utilizing rigid kinematic constraints through mechanical contact and disengaging energy storing elements (*slack* elements). We demonstrate multi-stability on 3-D printed structures where the rigid triangles display a much higher stiffness compared to the energy storing elements. We show reversible shape morphing between two pairs of open and closed shapes, that are actuated through Joule heating of shape memory springs. We validate the force needed to open a tri-stable switch and we also measure the force in a spring to transition between stable open and closed shapes. These forces of actuation can be scaled according for an application, by adjusting the stiffness of the slack elements.

6.2 Future work

Tunable metamaterials

- *Tunable failure characteristics*: In this research, we design complex trusses with optimized failure load and quasi-static stiffness, by varying the internal stress distribution within the system. In order to design a pre-stress distribution, we pre-compress specific bars. However, each theoretically obtained pre-stress distribution would optimize the failure load for a specific loading direction. We can replace some of the bars with stimuli responsive materials such as piezoelectric, liquid crystal elastomers or shape memory polymers. By selectively actuating specific sites, we can obtain a wide range of pre-stress distributions within the truss, which would enhance its failure load under several loading conditions. In addition to delaying failure, we can also use this method to tune in real-time the failure path within the structure. This would be useful in improving the life of a structure where replacements are difficult, such as space structures. We can also look at ways to induce controlled pre-stress during the fabrication of a structure such as by controlling the UV exposure to selected bars during polymerization in the 3-D printing process.

- *Adaptive dispersion properties*: We have shown that most dispersion properties of metama-

terials are highly sensitive to parameters such as local stiffness of elements and minor changes in topological parameters. We can exploit this feature by incorporating polymers within the structures, that are stimuli-responsive, and ultimately tune multiple dispersion properties simultaneously by controlling external stimuli (heat, light, electric or magnetic field).

Interpenetrating/ woven lattices

Lattices have proved to be an effective way of making structures with optimized mechanical properties, for two main reasons. First, the numerical methods describing their mechanics can be simplified to truss/ beam based models and they provide a reduced search space for parameters describing their topology, which simplifies the design process. Second, additive manufacturing has made it possible to fabricate highly complex geometries. However, most lattices are designed under the constraint that the relative density can not exceed 10% for simplified numerics to be valid, creating *hollow* materials. Hence, we can *interpenetrate/ weave* lattices together, thereby creating packed structures that are still easy to model and fabricate, but display unprecedented mechanical properties.

- *Stiff lattices with low wave speed*: Interpenetrating lattices would display superior stiffness for small deformation dictated by the sum of linear response of individual lattices, and extremely high stiffness at finite deformation due to contact among bars. However, the vibration response remains unaffected as the lattices remain contact free for small deformation. This would allow us to create densely packed, compact, strong, and stiff structures with arbitrary vibration mechanics. These lattices would be valuable to design devices where high structural rigidity is important with moderate wave speeds, such as underwater sonar windows, ultrasonography, and hydrophone casings.

- *Non-reciprocal lattices*: We can also exploit the bi-linear elastic response of these woven lattices. The design can be made such that the stiffness is extremely high under one loading direction, say compression and low under another, say tension. This can be made possible by interference of bars under a certain loading direction and not in the opposite direction. A bi-linear response would allow for the design of non-reciprocal dynamics, where wave propagation is different in opposite directions. This would allow for the design of compact acoustic diodes that display sufficient rigidity, to help realise phononic computers.

- *Pre-stressed lattices*: Loading or unloading the lattice at finite deformations can change its dynamic response tremendously. For example, with the same structure, at the same operating frequency but at different static pre-stress, we can design band gaps, standing waves, fast or slow propagating waves, or arbitrary modes of propagation.

- *Lattices in media*: We can extend our work on the dynamics of lattices in vacuum to include fluid-structure interaction to optimize the dispersion characteristics in media such as water. This is particularly useful in marine and biological applications.

Multi-stable shape morphing

- *3-D shape morphing*: In this thesis, we study 2-D shape morphing structures. The design of our tri-stable switch is such that two sides of a triangle act as rigid kinematic constraints. However, the number of possible mechanical contacts can be drastically increased on moving to three dimensions. Also, the kinematics become highly complex and we can expect a much larger range of admissible shapes in 3-D.

- *Larger tessellations*: In our work, we thermally actuate the shapes using Joule heating to demonstrate reversible bi-stability. We can fabricate larger tessellations of the tri-stable switch and demonstrate reversible shape morphing between several stable shapes. Also, by incorporating other stimuli responsive materials, we can switch between a larger number of shapes in response to individual stimuli.

- *Stiffness and energy barrier*: In application, the structural rigidity of a stable shape as well as energy needed to transition between shapes are important. Often, we would want the former to be high and the latter to be low, which is difficult to achieve because of the strong correlation between the quantities. We can look at ways to decouple these quantities and individually design them for different applications.

BIBLIOGRAPHY

[1] Amado-Becker, A., Ramos-Grez, J., José Yañez, M., Vargas, Y. & Gaete, L. (2008). Elastic tensor stiffness coefficients for sls nylon 12 under different degrees of densification as measured by ultrasonic technique. *Rapid Prototyping Journal*, *14*(5), 260–270. https://doi.org/10.1108/13552540810907929

[2] Anderson, B. E., Hughes, W. J. & Hambric, S. A. (2008). On the steering of sound energy through a supercritical plate by a near-field transducer array. *The Journal of the Acoustical Society of America*, *123*(5), 2613–2619.

[3] Andreassen, E., Chang, H. R., Ruzzene, M. & Jensen, J. S. (2016). Optimization of directional elastic energy propagation. *Journal of Sound and Vibration*, *379*, 53–70. https://doi.org/10.1016/j.jsv.2016.03.002

[4] Ashby, M. F. (2006). The properties of foams and lattices. *Philosophical Transactions of the Royal Society A*, *364*(1838), 15–30. https://doi.org/10.1098/rsta.2005.1678

[5] Babaee, S., Viard, N., Wang, P., Fang, N. X. & Bertoldi, K. (2016). Harnessing deformation to switch on and off the propagation of sound. *Advanced Materials*, *28*(8), 1631–1635.

[6] Bacigalupo, A., Lepidi, M., Gnecco, G., Vadalà, F. & Gambarotta, L. (2019). Optimal design of the band structure for beam lattice metamaterials. *Frontiers in Materials*, *6*, 2. https://doi.org/10.3389/fmats.2019.00002

[7] Bauer, J., Meza, L. R., Schaedler, T. A., Schwaiger, R., Zheng, X. & Valdevit, L. (2017). Nanolattices: An emerging class of mechanical metamaterials. *Advanced Materials*, *29*(40), 1701850. https://doi.org/10.1002/adma.201701850

[8] Bayat, A. & Gaitanaros, S. (2017). Wave directionality in three-dimensional periodic lattices. *Journal of Applied Mechanics*, *85*(1). https://doi.org/10.1115/1.4038287

[9] Bendsoe, M. P. & Sigmund, O. (2004). *Topology optimization: Theory, methods and applications*. Springer.

[10] Berger, J. B., Wadley, H. N. G. & McMeeking, R. M. (2017a). Mechanical metamaterials at the theoretical limit of isotropic elastic stiffness. *Nature*, *543*(7646), 533–537.

[11] Berger, J. B., Wadley, H. N. G. & McMeeking, R. M. (2017b). Mechanical metamaterials at the theoretical limit of isotropic elastic stiffness. *Nature*, *543*, 533–537. https://doi.org/10.1038/nature21075

[12] Bilal, O. R. & Hussein, M. I. (2011). Ultrawide phononic band gap for combined in-plane and out-of-plane waves. *Physical Review E*, *84*, 065701. https://doi.org/10.1103/PhysRevE.84.065701

[13] Bilal, O. R., Foehr, A. & Daraio, C. (2017). Bistable metamaterial for switching and cascading elastic vibrations. *Proceedings of the National Academy of Sciences*, *114*(18), 4603–4606.

[14] Bocquet, N., Nury, H., Baaden, M., Le Poupon, C., Changeux, J.-P., Delarue, M. & Corringer, P.-J. (2009). X-ray structure of a pentameric ligand-gated ion channel in an apparently open conformation. *Nature*, *457*(7225), 111–114.

[15] Boechler, N., Theocharis, G. & Daraio, C. (2011). Bifurcation-based acoustic switching and rectification. *Nature Materials*, *10*(9), 665–668.

[16] Brillouin, L. (1953). *Wave propagation in periodic structures* (Second). Dover.

[17] Bringuier, S., Swinteck, N., Vasseur, J., Robillard, J.-F., Runge, K., Muralidharan, K. & Deymier, P. A. (2011). Phase-controlling phononic crystals: Realization of acoustic boolean logic gates. *The Journal of the Acoustical Society of America*, *130*(4), 1919–1925.

[18] Bückmann, T., Stenger, N., Kadic, M., Kaschke, J., Frölich, A., Kennerknecht, T., Eberl, C., Thiel, M. & Wegener, M. (2012). Tailored 3D mechanical metamaterials made by dip-in direct-laser-writing optical lithography. *Advanced Materials*, *24*(20), 2710–2714.

[19] Casadei, F. & Rimoli, J. (2013). Anisotropy-induced broadband stress wave steering in periodic lattices. *International Journal of Solids and Structures*, *50*(9), 1402–1414. https://doi.org/10.1016/j.ijsolstr.2013.01.015

[20] Celli, P. & Gonella, S. (2014). Laser-enabled experimental wavefield reconstruction in two-dimensional phononic crystals. *Journal of Sound and Vibration*, *333*(1), 114–123. https://doi.org/10.1016/j.jsv.2013.09.001

[21] Celli, P., Yousefzadeh, B., Daraio, C. & Gonella, S. (2019). Bandgap widening by disorder in rainbow metamaterials. *Applied Physics Letters*, *114*(9), 091903. https://doi.org/10.1063/1.5081916

[22] Chang, C. W., Okawa, D., Majumdar, A. & Zettl, A. (2006). Solid-state thermal rectifier. *Science*, *314*(5802), 1121–1124.

[23] Chen, T., Bilal, O. R., Lang, R., Daraio, C. & Shea, K. (2019). Autonomous deployment of a solar panel using elastic origami and distributed shape-memory-polymer actuators. *Physical Review Applied*, *11*(6), 064069.

[24] Chen, T., Bilal, O. R., Shea, K. & Daraio, C. (2018). Harnessing bistability for directional propulsion of soft, untethered robots. *Proceedings of the National Academy of Sciences*, *115*(22), 5698–5702.

[25] Chen, T. & Shea, K. (2018). An autonomous programmable actuator and shape reconfigurable structures using bistability and shape memory polymers. *3D Printing and Additive Manufacturing*, *5*(2), 91–101.

[26] Chen, W., Rajaram, S., Thomas, S. & Nutt, S. R. (2009). Carbon nanotube reinforced acoustically transparent epoxy nanocomposites for underwater sonar windows.

[27] Chernow, V. F., Alaeian, H., Dionne, J. A. & Greer, J. R. (2015). Polymer lattices as mechanically tunable 3-dimensional photonic crystals operating in the infrared. *Applied Physics Letters*, *107*(10), 101905. https://doi.org/10.1063/1.4930819

[28] Cheung, K. C. & Gershenfeld, N. (2013). Reversibly assembled cellular composite materials. *Science*.

[29] Christiansen, R. E., Wang, F. & Sigmund, O. (2019). Topological insulators by topology optimization. *Physical Review Letters*, *122*, 234502. https://doi.org/10.1103/PhysRevLett.122.234502

[30] Cochran, J., Lee, K., McDowell, D. & Sanders, T. (2002). Multifunctional metallic honeycombs by thermal chemical processing. *Processing and Properties of Lightweight Cellular Metals and Structures, Global Symposium on Materials Processing and Manufacturing, 3, TMS Annual Meeting, 131*.

[31] Dahl, J., Jensen, J. S. & Sigmund, O. (2008). Topology optimization for transient wave propagation problems in one dimension. *Structural and Multidisciplinary Optimization*, *36*(6), 585–595. https://doi.org/10.1007/s00158-007-0192-5

[32] Dam, C. Q., Brezny, R. & Green, D. J. (1990). Compressive behavior and deformation-mode map of an open cell alumina. *Journal of Materials Research*.

[33] Dean, J., Bryan, M., Cooper, J., Virbule, A., Cunningham, J. & Hayward, T. (2015). A sound idea: Manipulating domain walls in magnetic nanowires using surface acoustic waves. *Applied Physics Letters*, *107*(14), 142405.

[34] Deshpande, V. S. & Fleck, N. A. (2001). Collapse of truss core sandwich beams in 3-point bending. *International Journal of Solids and Structures*, *38*(36), 6275–6305. https://doi.org/10.1016/S0020-7683(01)00103-2

[35] Deshpande, V., Fleck, N. & Ashby, M. (2001). Effective properties of the octet-truss lattice material. *Journal of the Mechanics and Physics of Solids*, *49*(8), 1747–1769. https://doi.org/10.1016/S0022-5096(01)00010-2

[36] Devaux, T., Tournat, V., Richoux, O. & Pagneux, V. (2015). Asymmetric acoustic propagation of wave packets via the self-demodulation effect. *Physical Review Letters*, *115*(23), 234301.

[37] Dinner, A. R., Šali, A., Smith, L. J., Dobson, C. M. & Karplus, M. (2000). Understanding protein folding via free-energy surfaces from theory and experiment. *Trends in Biochemical Sciences*, *25*(7), 331–339.

[38] Eichenfield, M., Chan, J., Camacho, R. M., Vahala, K. J. & Painter, O. (2009). Optomechanical crystals. *Nature*, *462*(7269), 78–82.

[39] Evans, A. G., Hutchinson, J. W., Fleck, N. A., Ashby, M. F. & Wadley, H. N. G. (2001). The topological design of multifunctional cellular metals. *Progress in Materials Science*, *46*(3), 309–327. https://doi.org/10.1016/S0079-6425(00)00016-5

[40] Evans, K. E. & Alderson, A. (2000). Auxetic materials: Functional materials and structures from lateral thinking! *Advanced Materials*, *12*(9), 617–628.

[41] Fan, H., Hartshorn, C., Buchheit, T., Tallant, D., Assink, R., Simpson, R., Kissel, D. J., Lacks, D. J., Torquato, S. & Brinker, C. J. (2007). Modulus-density scaling behaviour and framework architecture of nanoporous self-assembled silicas. *Nature Materials*.

[42] Fleck, N. A., Deshpande, V. S. & Ashby, M. F. (2010). Micro-architectured materials: Past, present and future. *Proceedings of the Royal Society A*, *466*(2121), 2495–2516. https://doi.org/10.1098/rspa.2010.0215

[43] Francfort, G. A. & Murat, F. (1986). Homogenization and optimal bounds in linear elasticity. *Archive of Rational Mechanics and analysis*, *94*(4), 307–334.

[44] Gazonas, G. A., Weile, D. S., Wildman, R. & Mohan, A. (2006). Genetic algorithm optimization of phononic bandgap structures. *International Journal of Solids and Structures*, *43*(18), 5851–5866. https://doi.org/10.1016/j.ijsolstr.2005.12.002

[45] Gibson, I., Rosen, D. W. & Brent, S. (2010). *Additive manufacturing technologies*. Berlin: Springer.

[46] Gibson, L. J. & Ashby, M. F. (1990). *Cellular solids: Structure and properties*.

[47] Gibson, L. J. & Ashby, M. F. (1997). *Cellular solids, structure and properties*. Cambridge University Press.

[48] Gonella, S. & Ruzzene, M. (2008). Analysis of in-plane wave propagation in hexagonal and re-entrant lattices. *Journal of Sound and Vibration*, *312*(1), 125–139. https://doi.org/10.1016/j.jsv.2007.10.033

[49] Graff, K. F. (2012). *Wave motion in elastic solids*. Courier Corporation.

[50] Guo, X., Li, H., Ahn, B. Y., Duoss, E. B., Hsia, K. J., Lewis, J. A. & Nuzzo, R. G. (2009). Two-and three-dimensional folding of thin film single-crystalline silicon for photovoltaic power applications. *Proceedings of the National Academy of Sciences*, *106*(48), 20149–20154.

[51] Guseinov, R., McMahan, C., Pérez, J., Daraio, C. & Bickel, B. (2020). Programming temporal morphing of self-actuated shells. *Nature Communications*, *11*(1), 1–7.

[52] Halkjær, S., Sigmund, O. & Jensen, J. S. (2006). Maximizing band gaps in plate structures. *Structural and Multidisciplinary Optimization*, *32*(4), 263–275. https://doi.org/10.1007/s00158-006-0037-7

[53] Hughes, T. J. (2012). *The finite element method: Linear static and dynamic finite element analysis*. Courier Corporation.

[54] Hussein, M. I., Hamza, K., Hulbert, G. M., Scott, R. A. & Saitou, K. (2006). Multiobjective evolutionary optimization of periodic layered materials for desired wave dispersion characteristics. *Structural and Multidisciplinary Optimization*, *31*(1), 60–75. https://doi.org/10.1007/s00158-005-0555-8

[55] Hutchinson, R. G. & Fleck, N. A. (2006). The structural performance of the periodic truss. *Journal of the Mechanics and Physics of Solids*, *54*(4), 756–782. https://doi.org/10.1016/j.jmps.2005.10.008

[56] Injeti, S. S., Celli, P., Bhattacharya, K. & Daraio, C. (2021). Tuning acoustic impedance in load-bearing structures. *In preparation*.

[57] Injeti, S. S., Daraio, C. & Bhattacharya, K. (2019a). Metamaterials with engineered failure load and stiffness. *Proceedings of the National Academy of Sciences*, *116*(48), 23960–23965. https://doi.org/10.1073/pnas.1911535116

[58] Injeti, S. S., Daraio, C. & Bhattacharya, K. (2019b). Metamaterials with engineered failure load and stiffness. *Proceedings of the National Academy of Sciences*, *116*(48), 23960–23965. https://doi.org/10.1073/pnas.1911535116

[59] Injeti, S. S., Daraio, C. & Bhattacharya, K. (2019c). Metamaterials with engineered failure load and stiffness. *Proceedings of the National Academy of Sciences*, *116*(48), 23960–23965.

[60] Injeti, S. S., Israr, A., Liu, T., Mengüç, Y., Piazza, D. & Shin, D. D. (2021). A tuned mass amplifier for enhanced haptic feedback. *ArXiv Preprint arXiv:2101.11594*.

[61] Jiménez-Gambın, S., Jiménez, N., Benlloch, J. M. & Camarena, F. (2019). Holograms to focus arbitrary ultrasonic fields through the skull. *Physical Review Applied*, *12*, 014016. https://doi.org/10.1103/PhysRevApplied.12.014016

[62] Jing, H., Özdemir, S., Lü, X.-Y., Zhang, J., Yang, L. & Nori, F. (2014). Pt-symmetric phonon laser. *Physical Review Letters*, *113*(5), 053604.

[63] Joulain, K., Drevillon, J., Ezzahri, Y. & Ordonez-Miranda, J. (2016). Quantum thermal transistor. *Physical Review Letters*, *116*(20), 200601.

[64] Kadic, M., Milton, G. W., Hecke, M. & Wegener, M. (2019). 3D metamaterials. *Nature Reviews Physics*, 1–13.

[65] Kepler, J. A. (2011). Simple stiffness tailoring of balsa sandwich core material. *Composites Science and Technology*.

[66] Kobayashi, W., Teraoka, Y. & Terasaki, I. (2009). An oxide thermal rectifier. *Applied Physics Letters*, *95*(17), 171905.

[67] Kotikian, A., McMahan, C., Davidson, E. C., Muhammad, J. M., Weeks, R. D., Daraio, C. & Lewis, J. A. (2019). Untethered soft robotic matter with passive control of shape morphing and propulsion. *Science Robotics*, *4*(33).

[68] Krödel, S. & Daraio, C. (2016). Microlattice metamaterials for tailoring ultrasonic transmission with elastoacoustic hybridization. *Physical Review Applied*, *6*, 064005. https://doi.org/10.1103/PhysRevApplied.6.064005

[69] Krödel, S., Delpero, T., Bergamini, A., Ermanni, P. & Kochmann, D. M. (2014). 3d auxetic microlattices with independently controllable acoustic band gaps and quasi-static elastic moduli. *Advanced Engineering Materials*, *16*(4), 357–363. https://doi.org/10.1002/adem.201300264

[70] Leong, T. G., Randall, C. L., Benson, B. R., Bassik, N., Stern, G. M. & Gracias, D. H. (2009). Tetherless thermobiochemically actuated microgrippers. *Proceedings of the National Academy of Sciences*, *106*(3), 703–708.

[71] Li, B., Wang, L. & Casati, G. (2004). Thermal diode: Rectification of heat flux. *Physical Review Letters*, *93*(18), 184301.

[72] Li, B., Wang, L. & Casati, G. (2006). Negative differential thermal resistance and thermal transistor. *Applied Physics Letters*, *88*(14), 143501.

[73] Li, F., Anzel, P., Yang, J., Kevrekidis, P. G. & Daraio, C. (2014). Granular acoustic switches and logic elements. *Nature Communications*, *5*(1), 1–6.

[74] Li, W., Meng, F., Chen, Y., Li, Y. & Huang, X. (2019). Topology optimization of photonic and phononic crystals and metamaterials: A review. *Advanced Theory and Simulations*, *2*(7), 1900017. https://doi.org/10.1002/adts.201900017

[75] Li, X.-F., Ni, X., Feng, L., Lu, M.-H., He, C. & Chen, Y.-F. (2011). Tunable unidirectional sound propagation through a sonic-crystal-based acoustic diode. *Physical Review Letters*, *106*(8), 084301.

[76] Liang, B., Guo, X., Tu, J., Zhang, D. & Cheng, J. (2010). An acoustic rectifier. *Nature Materials*, *9*(12), 989–992.

[77] Liang, B., Yuan, B. & Cheng, J.-c. (2009). Acoustic diode: Rectification of acoustic energy flux in one-dimensional systems. *Physical Review Letters*, *103*(10), 104301.

[78] Liebold-Ribeiro, Y. & Körner, C. (2014). Phononic band gaps in periodic cellular materials. *Advanced Engineering Materials*, *16*(3), 328–334. https://doi.org/10.1002/adem.201300064

[79] Liu, G.-R. & Quek, S. S. (2013). *The finite element method: A practical course*. Butterworth-Heinemann.

[80] Lu, Y., Yang, Y., Guest, J. K. & Srivastava, A. (2017). 3-d phononic crystals with ultra-wide band gaps. *Scientific Reports*, *7*, 43407. https://doi.org/10.1038/srep43407

[81] Markos, P. & Soukoulis, C. M. (2008). *Wave propagation: From electrons to photonic crystals and left-handed materials*. Princeton University Press.

[82] Matlack, K. H., Bauhofer, A., Krödel, S., Palermo, A. & Daraio, C. (2016). Composite 3d-printed metastructures for low-frequency and broadband vibration absorption. *Proceedings of the National Academy of Sciences*, *113*(30), 8386–8390.

[83] Maxwell, J. C. (1864). On the calculation of the equilibrium and stiffness of frames. *The London, Edinburgh, and Dublin Philosophical Magazine and Journal of Science*, *27*(182), 294–299.

[84] Meza, L. R., Das, S. & Greer, J. R. (2014). Strong, lightweight, and recoverable three-dimensional ceramic nanolattices. *Science*, *345*(6202), 1322–1326. https://doi.org/10.1126/science.1255908

[85] Milton, G. W. (2002). *The theory of composites*. Cambridge University Press.

[86] Milton, G. W. (2018). Stiff competition. *Nature*, *564*, E1.

[87] Milton, G. W. & Cherkaev, A. V. (1995). Which elasticity tensors are realizable? *Journal of Engineering Materials and Technology*, *117*(4), 483–493.

[88] Mishuris, G. & Slepyan, L. (2014). Brittle fracture in a periodic structure with internal potential energy. *Proceedings of the Royal Society A: Mathematical, Physical and Engineering Sciences*.

[89] Moini, M., Olek, J., Youngblood, J. P., Magee, B. & Zavattieri, P. D. (2018). Additive manufacturing and performance of architectured cement-based materials. *Advanced Materials*, *30*(43), 1802123. https://doi.org/10.1002/adma.201802123

[90] Montgomery, R. E., Weber, F. J., White, D. F. & Thompson, C. M. (1982). On the development of acoustically transparent structural plastics. *The Journal of the Acoustical Society of America*, *71*(3), 735–741.

[91] Morcos, F., Schafer, N. P., Cheng, R. R., Onuchic, J. N. & Wolynes, P. G. (2014). Coevolutionary information, protein folding landscapes, and the thermodynamics of natural selection. *Proceedings of the National Academy of Sciences*, *111*(34), 12408–12413.

[92] Naficy, S., Gately, R., Gorkin III, R., Xin, H. & Spinks, G. M. (2017). 4d printing of reversible shape morphing hydrogel structures. *Macromolecular Materials and Engineering*, *302*(1), 1600212.

[93] Nemat-Nasser, S. & Hori, M. (1999). *Micromechanics: Overall properties of heterogeneous materials*. North-Holland.

[94] Nesterenko, V., Daraio, C., Herbold, E. & Jin, S. (2005). Anomalous wave reflection at the interface of two strongly nonlinear granular media. *Physical Review Letters*, *95*(15), 158702.

[95] Nury, H., Poitevin, F., Van Renterghem, C., Changeux, J.-P., Corringer, P.-J., Delarue, M. & Baaden, M. (2010). One-microsecond molecular dynamics simulation of channel gating in a nicotinic receptor homologue. *Proceedings of the National Academy of Sciences*, *107*(14), 6275–6280.

[96] Pajunen, K., Johanns, P., Pal, R. K., Rimoli, J. J. & Daraio, C. (2019). Design and impact response of 3d-printable tensegrity-inspired structures. *Materials & Design*, *182*, 107966. https://doi.org/10.1016/j.matdes.2019.107966

[97] Palermo, A., Wang, Y., Celli, P. & Daraio, C. (2019). Tuning of surface-acoustic-wave dispersion via magnetically modulated contact resonances. *Physical Review Applied*, *11*, 044057. https://doi.org/10.1103/PhysRevApplied.11.044057

[98] Park, J. H., Ma, P. S. & Kim, Y. Y. (2015). Design of phononic crystals for self-collimation of elastic waves using topology optimization method. *Structural and Multidisciplinary Optimization*, *51*(6), 1199–1209. https://doi.org/10.1007/s00158-014-1206-8

[99] Pham, M.-S., Liu, C., Todd, I. & Lertthanasarn, J. (2019). Damage-tolerant architected materials inspired by crystal microstructure. *Nature*, *565*, 305. https://doi.org/10.1038/s41586-018-0850-3

[100] Phani, A. S. (2017). Elastodynamics of lattice materials. *Dynamics of lattice materials* (pp. 53–92). John Wiley & Sons, Ltd. https://doi.org/10.1002/9781118729588.ch3

[101] Phani, A. S., Woodhouse, J. & Fleck, N. A. (2006). Wave propagation in two-dimensional periodic lattices. *The Journal of the Acoustical Society of America*, *119*(4), 1995–2005. https://doi.org/10.1121/1.2179748

[102] Popa, B.-I. & Cummer, S. A. (2014). Non-reciprocal and highly nonlinear active acoustic metamaterials. *Nature Communications*, *5*(1), 1–5.

[103] Raney, J. R., Compton, B. G., Mueller, J., Ober, T. J., Shea, K. & Lewis, J. A. (2018). Rotational 3d printing of damage-tolerant composites with programmable mechanics. *Proceedings of the National Academy of Sciences*, *115*(6), 1198–1203. https://doi.org/10.1073/pnas.1715157115

[104] Rayneau-Kirkhope, D., Mao, Y. & Farr, R. (2012). Ultralight fractal structures from hollow tubes. *Physical Review Letters*.

[105] Reid, D. R., Pashine, N., Wozniak, J. M., Jaeger, H. M., Liu, A. J., Nagel, S. R. & de Pablo, J. J. (2018). Auxetic metamaterials from disordered networks. *Proceedings of the National Academy of Sciences*, *115*(7), E1384–E1390.

[106] Ronellenfitsch, H., Stoop, N., Yu, J., Forrow, A. & Dunkel, J. (2019). Inverse design of discrete mechanical metamaterials. *Physical Review Materials*, *3*, 095201. https://doi.org/10.1103/PhysRevMaterials.3.095201

[107] Salzer, R. (2012). *Biomedical imaging: Principles and applications*. John Wiley & Sons.

[108] Schaedler, T. A., Jacobsen, A. J., Torrents, A., Sorensen, A. E., Lian, J., Greer, J. R., Valdevit, L. & Carter, W. B. (2011). Ultralight metallic microlattices. *Science*.

[109] Shan, S., Kang, S. H., Raney, J. R., Wang, P., Fang, L., Candido, F., Lewis, J. A. & Bertoldi, K. (2015). Multistable architected materials for trapping elastic strain energy. *Advanced Materials*, *27*(29), 4296–4301.

[110] Shores, T. S. (2007). *Applied linear algebra and matrix analysis* (Vol. 2541). Springer.

[111] Sigalas, M., Kushwaha, M. S., Economou, E. N., Kafesaki, M., Psarobas, I. E. & Steurer, W. (2005). Classical vibrational modes in phononic lattices: Theory and experiment. *Zeitschrift für Kristallographie-Crystalline Materials*, *220*(9-10), 765–809.

[112] Sigmund, O. & Jensen, J. S. (2003). Systematic design of phononic band-gap materials and structures by topology optimization. *Philosophical Transactions of the Royal Society A*, *361*, 1001–1019. https://doi.org/10.1098/rsta.2003.1177

[113] Spadoni, A., Höhler, R., Cohen-Addad, S. & Dorodnitsyn, V. (2014). Closed-cell crystalline foams: Self-assembling, resonant metamaterials. *The Journal of the Acoustical Society of America*, *135*(4), 1692–1699. https://doi.org/10.1121/1.4867375

[114] Su, X., Norris, A. N., Cushing, C. W., Haberman, M. R. & Wilson, P. S. (2017). Broadband focusing of underwater sound using a transparent pentamode lens. *The Journal of the Acoustical Society of America*, *141*(6), 4408–4417. https://doi.org/10.1121/1.4985195

[115] Tallarico, D., Movchan, N. V., Movchan, A. B. & Colquitt, D. J. (2017). Tilted resonators in a triangular elastic lattice: Chirality, bloch waves and negative refraction. *Journal of the Mechanics and Physics of Solids*, *103*, 236–256. https://doi.org/10.1016/j.jmps.2017.03.007

[116] Tantikom, K. & Aizawa, T. (2005). Compressive deformation simulation of regularly cell-structured materials with various column connectivity. *Materials Transactions*.

[117] Thompson, C. M. (1990). Development of a structurally rigid, acoustically transparent plastic. *The Journal of the Acoustical Society of America*, *87*(3), 1138–1143.

[118] Torrents, A., Schaedler, T. A., Jacobsen, A. J., Carter, W. B. & Valdevit, L. (2012). Characterization of nickel-based microlattice materials with structural hierarchy from the nanometer to the millimeter scale. *Acta Materialia*.

[119] Vahala, K., Herrmann, M., Knünz, S., Batteiger, V., Saathoff, G., Hänsch, T. & Udem, T. (2009). A phonon laser. *Nature Physics*, *5*(9), 682–686.

[120] Vidyasagar, A., Krödel, S. & Kochmann, D. M. (2018). Microstructural patterns with tunable mechanical anisotropy obtained by simulating anisotropic spinodal decomposition. *Proceedings of the Royal Society A*, *474*(2218), 20180535. https://doi.org/10.1098/rspa.2018.0535

[121] Vila, J., Pal, R. K. & Ruzzene, M. (2017). Observation of topological valley modes in an elastic hexagonal lattice. *Physical Review B*, *96*, 134307. https://doi.org/10.1103/PhysRevB.96.134307

[122] Vinson, J. R. (1999). *The behavior of sandwich structures of isotropic and composite materials*. CRC Press.

[123] Wang, L. & Li, B. (2007). Thermal logic gates: Computation with phonons. *Physical Review Letters*, *99*(17), 177208.

[124] Wang, L. & Li, B. (2008). Phononics gets hot. *Physics World*, *21*(03), 27.

[125] Wang, P., Casadei, F., Kang, S. H. & Bertoldi, K. (2015). Locally resonant band gaps in periodic beam lattices by tuning connectivity. *Physical Review B*, *91*, 020103. https://doi.org/10.1103/PhysRevB.91.020103

[126] Xia, X., Afshar, A., Yang, H., Portela, C. M., Kochmann, D. M., Di Leo, C. V. & Greer, J. R. (2019). Electrochemically reconfigurable architected materials. *Nature*, *573*(7773), 205–213.

[127] Zhang, J. & Ashby, M. F. (1992). The out-of-plane properties of honeycombs. *International Journal of Mechanical Sciences*.

[128] Zhang, T., Cheng, Y., Guo, J.-z., Xu, J.-y. & Liu, X.-j. (2015). Acoustic logic gates and boolean operation based on self-collimating acoustic beams. *Applied Physics Letters*, *106*(11), 113503.

[129] Zhang, Z., Ni, X., Wu, H., Sun, M., Bao, G., Wu, H. & Jiang, S. (2021). Pneumatically actuated soft gripper with bistable structures. *Soft Robotics*.

[130] Zheng, Z., Wang, H., Dong, L., Shi, Q., Li, J., Sun, T., Huang, Q. & Fukuda, T. (2021). Ionic shape-morphing microrobotic end-effectors for environmentally adaptive targeting, releasing, and sampling. *Nature Communications*, *12*(1), 1–12.